

Stochastic Modeling of the Formation of Aromatics in Combustion

by

Qi Wang

A dissertation submitted in partial fulfillment
of the requirements for the degree of
Doctor of Philosophy
(Mechanical Engineering)
in the University of Michigan
2021

Doctoral Committee:

Associate Research Scientist Paolo Elvati, Co-Chair
Professor Angela Violi, Co-Chair
Professor André L. Boehman
Professor James F. Driscoll

Qi Wang

bluelion@umich.edu

ORCID iD: 0000-0002-9636-9659

©Qi Wang 2021

Dedicated to my family,
my mom Liu, Guiying and
my dad Wang, Yujie.

ACKNOWLEDGMENTS

This dissertation and years of my research work at University of Michigan would not be possible without the support and guidance of my advisor, Professor Angela Violi, who inspired my interests in the combustion field and helped me go through the toughest time of my Ph.D. study. Nor would it be possible without Dr. Paolo Elvati, who guided me and provided valuable discussions and insights for enormous times.

Thank you as well to the rest of my dissertation committee member, Professor André L. Boehman and Professor James F. Driscoll, for the time and expertise that leads to the completion of this dissertation.

To my fellows in the Violi Group, I truly treasure our collaborations and conversations. It has been a pleasure working with all of you. I would like to give special thanks to my friend and close collaborator Xuetao Shi. I have learned a lot from you, and we sure turned quite some ideas into meaningful results.

I would also like to thank the rest of my friends. Thank you Anqi Sun, Fengwen Song, Calvin Wang, and Zifeng Peng, for helping me a lot throughout the years with my study at University of Michigan and life here in Michigan. Thank you Mingxin Ding, Dr. Yilong Li, Anqi, and Nuan, for your companionship at different stages of my Ph.D. life. You all made my life colorful.

Finally, I would like to thank my mom and dad for your love and support all along. This dissertation is for you.

TABLE OF CONTENTS

DEDICATION	ii
ACKNOWLEDGEMENTS	iii
LIST OF FIGURES	vi
LIST OF TABLES	viii
LIST OF ABBREVIATIONS	ix
ABSTRACT	xi
CHAPTER	
1 Introduction	1
1.1 Knowledge of Combustion-generated PACs	2
1.1.1 Early Studies from Shock-tubes and Premixed Flames	2
1.1.2 The Formation of Six-membered Aromatic PAHs	4
1.1.3 Recent Experimental Evidences on the Complexity of the PACs	5
1.2 Deterministic Modeling of the PACs in Combustion	6
1.3 Stochastic Modeling of PACs in Combustion	8
1.4 Overview of the Stochastic Models in Combustion	9
1.5 Scope, Objectives, and Achievements	11
2 Methodology	14
2.1 Overview of the SNapS2 Code	14
2.2 Implementation of the Kinetic Mechanism	16
2.2.1 Full Reversibility and Thermodynamic Consistency	16
2.2.2 Sterically-resolved Reaction Descriptions	18
3 A Kinetic Mechanism for the Formation of PACs in Combustion	22
3.1 Carbon-Hydrogen Reactions	22
3.2 Oxygen-Hydrogen Reactions	26
3.3 Carbon-Carbon Reactions	27
3.4 Carbon-Oxygen Reactions	34
3.5 Isomerizations	38
4 Exploring Missing Reaction Pathways	41
4.1 The Formation of Benzofuran and Dibenzofuran	41

4.1.1	Formation of Benzofuran from Benzene	42
4.1.2	Formation of Dibenzofuran from Biphenyl	45
4.1.3	Alternative and Competing Pathways Study	46
4.2	The Formation of Five-membered Rings	51
4.2.1	Five-membered Ring Formation on Zig-Zag Site from Naphthalene	52
4.2.2	Five-membered Ring Formation on Armchair Site from Biphenyl	54
4.2.3	Reaction Pathways in a Closed Homogeneous Batch Reactor . . .	55
5	Validations of the SNapS2 in Various Combustion Conditions	58
5.1	Mass Spectrum in an Ethylene Counterflow Diffusion Flame	58
5.1.1	The Flame System	59
5.1.2	Stochastic Modeling	59
5.2	Oxygen content in a Coflow Diffusion Jet A-1 Surrogate Flame	62
5.2.1	The Flame System	63
5.2.2	Stochastic Modeling	63
5.3	Molecular Structures in an Ethylene Premixed Flame	68
5.3.1	The Flame System and the Gas-phase Modeling	68
5.3.2	Stochastic Modeling	69
6	Applications of the SNapS2 Beyond the Limitation of Diagnostics	80
6.1	Spatial Dependence of the PAC Growth in an Ethylene Counterflow Dif- fusion Flame	81
6.1.1	The Flame System	81
6.1.2	Reactivity Along the Centerline and Streamlines	81
6.1.3	Spatial Dependence of the PAC Formation	83
6.2	Effect of Ethanol on the Formation of Aromatics	87
6.2.1	The Flame System	88
6.2.2	Gas-phase Kinetic Mechanism	89
6.2.3	Gas-phase Simulations	90
6.2.4	Stochastic Simulations	94
7	Conclusions and Future Work	101
	BIBLIOGRAPHY	105

LIST OF FIGURES

2.1	Examples of scenarios for the site selections in the S _{Nap} S ₂ kinetic mechanism.	19
2.2	Comparison of the reaction selection process between S _{Nap} S code and S _{Nap} S ₂ code.	20
2.3	Example of better site definition in the S _{Nap} S ₂ kinetic mechanism.	21
4.1	Reaction pathways for the formation of benzofuran from benzene.	43
4.2	Resonance structures for A3 , demonstrating its delocalized radical site.	44
4.3	Reaction pathways for the formation of dibenzofuran from biphenyl.	45
4.4	Reaction comparisons for hydrogen abstraction and acetylene addition with the presence of different functional groups.	50
4.5	Reaction pathways for the formation of five-membered ring from a zig-zag site and a C ₂ gas phase species.	53
4.6	Reaction pathways for the formation of five-membered ring from an armchair site and a C ₁ gas phase species.	54
4.7	The rate of production for the formation of acenaphthylene (N14).	56
4.8	The rate of production for the formation of acenaphthene (N15).	57
5.1	Snapshot of the central plane of the counterflow flame obtained via CFD simulations.	60
5.2	Comparison between the experimental aerosol mass spectrum and the mass spectrum predicted by S _{Nap} S ₂ .	61
5.3	Temperature profile from CFD simulations for the coflow diffusion flame.	64
5.4	Oxygen-to-carbon ratio plotted against the molecular mass for different locations along the center streamline.	65
5.5	Example molecules simulated by the S _{Nap} S ₂ at an HAB of 8 mm of the premixed flame.	70
5.6	Possible number of chemical groups involving oxygen observed in simulated S _{Nap} S ₂ -generated molecules at 8 mm of the premixed flame.	71
5.7	Oxygen-to-carbon ratio for S _{Nap} S ₂ -generated molecules with respect to the number of oxygen atoms in the premixed flame.	72
5.8	Hydrogen-to-carbon ratio with respect to the number of carbon atoms for S _{Nap} S ₂ -generated molecules in the premixed flame.	73
5.9	Hydrogen-to-carbon ratio with respect to the number of carbon atoms for S _{Nap} S ₂ -generated pure hydrocarbons in the premixed flame.	74
5.10	The percentage of acyclic carbon with respect to the number of carbon atoms for the S _{Nap} S ₂ -generated molecules at an HAB of 8 mm of the premixed flame.	75

5.11	The number of five- and six-membered rings with respect to the number of carbon atoms for the SNapS2-generated molecules at an HAB of 8 mm of the premixed flame	75
5.12	The number of non-embedded five-membered rings with respect to the number of six-membered rings for SNapS2-generated molecules and assigned PACs from AFM images	76
5.13	Frequency of the three types of five-membered rings formed in the SNapS2-generated molecules at 8 mm.	77
5.14	The relative plane displacement with respect to the number of carbon atoms . .	78
6.1	Time evolution of selected species in the ethylene counterflow diffusion flame .	82
6.2	SNapS2-generated mass spectra at different locations along the streamline i . .	84
6.3	Comparison between experimentally and computed properties of the pure and 50% doped systems	90
6.4	Mole fraction profiles of selected species from gas-phase modeling results for the set of six flames	92
6.5	Mole fractions of small aromatics and large PAHs from gas-phase simulations for the set of six flames	93
6.6	Average and cumulative chemical growth of PACs as a function of height above the burner from SNapS2 simulations for the set of six flames	95
6.7	Percentage of oxy-PACs and the mole fraction profiles for atomic hydrogen and atomic oxygen from gas-phase simulations as a function of HAB from SNapS2 simulations for the set of six flames	97
6.8	Example of compounds predicted in the pure ethylene/air premixed flame with equivalence ratio of 2.34 using benzene as seed molecule	98

LIST OF TABLES

3.1	Reaction schemes for carbon-hydrogen reaction category part I: reactions for cyclic carbon sites	23
3.2	Reaction schemes for carbon-hydrogen reaction category part II: reactions for open-chain carbon sites	24
3.3	Reaction schemes for oxygen-hydrogen reaction category	27
3.4	Reaction schemes for carbon-carbon reaction category part I: reactions for carbon fragments addition/abstraction to/from aromatic or aliphatic carbon	28
3.5	Reaction schemes for carbon-carbon reaction category part II: reactions for five-membered hydrocarbon ring formation/breaking	29
3.6	Reaction schemes for carbon-carbon reaction category part III: reactions for six-membered ring formation/breaking through HACA pathways	30
3.7	Reaction schemes for carbon-carbon reaction category part IV: reactions for six-membered ring formation/breaking through pathways other than HACA . .	31
3.8	Reaction schemes for carbon-carbon reaction category part V: reactions for ring conversion from five-membered to six-membered hydrocarbon ring	32
3.9	Reaction schemes for carbon-oxygen reaction category part I: reactions for oxygen addition/abstraction to/from carbon and carbon fragments addition/abstraction to/from oxygen	35
3.10	Reaction schemes for carbon-oxygen reaction category part II: reactions for five-membered furan ring formation/breaking	36
3.11	Reaction schemes for carbon-oxygen reaction category part III: reactions for ring oxidation	37
3.12	Reaction schemes for isomerization reaction category	39
6.1	The time percentages of 5 reactions at three locations of the flame in terms of (DFC, DFFO), weighed by the lifespan of the reacting PACs from SNapS2-simulated traces	86
6.2	Most frequent/relevant/important reactions occurring in SNapS2 simulation in the pure ethylene/ air premixed flame with equivalence ratio of 2.34, at different HAB.	99

LIST OF ABBREVIATIONS

PACs Polycyclic Aromatic Compounds

PAHs Polycyclic Aromatic Hydrocarbons

oxy-PACs Oxygenated Polycyclic Aromatic Compounds

HACA Hydrogen-Abstraction-Acetylene(C_2H_2)-Addition

CAHM Carbon(C_2H_2)-Addition-Hydrogen-Migration

kMC kinetic Monte Carlo

ODEs Ordinary Differential Equations

RREs Reaction Rate Equations

CME Chemical Master Equation

MM Molecular Mechanism

CFD Computational Fluid Dynamics

AMPI Atomistic Model for Particle Inception

SNapS Stochastic Nanoparticle Simulator

SMILES Simplified Molecular Input Line Entry System

SMARTS SMiles ARbitrary Target Specification

AFM Atomic Force Microscopy

XPS X-ray Photoelectron Spectroscopy

VUV-MBMS Molecular-Beam Mass Spectrometry with Vacuum-Ultraviolet Photoionization

VUV-AMS Aerosol Mass Spectrometry with Vacuum-Ultraviolet Photoionization

RC Ring Closure

HE Hydrogen Elimination

DHE Direct Hydrogen Elimination

HD Hydrogen Disproportionation

DFFO Distance From the Fuel Outlet

DFC Distance From the Centerline

HAB Height Above the Burner

O/C Oxygen-to-Carbon Ratio

H/C Hydrogen-to-Carbon Ratio

ABSTRACT

Understanding the formation of polycyclic aromatic compounds (PACs) in combustion not only bridges the knowledge gap between the small gas-phase species and incipient soot particles, but may also help address the global emission issues of both PACs and soot. In this thesis, I present a kinetic mechanism utilizing reactive sites (*i.e.*, the chemical and physical neighbourhoods) to describe the PAC growth in combustion. This kinetic mechanism was implemented for a stochastic modeling code (*i.e.*, SNapS2) recently developed by the Violi Group. To address new experimental and computational discoveries, chemical reactions were gathered and categorized from various literature, while the reaction rate constants came from either literature or my own calculations to ensure full reversibility and thermodynamic consistency. These reactions were then implemented into SNapS2 kinetic mechanism with precise reactive site definitions to eliminate the possibility of steric hindrance and unrealistic reactions. Compared with the previous version of SNapS2, thanks to this new kinetic mechanism, the computational performance increased by an order of magnitude, enabling the simulation of complex two-dimensional flames. Some missing reaction pathways, which were identified from experimental evidence and simulations but not available in the literature, were explored and calculated using quantum chemistry methods. These newly discovered reactions were included in the SNapS2 kinetic mechanism as well, and some of them were already proven to be important under specific conditions.

The characteristics of the PACs predicted with the kinetic mechanism were compared against different experimental measurements: mass spectra measured in a counterflow diffusion flame, the oxygen-to-carbon ratios obtained at different locations of a coflow diffusion flame, and the molecular structures observed in a premixed laminar flame. These

successful validations demonstrate that the S NapS2 kinetic mechanism provides a high-fidelity, and yet generic, description of the PAC formation under various combustion conditions, making S NapS2 the first-of-its-kind to have such extensive flexibility and wealth of information. It greatly contributes to reveal the underlying chemical pathways to the experimental observations.

Furthermore, S NapS2 code and the kinetic mechanism have shown its capability to provide valuable insights on the formation of aromatics beyond the limitation of diagnostics. For one application, spatial dependence of the PAC growth in an ethylene counterflow diffusion flame was characterized by S NapS2 simulations, revealing distinct PAC growth pathways for the streamlines starting from fuel side and oxidizer side. Given the fidelity of the S NapS2 predictions, it was also used to examine conditions that are impossible to test experimentally, like completely decoupling the effects of flame temperature when studying the effects of ethanol doping on the formation of aromatics, highlighting the chemical pathways that result in soot reduction. Both applications show the uniqueness and great potential of the model to obtain insights of the PAC formation when measurements are hard to obtain or experiments are difficult to control. Altogether, this dissertation lays a solid foundation that not only helps explain the experimental observations for the formation of soot precursors, but also provides a powerful tool for exploring the gas-phase nanoparticle growth that could drive the development of novel combustion technologies or the design of new nanomaterials.

CHAPTER 1

Introduction

The formation of Polycyclic Aromatic Compounds (PACs) and particles has become one of the central themes of combustion research due to environmental concerns about pollutant emissions [205, 138]. The global atmosphere emissions of the 16 PACs listed as the United States Environmental Protection Agency priority pollutant was estimated to be 520 Gg per year in 2004 with biofuel (56.7%), wildfire (17.0%) and consumer product usage (6.9%) as the major sources [205]. Their toxic effects on both human and ecosystem health are well documented [1]. Exposure to PACs may cause toxic effects including carcinogenicity, teratogenicity, genotoxicity, and immunotoxicity [138].

The formation and growth of the PACs also bridge the main combustion zone chemistry with the formation of particles (*i.e.*, nanoparticles and soot). The formation of PACs has long been considered as an important step for soot formation, since PACs are the key building blocks for the nucleation step that leads to the transition from gas-phase species to nanoparticles. Thus, the characteristics of the PACs formed under various combustion conditions would directly influence the soot formation. For example, Elvati *et al.* [45, 43, 46, 44] indicated that the dimerization of PACs in general is affected by the shape of the molecules as well as the oxygen content, and that oxygenated species have less tendency to form dimers than pure hydrocarbons. Thus, understanding the formation of PACs in combustion not only bridges the knowledge gap between the small gas-phase species and incipient soot particles, but may also help address the global emission issues of

both PACs and soot. Their applications in material synthesis [69] and compression ignition engines [167, 102] make PACs interesting and important to study as well.

1.1 Knowledge of Combustion-generated PACs

Knowledge of the combustion-generated PACs has been accumulated from both experiments and simulations over the past few decades. Since these PACs are formed in very complex gas-phase systems, early studies made a lot of assumptions to simplify, both experimentally and computationally. Early experimental studies used shock-tubes to learn combustion chemistry and premixed flames to understand the physical and chemical factors that alter the formation of PAHs. At the same time, the computational works largely focused on the formation pathways of six-membered aromatic PAHs. However, recent experimental evidence revealed the complex molecular structures of the combustion-generated PACs. These new experimental discoveries showed a general lack of understanding and predicting capabilities for most of the models to capture this complexity. While SNaPS [96] was promising for modeling the growth of these PACs, its code and kinetic mechanism need to be completely reexamined and further improved.

1.1.1 Early Studies from Shock-tubes and Premixed Flames

The evolution of gas-phase species during combustion is well known to depend on the specific physical and chemical conditions of the system. Previous works in shock-tubes and premixed flames have provided great insights on the formation of Polycyclic Aromatic Hydrocarbons (PAHs). Shock-tube studies have been significantly contributing to the understanding of the chemical process of PAH formation. Frenklach and his coworkers proposed the Hydrogen-Abstraction-Acetylene(C_2H_2)-Addition (HACA) pathway in an acetylene shock-tube pyrolysis study [54] in 1985. HACA pathways were later expanded and proven to be the major route of PAH growth in most pure hydrocarbon flames [58, 53, 56, 57]. Gar-

diner [61] reviewed the early shock-tube studies of combustion chemistry, while Hanson and Davidson [74] presented a detailed review of recent advances in shock-tube methods. Both articles highlighted the importance of shock-tube studies for combustion chemistry model validation and refinement.

Several studies have been conducted over the years on the effects of temperature, pressure, fuel composition, oxygenates additions on both soot volume and PAH formation of laminar premixed flames. Wagner *et al.* (see [48] and references therein) revealed a bell shaped dependence of the final soot volume on the maximum flame temperature in experiments, as well as the dependence of the final soot volume on pressure. Frenklach [52] further applied the kinetic Monte Carlo (kMC) technique to model surface growth of soot particles, finding that the growth rate of soot particle surface increases with temperature while the growth rate of PAHs decays with temperature. Mauss and Bockhorn [48] later confirmed this phenomena with numerical modeling. Maricq [108] examined soot composition as a function of four types of fuels, height in flame, equivalence ratio, and fuel/air flow rate in experiments. Wu *et al.* [195] summarized the early work on the effects of ethanol doping on PAHs or soot formation in flames and shock-tubes, and reported a similar reduction of PAHs and soot in premixed ethylene/air flames by addition of ethanol with experiments. Elvati *et al.* [43] further studied the physical and chemical growth mechanisms of the premixed laminar flames from literature by Wu *et al.* [195] and Salamanca *et al.* [142], employing a variety of computational techniques and revealing some reasons of soot reduction with addition of oxygenates. All these studies above involve comparisons across several flames with similar conditions (*e.g.*, equivalence ratio, carbon flow rate, and maximum flame temperature) in order to isolate and observe the effect of changing a single physical or chemical condition. These studies greatly contribute to the understanding of the factors that could change the formation of PAHs and soot.

1.1.2 The Formation of Six-membered Aromatic PAHs

The more fundamental understanding of the underlying reaction pathways for the PAH formation have also been investigated for a long time. Great interests have been focused on the formation of the six-membered aromatic PAHs, the honeycomb-like structures. Among those, one of the most famous pathways is the HACA, which contains a repetitive sequence of two reaction steps – a hydrogen abstraction reaction (*i.e.*, activation step) and an acetylene (C_2H_2) addition reaction to the radical site. An extra aromatic ring can then be formed through a ring closure reaction. The HACA includes three major pathways, the Frenklach's route [58], the alternative Frenklach's route [54, 9], and the Bittner-Howard's route [13]. Beside the well-known HACA pathways, other pathways have been proposed over the years, such as Diels-Alder growth [155, 90], cyclodehydrogenation (*i.e.*, bay-closure) [14, 176, 131], Carbon(C_2H_2)-Addition-Hydrogen-Migration (CAHM) pathway [204, 203], growth initiated by C_3 species (such as propargyl radical, allene, propyne and propene) [130, 117] and C_4 species (such as vinylacetylene) [115, 104].

Diels-Alder-type pathway was proposed by Siegmann and Sattler [155] in 2000 as the dominant route of PAH growth in methane combustion. Kislov *et al.* [90] later studied this pathway extensively using *ab initio* Gaussian-3-type calculations and concluded that the Diels-Alder pathway cannot compete with the HACA pathways even at high combustion temperatures by examining the reaction rate constants. Bay-closure pathways were defined by Böhm and Jander [14] in 1999. After that, quantum chemistry calculations were performed and reaction rate constants were determined by Violi [176] on the five-membered ring bay-closure pathways and by Raj *et al.* [131] on the six-membered ring bay-closure pathways. CAHM pathway was proposed by Zhang *et al.* [204, 203] to be important in the low-temperature, post-flame region. Frenklach *et al.* [57] later implied that both HACA and CAHM pathways can explain the formation of aliphatic groups chemisorbed at edges of aromatics. The six-membered aromatic growth initiated by propargyl radical (C_3H_3) addition was studied by Raj *et al.* [130], with the pathways being developed up to the for-

mation of pyrene. C_3H_3 is known to be a precursor of benzene (C_6H_6) in combustion and has appreciable concentration in flames. The growth initiated by allene ($\mathcal{A}C_3H_4$) addition and propyne ($\mathcal{P}C_3H_4$) addition was examined by Mebel *et al.* [117]. It was concluded that, although phenyl radical (C_6H_5) + $\mathcal{A}C_3H_4$ and C_6H_5 + $\mathcal{P}C_3H_4$ reactions can produce indene + H as the main product at low temperatures and pressures, under conditions relevant to combustion, these reactions mostly form phenyl-substituted propyne or allene. The six-membered aromatic growth initiated by vinylacetylene (C_4H_4) addition has been systematically investigated by Liu *et al.* [104] recently.

1.1.3 Recent Experimental Evidences on the Complexity of the PACs

As complex as it already seems for the formation pathways of six-membered aromatic PAHs, recent direct and indirect experimental evidences suggest that the actual combustion-generated PACs are much more complex than the purely benzenoid aromatic compounds, as it actually contains aliphatic chains [20, 28, 147], different types of five-membered rings [147], oxygen contents [19, 82, 26], and curvatures [160, 15, 111].

For nascent soot surface, Cain *et al.* [20] observed large amounts of aliphatic C–H groups ranging from 1 to 30 times that of aromatic C–H in a premixed, burner-stabilized flame, and the amount of aliphatic C–H relative to aromatic C–H remained approximately constant with respect to particle sizes ($D_{p,m} > 10$ nm). For gas-phase PACs, high-resolution Atomic Force Microscopy (AFM) was used for direct imaging of the build blocks forming the particles in the early stages of soot formation [28, 147], observing the noticeable presence of aliphatic side-chains. The same AFM study also showed a significant presence of penta-rings as opposed to the purely benzenoid aromatic compounds. Different types of peripheral pentagonal rings were observed, namely acenaphthylene-type, acenaphthene-type, fluorene-type, and indane-type. Numerous experimental evidences also suggest the presence of Oxygenated Polycyclic Aromatic Compounds (oxy-PACs) in even pure hydrocarbon flames. Cain *et al.* [19] studied a coflow diffusion flame of a three-

component Jet-A1 surrogate and characterized the oxygenated compounds in the range of 200 u to 600 u in mass, showing that the oxygenates are abundant in all soot samples at different locations of the flame. Commodo *et al.* [26] studied a flat laminar premixed ethylene/air flame, observing that just nucleated particles, with sizes of the order of 2 nm to 3 nm, contain about 3% of atomic oxygen over the total carbon atoms, and the O1s X-ray Photoelectron Spectroscopy (XPS) spectra suggests the presence of C–O–C ether-like bond. Johansson *et al.* [82] studied a premixed ethylene-oxygen flame and recorded XPS spectra of soot samples, from which the fractions of C–OH, C–O–C, and C=O species at different locations of the flame were determined. In addition, the AFM studies mentioned above identified three oxygenated species from the particles, a phenol, a ketone and a derivative of benzopyran (labeled in the original work as **PS7**, **PS2**, and **IS9** respectively in [28]). Each molecule requires a different formation pathway, which indicates the complexity of the oxygen reactions that occur in the flame. The curved PAHs, formed by embedding the five-membered rings into the structures, have drawn some attentions in the combustion community recently. From Martin *et al.* [111], high resolution transmission electron microscopy studies have shown that a significant fraction of curved PAHs is present in soot [160, 15]. Significant curvature has been found in 28–49% of the fringes.

These new experimental discoveries showed a general lack of understanding and predicting capabilities for the current models to capture this complexity, and called for the need of a new model for the growth of these PACs.

1.2 Deterministic Modeling of the PACs in Combustion

Due to the timescales and underlying assumptions, there are two classes of approaches usually used to model the PAC formation, the deterministic modeling and the stochastic modeling. The deterministic modeling approach, such as the one implemented in the CHEMKIN software [135], is often used as a tool for studying the chemistry of small

gas-phase species in combustion systems, and works reasonably well for predicting the concentrations of gas-phase species with molecular mass less than benzene in a range of flames [9, 139, 181, 133, 185]. The deterministic modeling approach solves a system of coupled Ordinary Differential Equations (ODEs) [87], *i.e.*, the Reaction Rate Equations (RREs) [67], derived from the Rate Laws [36] and provides the time evolution of all the species, by assuming that all the species concentrations are continuous and deterministic. As a result, a list of species, reactions, and rate constants is provided as part of the kinetic mechanism. The current gas-phase combustion kinetic mechanisms usually include species up to pyrene (*i.e.*, $C_{16}H_{10}$, 202 u) [9, 139, 181], some to coronene (*i.e.*, $C_{24}H_{12}$, 300 u) [185].

Current deterministic modeling approach is less feasible for studying the large PAC growth in combustion for the following reasons. First, there is a lack of reaction pathways and accurate rate constants, limited by the availability and accuracy of the quantum chemistry calculations [158]. Because of this, the accuracy of predicting the concentrations significantly decreases for larger species starting with naphthalene [133, 185, 151]. Second, because of the large reaction networks for PACs, the possibility of having a huge kinetic mechanism raises as well. For example, the number of unique species and reactions happening in a premixed laminar flame are at least in terms of millions [183]. The computational cost increases dramatically as increasing the number of species in the kinetic mechanism. Formulating and simulating such a system via deterministic approach are possible, but less feasible. Last but not the least, the continuous and deterministic assumptions that allow for solving the RREs do not generally hold for the PACs. The majority of the PACs have such low concentrations that would break the continuous assumption. These limitations make deterministic modeling approach inadequate for modeling PAC formation in great details and accuracy.

1.3 Stochastic Modeling of PACs in Combustion

Stochastic modeling offers a more general approach by directly solving the Chemical Master Equation (CME) [114]. The CME is a set of first-order differential equations describing the probability as a function of time to evolve according to a specific chemical reaction. The difficulty of solving the CME for even very simple systems eventually prompted the approach of constructing simulated temporal trajectories (*i.e.*, traces) [67], as averaging over sufficient traces can be used to estimate the time evolution of the reacting system. In 1976, Gillespie *et al.* [65, 66] proposed the stochastic simulation algorithm for simulating the chemical reactions. Gillespie and coworkers [67] later showed that through tau-leaping, the discrete-stochastic CME formalism is connected with the continuous-deterministic ODE formalism. As the thermodynamic limit is approached, where the molecular populations are imagined to go to infinity along with the system volume while the concentrations remain constant, the CME reduces to the RRE. This means that the ODE formalism is an approximation of the stochastic formalism which is generally accurate only if the system is sufficiently large and the tau-leaping conditions are satisfied [67].

These findings promoted the usage of stochastic modeling on the formation of PACs in combustion. The low concentrations of large PACs in combustion systems break the underlying assumptions of the continuous-deterministic formalism, and require the more general discrete-stochastic formalism. In addition, the stochastic modeling not only gives macroscopic insights (*e.g.*, PAC characteristics) like the deterministic modeling, but may also offer the detailed time evolution of individual molecules by constructing traces. This extra level of detail from the traces is very valuable, for example, for revealing the particle nucleation mechanisms. Furthermore, the stochastic modeling approach can be coupled with elementary reactions [175, 178, 24, 96] to expand the set of reactions based on reactive sites but not specific species. Therefore, the stochastic modeling is more attractive for studying the growth of PACs in combustion.

1.4 Overview of the Stochastic Models in Combustion

Over the years, several stochastic models have been proposed to study the PAC formation in combustion. Frenklach and coworkers pioneered the usage of kMC method in combustion systems to study the relative importance of different reaction pathways. In 1996, Frenklach *et al.* [52] applied a sterically resolved kMC technique to model the surface growth of soot particles under conditions typical of flame environments, in which the outcome of a specific elementary chemical reaction depends on the collision frequency, nominal reaction probability, and reactive sites. The reaction mechanism contained 13 gas-surface reactions focusing on the formation of aromatic rings. In 2005, Frenklach, Schuetz, and Ping [56] proposed a reaction pathway for the five-membered ring migration along a graphene edge, known as FSP mechanism. Employing the new migration kinetics along with kMC, simulations were carried out at conditions typical of soot growth in pure hydrocarbon flames. The reaction model developed to test the surface migration contained 9 overall reactions. The results further highlighted the role of five-membered ring migration in the growth of graphene layers.

In 2004, Violi [175, 178] introduced the Atomistic Model for Particle Inception (AMPI), which was the first to use the elementary chemical reactions and the tracking of a single species in stochastic simulations. Site descriptions included both five- and six-membered rings and generic aliphatic chains. The AMPI was able to reproduce the hydrogen-to-carbon trends identified in aromatic and aliphatic flames. The AMPI was later updated by Chung and Violi [24] to study the effect of oxidation on nanoparticle structures formed in a propane counterflow diffusion flame. In the case of high temperature and abundant radicals, the AMPI successfully predicted the nanoparticle formation. Starting from AMPI, later stochastic models until today, mostly track a single molecule under specific gas-phase environments [193, 55, 131, 132, 96].

In 2008, Celnik *et al.* [23] proposed a soot particle model that describes soot particles by their aromatic structure, including functional site descriptions and a detailed surface

chemistry mechanism. The PAH growth model in this paper included 12 jump processes, and is later named as kMC-ARomatic Site (KMC-ARS) model for PAHs surface growth. The KMC-ARS model was expanded in the following years by Raj *et al.* [131, 132]. The KMC-ARS model tracks each of the PAHs in the particles which evolve according to a list of jump processes that make use of the steady-state assumption. In 2010, the model included 20 jump processes [132]. The PAHs produced by KMC-ARS model was able to match some of the hydrogen-to-carbon ratios compared with experiments in different flames. The most recent work from Yapp *et al.* [200] further extended the model to allow the inclusion of five-membered rings and to track the associated change in curvature using the Gauss-Bonnet theorem.

In 2010, Whitesides and Frenklach [193] proposed a detailed chemical-kMC model of graphene-edge growth. Unlike the model used in FSP, the new model incorporated five-membered rings into growing structures, which further allowed for curved molecules to appear. A total of 42 surface transformations were included in the model. The kMC results showed that the curvature occurred regardless of initial substrate at both 1500 K and 2000 K with higher curvature occurring at the lower temperature. No curvature was produced in numerical simulations at 2500 K, indicating that high-energy environments cause the five-membered rings to be less stable. Building from previous work, recent kMC model from Frenklach *et al.* [55] has 111 reactions including simple oxygen chemistry (*i.e.*, the formation of phenols and ring oxidation). In an effort to reproduce recent measurements of soot oxidation rates, it was concluded that additional chemistry, oxidation through complex formation at neighboring surface sites, is required to fully reproduce the experimental observations.

Based on the philosophy of AMPI, Lai *et al.* [96] developed the Stochastic Nanoparticle Simulator (SNapS) model using kMC scheme and Molecular Mechanism (MM) to computationally investigate the growth of nanoparticle precursors through trajectories of chemical reactions. The SNapS simulation was two magnitudes faster than the AMPI on

a single kMC step basis as a result of obviating the use of MD. The SNaPS was able to predict the location and intensity of even-numbered carbon peaks for the mass spectrum of a benzene premixed flame [168] in the range of 200 u to 400 u [96]. The simulation results also exhibited a significant presence of five-membered rings. The SNaPS model was later applied to study the importance of oxygen chemistry. For example, the formation of furan-embedded PACs was emphasized in certain region of the flame [82], and the effect of doping ethanol on the PAC formation was studied by Elvati *et al.* [43] in pure hydrocarbon flames.

There are several limitations to the current stochastic approaches. First of all, the reaction pathways that were proven to be important in certain combustion conditions are missing from these models [82, 28, 147, 152]. In addition, for the reactions included, jump reactions are frequently used (*e.g.*, KMC-ARS model), meaning that the large variety of the intermediates deviated from stabilomers [159] cannot be considered. These limitations make the models incapable of reproducing some of the experimental measurements. Furthermore, the computational performance impedes the simulation of complex two-dimensional flames. Thus, a new stochastic code and a new kinetic mechanism are much needed to address these limitations.

1.5 Scope, Objectives, and Achievements

Understanding the formation of polycyclic aromatic compounds (PACs) in combustion not only bridges the knowledge gap between the small gas-phase species and incipient soot particles, but may also help address the global emission issues of both PACs and soot. In this thesis, I present a kinetic mechanism utilizing reactive sites (*i.e.*, the chemical and physical neighbourhoods) to describe the PAC growth in combustion. This kinetic mechanism was implemented for a stochastic modeling code (*i.e.*, SNaPS2) recently developed by the Violi Group. To address new experimental and computational discoveries, chemi-

cal reactions were gathered and categorized from various literature, while the reaction rate constants came from either literature or my own calculations to ensure full reversibility and thermodynamic consistency. These reactions were then implemented into S_{NapS2} kinetic mechanism with precise reactive site definitions to eliminate the possibility of steric hindrance and unrealistic reactions. Compared with the previous version of S_{NapS2}, thanks to this new kinetic mechanism, the computational performance increased by an order of magnitude, enabling the simulation of complex two-dimensional flames. Some missing reaction pathways, which were identified from experimental evidence and simulations but not available in the literature, were explored and calculated using quantum chemistry methods. These newly discovered reactions were included in the S_{NapS2} kinetic mechanism as well, and some of them were already proven to be important under specific conditions.

The characteristics of the PACs predicted with the kinetic mechanism were compared against different experimental measurements: mass spectra measured in a counterflow diffusion flame, the oxygen-to-carbon ratios obtained at different locations of a coflow diffusion flame, and the molecular structures observed in a premixed laminar flame. These successful validations demonstrate that the S_{NapS2} kinetic mechanism provides a high-fidelity, and yet generic, description of the PAC formation under various combustion conditions, making S_{NapS2} the first-of-its-kind to have such extensive flexibility and wealth of information. It greatly contributes to reveal the underlying chemical pathways to the experimental observations.

Furthermore, S_{NapS2} code and the kinetic mechanism have shown its capability to provide valuable insights on the formation of aromatics beyond the limitation of diagnostics. For one application, spatial dependence of the PAC growth in an ethylene counterflow diffusion flame was characterized by S_{NapS2} simulations, revealing distinct PAC growth pathways for the streamlines starting from fuel side and oxidizer side. Given the fidelity of the S_{NapS2} predictions, it was also used to examine conditions that are impossible to test experimentally, like completely decoupling the effects of flame temperature when study-

ing the effects of ethanol doping on the formation of aromatics, highlighting the chemical pathways that result in soot reduction. Both applications show the uniqueness and great potential of the model to obtain insights of the PAC formation when measurements are hard to obtain or experiments are difficult to control. Altogether, this dissertation lays a solid foundation that not only helps explain the experimental observations for the formation of soot precursors, but also provides a powerful tool for exploring the gas-phase nanoparticle growth that could drive the development of novel combustion technologies or the design of new nanomaterials.

CHAPTER 2

Methodology

Since the SNapS2 code was developed by Dr. Paolo Elvati from the Violi Group, in the following section, I only briefly explain how the SNapS2 code works for clarity, and focus more on the development of the the kinetic mechanism.

2.1 Overview of the SNapS2 Code

Dr. Jason Lai, the main contributor to the SNapS, the previous version of the SNapS2, has provided detailed explanation of the SNapS code [96]. Briefly, SNapS is a kMC code uses the atomic neighborhood (*i.e.*, reactive sites) to describe the chemical reactions. The SNapS generates particle time-histories (*i.e.*, traces) given an initial molecule (*i.e.*, seed) and the gas-phase environment (*i.e.*, temperature, pressure, and gas-phase species mole fractions). When enough traces are generated, it is possible to collect information about the statistical evolution and lifetime of different species, and gather data about the properties of the species at various times. For the molecule to advance a single reaction, the code searches its molecular structure for the reactive sites and makes a list of all the possible reactions that could happen with this molecule from the kinetic mechanism. The code then calculates the probability of reacting for all possible reactions, which has a higher reaction rate would have a higher probability of reacting. Finally the code selects one of the reactions stochastically. The modification of the molecule from the reactant to product was defined in the kinetic mechanism.

While S_{Nap}S2 uses some of the same concepts of S_{Nap}S, it was completely rewritten to obtain better performances and greater flexibility. The major change of the code is the time-dependent solver [67], enabling S_{Nap}S2 code to select reactions not based on the condition at a given time, but all future time as well. Here I also highlight some changes that affected the implementation of the kinetic mechanism. One of the changes is that the kinetic mechanism is separated from the kMC code itself, allowing great flexibility for frequent revision of the kinetic mechanism without affecting the integrity of the kMC code. Another change is the removal of the MM for performance reason, which requires a much more accurate kinetic mechanism, as discussed in later sections. With the new code, the computational performance of S_{Nap}S2 is one magnitude higher than the previous S_{Nap}S on a single KMC step basis, meaning S_{Nap}S2 now can simulate the PAC growth of approximately a million molecules within one week using 48 cores for a premixed laminar flame. This further makes S_{Nap}S2 capable of modeling complex two-dimensional flame (*e.g.*, coflow flame) within a relatively reasonable amount of time.

The S_{Nap}S2 code uses the kinetic mechanism, the gas-phase environment, and seed molecules as inputs, and outputs the time-histories of an ensemble of particles. The S_{Nap}S2 code can be used for simulating the chemical growth in different gas-phase environments, such as combustion, chemical vapor deposition, non-thermal plasma, etc. The kinetic mechanism that is input to the S_{Nap}S2 code determines the system of interest for the simulations. In the scope of this dissertation, the kinetic mechanism is for the PAC growth in combustion systems, and is my main contribution to the S_{Nap}S2 model. A description of the gas-phase environment can be input to the S_{Nap}S2 code, in term of temperature, pressure, and species mole fractions profiles. For combustion applications, these can generally be provided by experimental measurements, CHEMKIN simulations or Computational Fluid Dynamics (CFD) simulations. An important assumption for S_{Nap}S2 is that the growth of the particles have a negligible effect on the gas-phase environment. This assumption generally is reasonable since the amount of particles is relatively small compared

with the small gas-phase species. Thus, the seed molecules, which is the initial molecules for SNapS2 simulations, were selected based on local relative concentrations among a pool of small cyclic compounds (1 to 3 rings) with relatively well-known combustion chemistry (*e.g.*, cyclopentadiene, cyclopentadienyl radical, benzene, phenyl radical, toluene, phenol, phenoxy radical, propylbenzene, naphthalene, acenaphthylene and phenanthrene), as the concentration is directly proportional to the contribution of each species to the final statistical ensemble. Specifically, I chose to select only the molecules with a local concentration within two order of magnitude of the maximum concentration among all the seeds. The output of the SNapS2 code is a sequence of the particle history, including the timestamp of each reaction happened, reaction indices, as well as the description of the resulting molecular structure after each reaction.

2.2 Implementation of the Kinetic Mechanism

The SNapS2 kinetic mechanism includes 396 generic reactions found in the literature, grouped in five broad categories based on formation/breaking of different bond types: carbon-hydrogen bond (C–H), oxygen-hydrogen bond (O–H), carbon-carbon bond (C–C), carbon-oxygen bond (C–O), and isomerization reactions (*i.e.*, hydrogen migrations). Details about these reactions are discussed in the next chapter, Chapter 3. Each reaction is identified with a unique index for simplicity of reference. To make a fully-reversible, thermodynamically-consistent, and sterically-resolved kinetic mechanism that includes major PAC growth pathways, efforts have been put on both the reaction rate constants and the reaction descriptions.

2.2.1 Full Reversibility and Thermodynamic Consistency

The SNapS2 kinetic mechanism is fully-reversible and thermodynamically-consistent in order to improve the accuracy and universality of modeling the PAC growth in different

combustion systems. Full reversibility means that, for every reaction included in the kinetic mechanism, there is a corresponding reverse reaction included as well, no matter how small the reaction rate constants seem to be. Thermodynamic consistency is one step further compared with a fully-reversible mechanism, and is ensured using the following procedure. If the reverse reaction rate constants or equilibrium constants were not available in the literature, I computed the reverse reaction rate constants using the thermodynamics data to ensure thermodynamic consistency, the same as the method implemented in CHEMKIN software [135, 87]. The thermodynamics data are from NASA-format polynomials [17] which have 14 coefficients for one molecule: the first 7 coefficients are for the high-temperature region and the rest 7 coefficients are for the low-temperature range. The enthalpy (H_T°) and entropy (S_T°) at a specific temperature can be calculated according to ref. [17]:

$$\frac{H_T^\circ}{RT} = a_1 + \frac{a_2}{2}T + \frac{a_3}{3}T^2 + \frac{a_4}{4}T^3 + \frac{a_5}{5}T^4 + \frac{a_6}{T} \quad (2.1)$$

$$\frac{S_T^\circ}{R} = a_1 \cdot \ln(T) + a_2T + \frac{a_3}{2}T^2 + \frac{a_4}{3}T^3 + \frac{a_5}{4}T^4 + a_7 \quad (2.2)$$

where, R is the universal gas constant, T is the temperature, a_1 through a_7 are the 7 coefficients in NASA-format polynomials and are different for low- and high-temperature ranges.

Then the following equations were used to compute the reaction rate constant for the reverse reaction ($k_{reverse}$) [17], by calculating the Gibbs free energy (G_T°) and the equilibrium constants (K), and then fitted into the modified Arrhenius form.

$$\Delta_r G_T^\circ = -RT \cdot \ln(K) = \Delta_r H_T^\circ - T \Delta_r S_T^\circ \quad (2.3)$$

$$k_{reverse} = \frac{k_{forward}}{K} \quad (2.4)$$

where, Δ_r sums the products and subtracts the reactants as the change for the whole reaction, $k_{forward}$ is the reaction rate constant for the forward reaction.

Of note, a few single-step reactions included in the kinetic mechanism were combinations of two-step reactions. The reaction rate constants were calculated using steady-state approximation [36], by assuming that the intermediate species are in steady-state, and further fitted into modified Arrhenius form. Efforts were put on to keep as much intermediate species as possible, and only apply steady-state approximation to a few two-step reactions when the intermediate species have no other exits.

2.2.2 Sterically-resolved Reaction Descriptions

SNapS2 utilizes the Simplified Molecular Input Line Entry System (SMILES) [189, 38] to describe molecules, and reactive SMiles ARbitrary Target Specification (SMARTS) [39] to describe the chemical reactions. SMILES, one of the most common tool for molecule description in atomistic modeling, describes the critical information of molecular structure (*e.g.*, atoms, bonds, charges, branching, rings, aromaticity, and chirality) with a short, unique string for easier computational process. SMARTS, similar to SMILES, can describe the reactive sites by searching the sub-structure inside SMILES (*e.g.*, hydroxyl group in phenols). And reactive SMARTS further defines the reaction products by modifying the SMILES of the reacting molecule if the reactive site matches. By using these systems, the molecules were described using SMILES, while each chemical reaction found in the literature was translated into one or more reactive SMARTS depending on the complexity of the reactive sites. As the final result, the 396 generic reactions in the SNapS2 kinetic mechanism was implemented by 430 reactive SMARTS.

Since the implementation of reactive SMARTS require the description of reactive sites, not species (*e.g.*, CHEMKIN software), a number of items need to be carefully examined and specified. Examples of a few different scenarios that could occur during the implementation of the kinetic mechanism are shown in Figure 2.1.

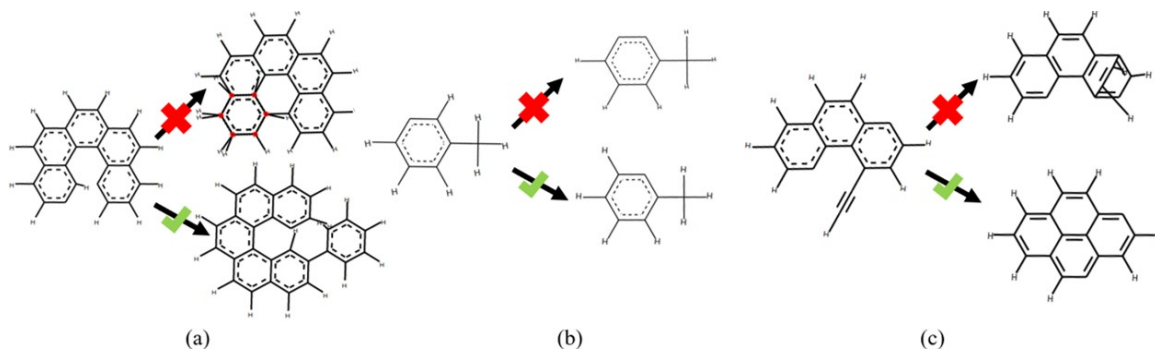


Figure 2.1: Examples of scenarios for the site selections in the SNaPS2 kinetic mechanism: (a) steric hindrance in phenyl radical addition reaction; (b) unrealistic reaction of hydrogen abstraction for creating a second radical electron on a single aromatic ring; and (c) improper ring closure. Arrows labeled with cross are the reactions need to be ruled out; arrows labeled with tick are the possible reactions being selected instead.

Figure 2.1 (a) shows a possible steric hindrance case for phenyl radical addition reaction, where one of the reactive sites is blocked by other atoms in the molecule. This would slow down, even prevent the reaction from happening. Figure 2.1 (b) shows a possible unrealistic reaction of hydrogen abstraction for creating a second radical electron on a single aromatic ring. Once an aromatic six-membered ring already has a radical site, the fast hydrogen migration can occur while a second hydrogen abstraction is usually unrealistic, which would form a biradical inside the same aromatic six-membered ring. Figure 2.1 (c) shows a possible improper ring closure. All of these are challenges for the reaction implementation.

In SNaPS code [96], a process called "rejection" is used to rule out these cases, as the flow chart shown on the left of Figure 2.2. These reactions are allowed to happen first, and then the wrong ones are rejected by utilizing MM. The change in potential energy for the reacting and product molecules is computed as part of the rejection process. Since steric hindrance, unrealistic reactions, and improper ring closures will result in an extreme increase in the potential energy change, these products are discarded based on a preset threshold. Then SNaPS code rejects the reaction, reselects another one and checks again. This rejection process takes about 90% of the SNaPS computational time.

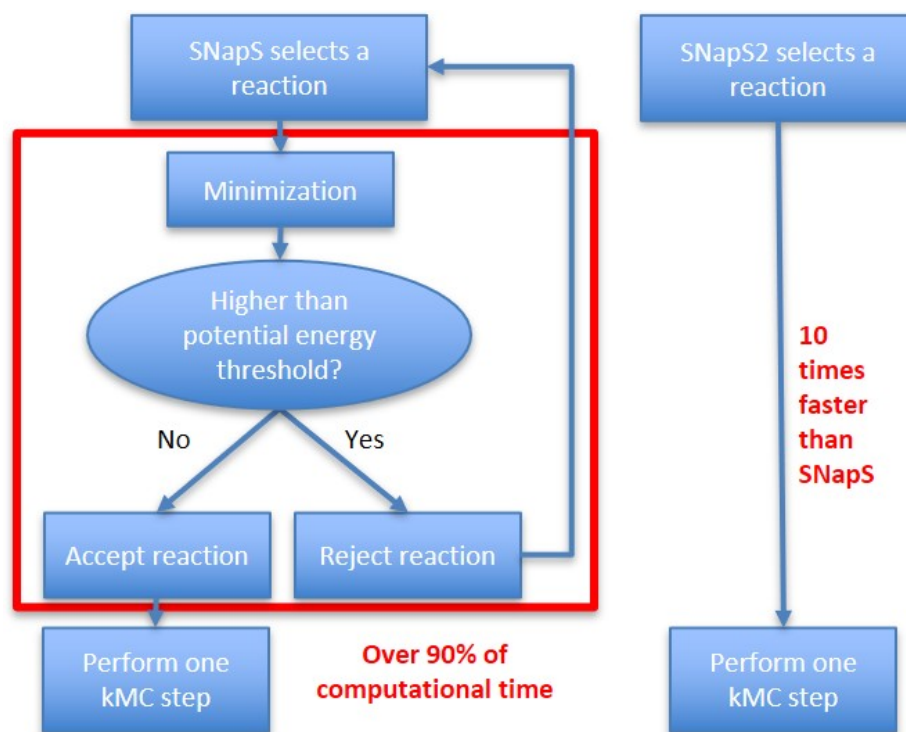


Figure 2.2: Comparison of the reaction selection process between SNaPS code and SNaPS2 code. The left side is the process for SNaPS code, and the right side is the process for SNaPS2 code. The process inside the red box is the reaction rejection process for SNaPS code, which is completely removed to improve the computational performance in SNaPS2 code.

With SNaPS2 code, MM is abandoned to improve the computational performance, and instead, the burden is completely on the implementation of the kinetic mechanism to prevent these reactions from happening. The site definitions were greatly expanded in the SNaPS2 kinetic mechanism to make sure that each reaction relies on sufficient description of atomic neighborhoods to rule out steric hindrance and unrealistic reactions, not external energy calculations. For example, Figure 2.1 (a) needs the reaction rejection process in the SNaPS code to rule out the wrong one [96]. Now with the recognition of the bay-site aromatic carbon [14] (as shown in Figure 2.3) in the site description of the SNaPS2 kinetic mechanism, reactive SMARTS eliminates the possibility of having the bay-site aromatic carbons as possible reactive sites for the phenyl addition, and the reaction can only happen with free-edge aromatic carbons. This expansion of site definitions prevents steric

hindrance scenario from the root causes. For Figure 2.1 (b), these hydrogen abstraction reactions were specified in SNapS2 kinetic mechanism, so that if a radical electron already appears on an aromatic ring, hydrogen abstraction will not happen on the same ring again. The hydrogen migration could happen however, to transfer the radical site along the aromatic ring. Figure 2.1 (c), both outcomes are allowed by SNapS without the rejection process [96], while SNapS2 kinetic mechanism specifies the armchair site [131] sufficiently to eliminate the improper ring closure. With better site definitions in the kinetic mechanism, the SNapS2 code is able to perform 10 times faster than the SNapS code for a single kMC step.

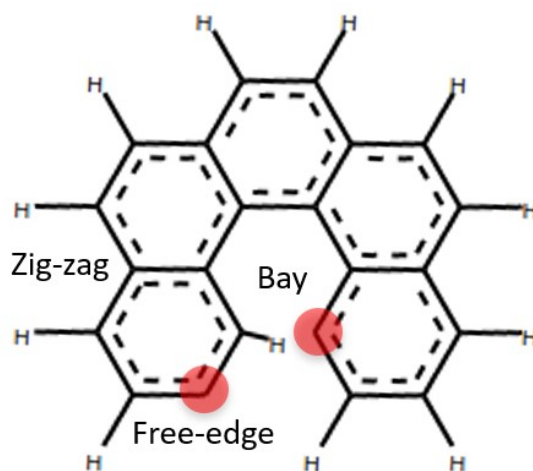


Figure 2.3: Example of better site definition in the SNapS2 kinetic mechanism. SNapS2 kinetic mechanism can recognize the bay-site aromatic carbon, free-edge aromatic carbon, as well as zig-zag aromatic carbon.

As the result of these processes, a fully-reversible, thermodynamically-consistent, and sterically-resolved kinetic mechanism was implemented for SNapS2 code, describing 396 generic reactions with 430 reactive SMARTS that include major PAC growth pathways. In the next chapter, I discuss the details of the generic reactions included in the kinetic mechanism, and the rationales behind the selection of these reactions and rate constants.

CHAPTER 3

A Kinetic Mechanism for the Formation of PACs in Combustion

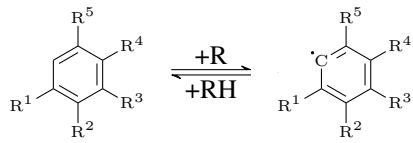
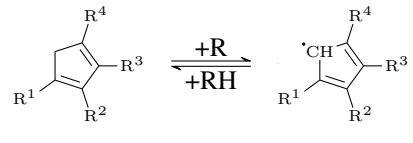
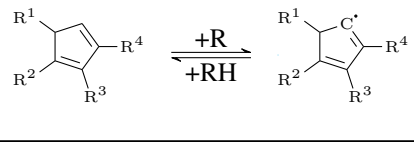
In this Chapter, I present a fully-reversible, thermodynamically-consistent, and sterically-resolved kinetic mechanism describing PAC growth in combustion with 396 generic reactions implemented by 430 reactive SMARTS. I discuss the details of the reaction pathways included in the kinetic mechanism, and the rationales behind the selection of these reactions and rate constants. The reaction were grouped in five broad categories based on formation/breaking of different bond types: carbon-hydrogen bond (C–H), oxygen-hydrogen bond (O–H), carbon-carbon bond (C–C), carbon-oxygen bond (C–O), and isomerizations (hydrogen migrations).

3.1 Carbon-Hydrogen Reactions

The carbon-hydrogen reaction category includes the reactions for carbon and hydrogen bond breaking and forming: the hydrogen abstraction and disproportionation from different chemical neighborhoods of carbon atoms, as well as the hydrogen addition as reverse. This category consists of 11 subcategories. Three of which are listed in Table 3.1: hydrogen abstraction from (reversely, addition to) six-membered aromatic carbon and five-membered carbon ring. Seven of which are listed in Table 3.2: methyl group, α -hydrogen of ethyl group, α -hydrogen of isopropyl group, β -hydrogen of vinyl group, α -hydrogen of

vinyl group, alkynyl group, and vinyl to alkynyl group. The last subcategory (indexed with CHb/f1b) which is not listed in this section, is for the formation of ring closure intermediates. These are shown in later tables grouped with ring closure reactions for clarity.

Table 3.1: Reaction schemes for carbon-hydrogen reaction category part I: reactions for cyclic carbon sites

Generic Reaction	Index	Gas-phase*	Reference
	CHb/f111-8	H, O, OH O ₂ , HO ₂ , CH ₃ C ₂ H ₃ , none	[57, 97, 90] [8, 6, 90] [134, 119]
	CHb/f121-8	H, O, OH O ₂ , HO ₂ , CH ₃ C ₂ H ₃ , C ₆ H ₅	[191, 134]
	CHb/f131-3	H, C ₂ H ₃ , none	[55, 134]

* Gas-phase species indicate the secondary reactant for (forward) bimolecular reactions and "none" is used for (forward) unimolecular reaction.

While hydrogen abstraction by atomic hydrogen (H) [177, 21] has been extensively studied because the high reaction rate constants and the abundance of H make it central in HACA pathways [52, 53, 57], quantum chemistry calculations were also carried out over decades for hydrogen abstraction reactions by other species, such as atomic oxygen (O) [24], oxygen molecule (O₂) [89], hydroxyl radical (OH) [122], hydroperoxyl radical (HO₂) [22, 7], methyl radical (CH₃) [78], and vinyl radical (C₂H₃) [134]. These reactions, as well as the hydrogen dissociation [119], are included in this mechanism to handle different gas-phase environments.

For aromatic six-membered ring (CHb/f11 subcategory), *ortho*-, *meta*-, and *para*-sites may influence the reaction rate constants depending on the attached functional group, as shown by Bao *et al.* [11] for the hydrogen abstraction from toluene. While abstracting

Table 3.2: Reaction schemes for carbon-hydrogen reaction category part II: reactions for open-chain carbon sites

Generic Reaction	Index	Gas-phase*	Reference
$R^1- \xrightleftharpoons[+RH]{+R} R^1-\dot{C}H_2$	CHb/f141-8	H, O, OH O ₂ , HO ₂ , CH ₃ C ₂ H ₃ , none	[169, 25, 125] [77, 169, 3, 169] [134, 77]
$R^1-\text{CH}_2- \xrightleftharpoons[+RH]{+R} R^1-\dot{C}H-$	CHb/f151-8	H, O, OH O ₂ , HO ₂ , CH ₃ C ₂ H ₃ , none	[169, 25, 125] [125, 3, 169] [134, 77]
$R^1-\text{CH}=\text{CH}- \xrightleftharpoons[+RH]{+R} R^1-\dot{C}H-\text{CH}=\text{CH}-$	CHb/f161-8	H, O, OH O ₂ , HO ₂ , CH ₃ C ₂ H ₃ , none	[125, 191] [125, 76, 3, 191] [134, 191]
$R^1= \xrightleftharpoons[+RH]{+R} R^1=\dot{C}H$	CHb/f171-8	H, O, OH O ₂ , HO ₂ , CH ₃ C ₂ H ₃ , none	[121, 170, 18, 210, 174] [18, 70, 191, 148, 170] [134, 124]
$R^1-\text{CH}=\text{CH}- \xrightleftharpoons[+RH]{+R} R^1-\dot{C}H-\text{CH}=\text{CH}-$	CHb/f181-8	H, O, OH O ₂ , HO ₂ , CH ₃ C ₂ H ₃ , none	[121, 170, 18, 210, 174] [18, 70, 191, 148, 170] [134, 124]
$R^1\equiv \xrightleftharpoons[+RH]{+R} R^1\equiv\dot{C}$	CHb/f191-7	H, O, OH O ₂ , HO ₂ , CH ₃ C ₂ H ₃	[85, 77, 191] [136, 110] [134]
$R^1=\dot{C}H \xrightleftharpoons[+RH]{+R} R^1\equiv$	CHb/f1a1 CHb/f1a2	H none	[90] [90]

* Gas-phase species indicate the secondary reactant for (forward) bimolecular reactions and "none" is used for (forward) unimolecular reaction.

hydrogen from *ortho*- and *para*-sites of the toluene has reaction rate constants close to hydrogen abstraction from benzene, the rate constants for *meta*-site hydrogen abstraction are much higher. Phenol, in contrast, makes *ortho*-site and *para*-site abstractions the major

routes. I recently compared the differences in rate constants for the hydrogen abstraction by H from benzene and from *ortho*-site of phenylethene, phenylacetylene, and phenol [152]. Results show that the reaction rate constants are within an order of magnitude between 500 K and 2000 K, with the highest rate constants being benzene and the lowest being phenylethene.

The major issue in extending these site effects beyond simple molecules is that, for complex PACs, an unrealistically complex characterization is needed since the number of possible site increases exponentially. In addition, the *ortho*-, *meta*-, and *para*-sites become arbitrary even for simple molecules (*e.g.*, trimethylbenzene). Thus, I gathered literature on these site effects to determine whether or not the difference is large enough (more than one magnitude) to be added into the mechanism. One example is the CCf112 reaction discussed in later section.

While the distinctions of reaction subcategories CHb/f14 to CHb/f19 are for site effects of different types of aliphatic carbons, the influence of replacing R¹ with aromatic ring was also compared from the literature. Comparing with reaction CHb141 which yields $9.83 \times 10^{12} \text{ cm}^3 \text{ mol}^{-1} \text{ s}^{-1}$ at 2000 K, substituting R¹ with benzene (*i.e.*, hydrogen abstraction by H from the methyl group of toluene) gives $1.28 \times 10^{13} \text{ cm}^3 \text{ mol}^{-1} \text{ s}^{-1}$ at 2000 K, showing that the difference is marginal.

CHb/f1a is the reaction subclass describing the formation of alkyne from vinyl radical by Direct Hydrogen Elimination (DHE) or Hydrogen Disproportionation (HD) reactions. This reaction subcategory is an important step of the major pathway for the HACA, after attaching an acetylene to the aromatic carbon site. Through this reaction, ethenylphenyl radical further evolves into the more stable molecule, phenylacetylene, and waits for a second acetylene to attach and eventually closes a ring.

CHb/f1b is the reaction subclass forming an aromatic bond from a single, cyclic bond by direct hydrogen elimination (*i.e.*, disassociation) or hydrogen disproportionation reactions. These reactions usually form stable aromatic structures from intermediates. Because

of its close relationship with ring closure reactions, these CHb/f1b are included in the tables of later section for reactions forming five- and six-membered rings.

In addition, rate estimations for groups of reactions have been developed in various studies. Violi *et al.* [177] utilized reaction class transition state theory/linear energy relationship to evaluate the rate constants of hydrogen abstraction reactions by H atoms from classes of aromatics. Carstensen *et al.* [21] established a relatively simple protocol to estimate rate constants of hydrogen abstraction reactions by H atoms from alkanes, cycloalkanes, and allylic systems. Raman *et al.* [134] later employed these concepts and extended the study to H abstraction by vinyl radicals. For the purpose of this dissertation, I assigned the same set of reaction rate constants for a given reaction regardless of the size of the molecule. But in principle, this kinetic mechanism can be expanded using above techniques.

3.2 Oxygen-Hydrogen Reactions

Similar to carbon-hydrogen reactions category, the oxygen-hydrogen reaction category includes the reactions for oxygen and hydrogen bond breaking and forming: the hydrogen abstraction from hydroxyl group, as well as the hydrogen addition to oxygen as reverse. This category includes three subcategories listed in Table 3.3: hydrogen abstraction from (reversely, addition to) the oxygen which attached to aromatic carbon, aliphatic cyclic carbon (specifically five-membered ring), and aliphatic acyclic carbon.

The site effects of hydrogen abstraction from hydroxyl group are simpler than C-H category, thus the hydroxyl group is further categorized into phenols (OHb/f11) and alcohols (OHb/f12 and OHb/f13). As a comparison, the reaction rate constants for OHb111, OHb121, and OHb131 (*i.e.*, hydrogen abstraction by H from different hydroxyl sites) are $5.1 \times 10^{12} \text{ cm}^3 \text{ mol}^{-1} \text{ s}^{-1}$, $8.6 \times 10^{12} \text{ cm}^3 \text{ mol}^{-1} \text{ s}^{-1}$ and $4.0 \times 10^{12} \text{ cm}^3 \text{ mol}^{-1} \text{ s}^{-1}$ respectively at 2000 K. The difference is quite small. Since these reactive sites were simple to

Table 3.3: Reaction schemes for oxygen-hydrogen reaction category

Generic Reaction	Index	Gas-phase*	Reference
	OHb/f111-9	H, O, OH O ₂ , HO ₂ , CH ₃ C ₂ H ₃ , C ₆ H ₅ , none	[75, 47, 150] [8, 7, 191] [47, 49, 198]
	OHb/f121-4	H, O, OH, HO ₂	[191]
$R^1-O \xrightleftharpoons[+RH]{+R} R^1-O\cdot$	OHb/f131-6	H, O OH, O ₂ HO ₂ , CH ₃	[126, 194] [208, 146] [209, 199]

* Gas-phase species indicate the secondary reactant for (forward) bimolecular reactions and "none" is used for (forward) unimolecular reaction.

specify by reactive SMARTS, distinguishing them would not significantly increase computational cost. I chose to keep these site effects for better accuracy.

Similar to the discussion above regarding the activation of HACA pathways, hydrogen abstractions from the hydroxyl group of phenols and alcohols are the important activation step for the oxygen chemistry, which may further lead to the formation of ketones (*i.e.*, COf/b14) and furans (*i.e.*, COf/b15) discussed in later sections.

3.3 Carbon-Carbon Reactions

The carbon-carbon reaction category includes the reactions for aromatic and/or aliphatic carbon bond breaking and forming: the carbon fragments addition/abstraction listed in Table 3.4, five-membered ring formation/breaking listed in Table 3.5, six-membered ring formation/breaking via HACA pathways listed in Table 3.6 and via other pathways listed in Table 3.7, as well as ring conversion from/to five-membered to/from six-membered ring listed in Table 3.8.

Table 3.4: Reaction schemes for carbon-carbon reaction category part I: reactions for carbon fragments addition/abstraction to/from aromatic or aliphatic carbon

Generic Reaction	Index	Gas-phase*	Reference
$\text{C}_6\text{H}_5\text{R}^1\text{R}^2\text{R}^3\text{R}^4\text{R}^5 \cdot \xrightleftharpoons[+\text{H}]{+\dot{\text{R}}^6/+\text{R}^6\text{H}} \text{C}_6\text{H}_5\text{R}^1\text{R}^2\text{R}^3\text{R}^4\text{R}^5\text{R}^6 \cdot$	CCf/b111-b CCf/b212	CH ₃ , C ₂ H ₂ , C ₂ H ₃ C ₂ H ₄ , C ₃ H ₃ , $\mathcal{A}\text{C}_3\text{H}_4$ $\mathcal{P}\text{C}_3\text{H}_4$, C ₃ H ₆ , C ₄ H ₄ C ₆ H ₅ , C ₆ H ₆ C ₂ H ₂ R ¹ is O-H	[139, 103, 139] [139, 130, 117] [117, 115] [139] [152]
$\text{C}_4\text{H}_3\text{R}^1\text{R}^2\text{R}^3\text{R}^4 \cdot \xrightleftharpoons[+\text{H}]{+\dot{\text{R}}^5/+\text{R}^5\text{H}} \text{C}_4\text{H}_3\text{R}^1\text{R}^2\text{R}^3\text{R}^4\text{R}^5 \cdot$	CCf/b121-2	CH ₃ , C ₂ H ₂	[185, 103]
$\text{R}^1-\dot{\text{C}}\text{H}_2 \xrightleftharpoons[+\text{H}]{+\dot{\text{R}}^2/+\text{R}^2\text{H}} \text{R}^1-\text{C}-\text{R}^2$	CCf/b131-8	CH ₃ , C ₂ H ₂ , C ₂ H ₃ C ₂ H ₄ , C ₃ H ₃ , $\mathcal{P}\text{C}_3\text{H}_4$ C ₆ H ₅ , C ₆ H ₆	[185, 117] [185] [139, 185]
$\text{R}^1-\text{CH}=\dot{\text{C}}\text{H} \xrightleftharpoons[+\text{H}]{+\dot{\text{R}}^2/+\text{R}^2\text{H}} \text{R}^1-\text{CH}=\text{CH}-\text{R}^2$	CCf/b141-5	CH ₃ , C ₂ H ₂ , C ₂ H ₃ C ₂ H ₄ , C ₆ H ₅	[185, 90] [185, 139]

* Gas-phase species indicate the secondary reactant for (forward) bimolecular reactions. "R¹ is O-H" means that this reaction rate is specifically used when the functional group R¹ is hydroxyl group.

Acetylene addition to the aromatic six-membered ring is a major step for both the HACA pathways (Table 3.6) and the formation of furan-embedded PACs (Table 3.10). However as I recently shown in ref. [152], the C₂H₂ addition to different reactive sites (*e.g.*, phenyl or 2-hydroxybenzene) makes a difference in the reaction rate constants as much as two orders of magnitudes at 2000 K. For this reason, I included two generic reactions for C₂H₂ addition: CCf212 when there is a hydroxyl group presents in *ortho*-site, which is the key step for furan rings formation [152], and CCf112 for all other cases, such as the HACA growth pathways [103].

In many combustion systems, there is generally a higher concentration of C₂H₂ than other small carbonaceous species (*e.g.*, C₃ and C₄ species). However, I also included other

Table 3.5: Reaction schemes for carbon-carbon reaction category part II: reactions for five-membered hydrocarbon ring formation/breaking

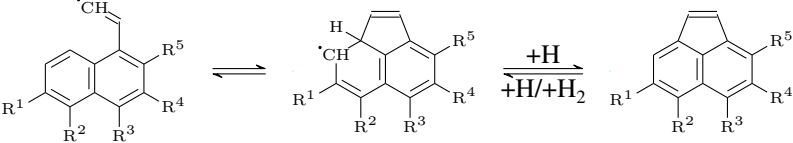
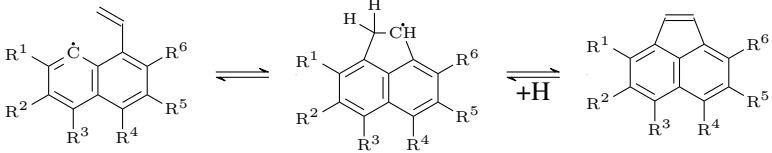
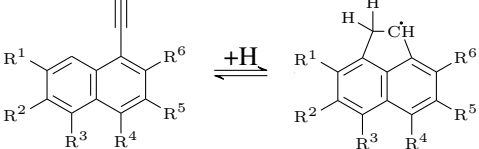
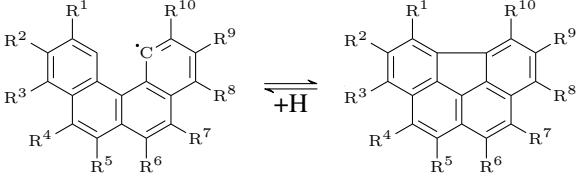
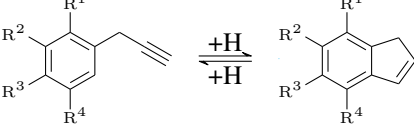
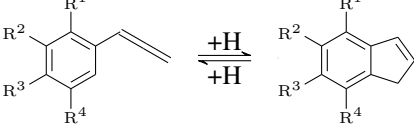
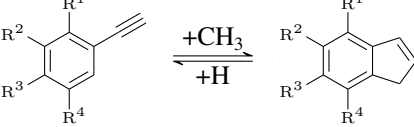
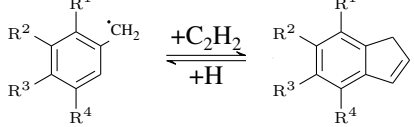
Generic Reaction	Index	Reference
	CCf/b151 CHb/f1b1 CHb/f1b2	[103] [103] [90]
	CCf/b152 CHb/f1b3	[56] [56]
	CCf/b153	[55]
	CCf/b154	[176, 131]
	CCf/b155	[117]
	CCf/b156	[117]
	CCf/b157	[117]
	CCf/b158	[117]

Table 3.6: Reaction schemes for carbon-carbon reaction category part III: reactions for six-membered ring formation/breaking through HACA pathways

Generic Reaction	Index	Ref.
	CCf/b161 CHb/f1b4 CHb/f1b5	[90] [90] [90]
	CCf/b162 CHb/f1b6 CHb/f1b7	[103] [103] [90]
	CCf/b163	[103]
	CCf/b164 CHb/f1b8 CHb/f1b9	[92] [92] [92]
	CCf/b165 CHb/f1ba CHb/f1bb	[92] [92] [92]
	CCf/b166	[92]
	CCf/b167	[52]

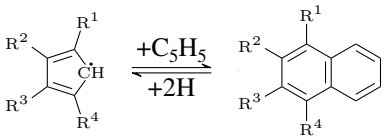
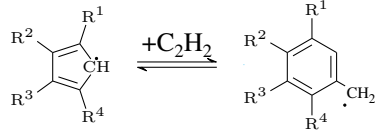
growth mechanisms which involves the addition of many gas-phase species for comparisons in different environments. Allene ($\mathcal{A}C_3H_4$) addition (CCf116) and propyne ($\mathcal{P}C_3H_4$)

Table 3.7: Reaction schemes for carbon-carbon reaction category part IV: reactions for six-membered ring formation/breaking through pathways other than HACA

Generic Reaction	Index	Reference
	CCf/b168	[90]
	CCf/b169	[90]
	CCf/b16a	[131]
	CCf/b16b	[115]
	CCf/b16c	[34]
	CCf/b16d	[115]

addition (CCf117) to the aromatic ring could be the first step for the PAC growth initiated by C_3 species, and may be followed by five-membered ring closure reactions described by CCf155 and CCf156 [117], while vinylacetylene addition could initiate the C_4 species growth [115, 104] with six-membered ring closure of CCf16b. Addition of a phenyl radi-

Table 3.8: Reaction schemes for carbon-carbon reaction category part V: reactions for ring conversion from five-membered to six-membered hydrocarbon ring

Generic Reaction	Index	Reference
	CCf/b171	[123]
	CCf/b172	[30]

cal (CCf11a and CCf11b) introduces the biphenyl-type armchair site, which may then go through directly Diels-Alder pathways (CCf168), or HACA pathways (CCf164 to CCf166) when an C_2H_2 is attached, or dibenzofuran-type pathways (COf159 to COf15d) when an oxygen atom is attached.

Furthermore, addition of the first aliphatic chain to the aromatic ring (CCf111 to CCf119) could initiate the aliphatic chain growth described by subcategories CCf13 and CCf14. Experimental evidences suggest that aliphatic chains exist in both soot precursors (PACs) [147, 28] and nascent soot surfaces [20]. Subcategories CCf13 and CCf14 provide the aliphatic carbon growth chemistry to study the competitive roles of aliphatic and aromatic growth in different environments.

The acetylene addition to five-membered ring (CCf122) was estimated to be the same as the addition on the six-membered aromatic ring (CCf112). This further allows the pathway to form curved PACs [193, 200, 111] (*e.g.*, corannulene) through HACA mechanism. Indeed, the chemistry of PACs started with cyclopentadiene or cyclopentadienyl radical needs to be further studied.

Table 3.5 includes the subcategory of five-membered ring formation through HACA pathways (CCf151 to CCf153), bay closure (CCf154), C_3 growth (CCf155 and CCf156), and other pathways (CCf157 and CCf158). As mentioned in the introduction, many PAC

kinetic mechanisms combined multi-step reactions using the steady-state approximation to skip the formation of intermediates and only focus on aromatic structure growth. While I used the steady-state approximation a few times to treat reactions which are too complex for implementation (*e.g.*, CCf154) when the intermediates have no other exits, I also preserved the intermediates chemistry as much as possible since some intermediates might be important from experimental observations: from recent studies of high-resolution AFM images of soot samples [28], an appreciable number of aromatic molecules incorporating different types of five-membered rings were observed, namely: acenaphthylene-type, acenaphthene-type, fluorene-type and indane-type. The acenaphthene-type specifically, may come from the intermediates after CCf152 and CCf153 reactions: instead of losing one hydrogen (CHb1b3), it may add one more hydrogen (CHf12) and become acenaphthene-type five-membered ring. Thus keeping these intermediates would help understand the experimental observations and improve modeling predictions.

Six-membered ring formation by HACA pathways have been included for both free-edge (CCf/b161/2/3) and armchair sites (CCf/b164/5/6/7) by attaching two or one C_2H_2 respectively, listed in Table 3.6. Introduced by Frenklach and coworkers [54] from shock-tube pyrolysis of acetylene, HACA pathways are now considered to be the driven mechanism for pure hydrocarbon PACs formation in many conditions [58, 53, 56, 57]. Pathway CHb111 – CCf112 – CCf142 – CCf161 specifically is the Bittner-Howard's route [13] of the HACA pathways, computed by Kislov *et al.* [90]. In addition, the site effects of HACA pathways has been recently discussed by Liu *et al.* [103].

Six-membered ring formation by other pathways, namely Diels-Alder, bay closure, growth initiated by C_3 species and by C_4 species, have been listed in Table 3.7. Diels-Alder pathway [155, 90], listed as CCf167 and CCf168 reactions, does not involve radical species during the growth. The acetylene is directly added to form intermediate, and then H_2 leaves, forming the more stable molecule. C_3 growth initiated by propargyl radical has been studied by Raj *et al.* [130], and C_4 growth initiated by vinylacetylene has been

recently studied by Liu *et al.* [104]. However, both articles include multiple steps and intermediates which are too redundant to consider all. For simplification, I used the work from D'Anna [34] and Mebel [115] as one-step reaction listed as CCf16a and CCf16b.

The self-combination of cyclopentadienyl radical (CCf171) as a source for forming naphthalene has long been studied [123, 118, 106]. A single net rate expression was first established by Murakami *et al.* [123] through experiments to describe a direct conversion. Later studies found that the process is quite complex, which involves tens of intermediates [118]. A more recent study [106] with the pressure dependent kinetic analysis, observed that $C_{10}H_{10}$ is a long-live species which may enter $C_{10}H_9$ surface with H abstraction, and a detailed sub-mechanism describing the whole process was provided within. In my mechanism for simplification, I still used a single rate expression (CCf/b171) by Murakami *et al.* [123] for describing the conversion.

3.4 Carbon-Oxygen Reactions

The carbon-oxygen reaction category includes the reactions for aromatic or aliphatic carbon bond breaking and forming with oxygen: the oxygen addition/abstraction to/from carbon and carbon fragments addition/abstraction to/from oxygen listed in Table 3.9, furan ring formation/decomposition listed in Table 3.10, as well as five- and six-membered ring oxidation listed in Table 3.11.

While almost all of the combustion systems use oxygen as oxidizer, it is only in recent years that large oxy-PACs as combustion byproduct started to get more of attentions [82, 43, 46, 44, 64]. Several recent papers [157, 82, 43, 182] have revealed the importance of including the oxygen chemistry of the PACs in order to explain the experimental observations. Elvati *et al.* [45, 43, 46, 44] indicated that the dimerization of PACs in general is affected by the shape of the molecules as well as the oxygen content, and that oxygenated species have less tendency to aggregate than pure hydrocarbons. Thus a

Table 3.9: Reaction schemes for carbon-oxygen reaction category part I: reactions for oxygen addition/abstraction to/from carbon and carbon fragments addition/abstraction to/from oxygen

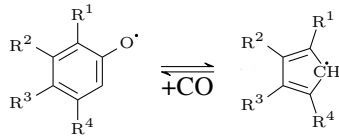
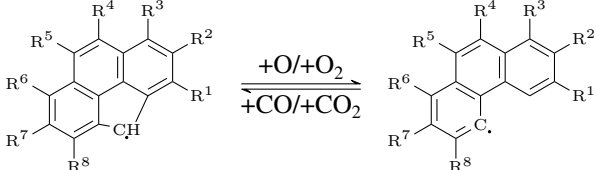
Generic Reaction	Index	Gas-phase*	Reference
	COf/b111-3	OH, O ₂ , HO ₂	[24, 55, 191]
	COf/b114	OH	[55]
	COf/b115	O	[24]
	COf/b116	OH	[24]
	COf/b121-4	CH ₃ , C ₂ H ₂ C ₂ H ₃ , C ₆ H ₅	[24, 171, 139, 152] [139]
	COf/b131	HO ₂	[191]
	COf/b132	O	[191]
	COf/b133-6	O, OH, O ₂ , HO ₂	[24, 60, 207]
	COf/b141-3	R ⁵ is O• R ⁵ is O-O• R ⁵ is O-OH	[207]

* Gas-phase species indicate the secondary reactant for (forward) bimolecular reactions. For COf/b14 subcategory specifically, the atoms listed in the gas-phase are to replace R⁵ in the reactant of the forward direction of the unimolecular reaction.

Table 3.10: Reaction schemes for carbon-oxygen reaction category part II: reactions for five-membered furan ring formation/breaking

Generic Reaction	Index	Reference
	COf/b151 CHb/f1bc-d	[152]
	COf/b152 CHb/f1be-f	[152]
	COf/b153 CHb/f1bg-h	[152]
	COf/b154-5	[152]
	COf/b156	[152]
	COf/b157-8	[191]
	COf/b159-a	[152]
	COf/b15b-c	[152]
	COf/b15d	[152]

Table 3.11: Reaction schemes for carbon-oxygen reaction category part III: reactions for ring oxidation

Generic Reaction	Index	Reference
	COb/f161	[191]
	COb/f162-3	[55]

mechanism including the oxy-PAC formation would further help to understand these effects during the transition of small gas-phase species to soot particles.

The subcategory COf11 contains the reactions describing the bonding of oxygen on aromatic rings, which may lead to the formation of ethers (COf12). The reaction rate constants for vinyl (COf123) and phenyl (COf124) bonding with another phenyl is estimated to be the same as methyl reacting with phenyl (COf121), since three reactions are all radical-radical combination reactions [81]. The C₂H₂ addition to the phenoxy was recently computed as a possible pathway for the formation of furans (COf151 and COf152) [152].

The reaction subcategory COf13 is for attaching the oxygen onto five-membered rings, which may further go through the formation of ketones in subcategory COf14. Zhong and Bozzelli [207] studied the atomic hydrogen, hydroxyl radical, hydroperoxyl radical, atomic oxygen, and oxygen molecule association reactions with cyclopentadienyl radical, including the formation of cyclopentadienone from various species. While the ketones are not formed by a lot at high temperatures in combustion suggested by some experimental data [82], including these pathways would further complete the scope of oxygen chemistry in my PAC kinetic mechanism.

Various experiments [128, 179, 201] have measured the benzofuran mole fraction pro-

files and confirmed its significant presence. Johansson *et al.* [82] proposed a pathway for forming benzofuran through acetylene addition to phenoxy radical. Later PAC models implemented this pathway found that furan-embedded PACs indeed show up significantly at certain region of the flame where both atomic oxygen and C_2H_2 concentrations are high [43, 182]. Our recent *ab initio* study extended the formation pathways of benzofuran to a total of six routes and proposed three new dibenzofuran [152] formation pathways. These newly computed pathways have been included in this mechanism in Table 3.10.

Table 3.11 includes the oxidation of five- and six-membered rings. Five-membered ring oxidation with gas-phase species atomic oxygen and oxygen molecule (COb162 and COb163) has been studied recently by Frenklach and Mebel [55, 60]. These oxidation reactions provide a possible exit for fluorene-type five-membered rings [28] discussed before.

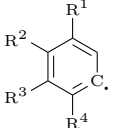
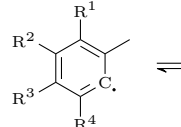
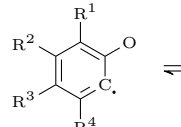
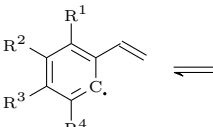
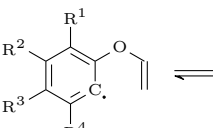
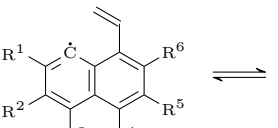
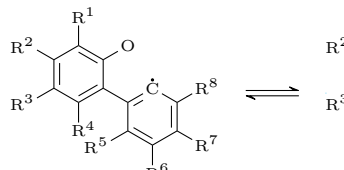
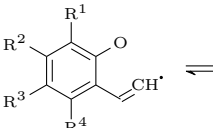
3.5 Isomerizations

The isomerization reactions happening during the ring formation/breaking process have been previously discussed, this category focuses on the reactions for hydrogen migration. This category includes four subcategories listed in Table 3.12: hydrogen migration between aliphatic acyclic atoms, between aromatic cyclic atoms, between aliphatic and aromatic atoms, as well as between aliphatic acyclic atoms with the presence of aromatic rings.

The isomerization between $\mathcal{P}C_3H_4$ and $\mathcal{A}C_3H_4$ (Iso/Irv111) is a common hydrogen migration reaction in nature, and is important to bridge some of the reaction pathways in this mechanism (*e.g.*, C_3 growth in CCf155 and CCf156). Davis *et al.* [37] provided the Rice–Ramsperger–Kassel–Marcus rate coefficient parameters for $\mathcal{P}C_3H_4$ to $\mathcal{A}C_3H_4$ isomerization reaction, while Miller and Klippenstein [120] reported the reverse. The isomerization in both direction are studied by Giri *et al.* [68], compared with the competing role of decomposition.

Reaction Iso121 accommodates hydrogen migration along a single aromatic ring. Hy-

Table 3.12: Reaction schemes for isomerization reaction category

Generic Reaction	Index	Reference
$R^1-C-C\equiv C \rightleftharpoons R^1-C=C=C$	Iso/Irv111	[68, 120, 37]
	Iso/Irv121	[32]
	Iso/Irv131	[32]
	Iso/Irv132	[152]
	Iso/Irv133	[90]
	Iso/Irv134	[152]
	Iso/Irv135	[56]
	Iso/Irv136	[152]
	Iso/Irv141	[152]

hydrogen abstraction from an aromatic ring which already contains a radical site is not allowed in CHb11 subcategory, since the hydrogen migration is much more often than a

second hydrogen abstraction. Dames and Wang [32] studied isomerization kinetics of benzylic and methylphenyl type radicals in single-ring aromatics, including the ring H-shifting described by reaction Iso121.

The isomerization between the phenylethene radical and 2-phenylethene radical (Irv133) is a step on the minor route of the HACA mechanism. While the dominant route of the HACA mechanism forms phenylacetylene from the phenylethene radical through CHb1a1/2 reactions, the minor route can be achieved by this isomerization to preserve the vinyl group before the second C₂H₂ addition.

The isomerization reaction Iso134 can bridge the furan formation pathway COf151 and COf152. Similarly, reaction Iso136 connects the furan formation pathway COf159/a and COf15b/c; and reaction Iso141 links the furan formation pathway COf153 and COf154/5. Detailed pathways have been discussed by Shi *et al.* [152].

CHAPTER 4

Exploring Missing Reaction Pathways

During the literature review for the S_{Nap}S₂ kinetic mechanism, several missing reaction pathways emerged. Together with Dr. Xuetao Shi, we were able to extensively study these reaction pathways for the formation of benzofuran and dibenzofuran [152], as well as types of five-membered rings [153]. Since the quantum chemistry calculations were carried out by Dr. Xuetao Shi, in the following section I mainly discuss the reaction pathways that I proposed, and the impact of these new reaction pathways on the formation of PACs. The following sections are adapted from these publications [152, 153].

4.1 The Formation of Benzofuran and Dibenzofuran

Recent studies have reported the presence of oxy-PACs in flames [82, 43, 19, 27, 26], and highlighted their role in soot formation [40, 99, 79, 80, 195, 113, 162, 142, 43, 46, 44, 64, 182]. One of the simplest among the oxy-PACs is furan, which is a heterocyclic organic compound, consisting of a five-membered aromatic ring with four carbon atoms and one oxygen atom. Furan has been thoroughly studied in high-temperature regimes due to its simple structure and broad applications [107, 149, 50, 188, 173, 197, 4, 105, 196, 187, 100, 166]. However, limited information is available on larger oxy-PACs containing furan unit, such as benzofuran and dibenzofuran, in which case furan ring is condensed with one or two benzene rings. Recent experiments revealed the importance of benzofuran and dibenzofuran in various conditions: Yuan *et al.* [201] studied the pyrolysis of anisole

and in a flow reactor and reported the formation of benzofuran and dibenzofuran around 1000 K. Wagnon *et al.* [179] studied anisole oxidation in a jet-stirred reactor and measured the formation of benzofuran. Similarly, Pousse *et al.* [128] reported on the formation of benzofuran in an indane/methane/oxygen/argon premixed flame. In addition, the formation and emission of large furan-embedded PACs start to get attentions. Johansson *et al.* [82] proposed a pathway for the formation of benzofuran, from the unimolecular ring closure of phenoxyvinyl radical. Later studies [43, 182], by implementing this pathway, confirmed that the formation of furan-embedded PACs could be important in flames. In light of these recent experiments, simulations, and a lack of a broader study on the formation of large PACs containing furan group, the chemical pathways to benzofuran and dibenzofuran from benzene or biphenyl were extensively studied in an environment characterized by various gas-phase species (*e.g.*, O, H, OH, C₂H₂) that are likely present in flame conditions.

4.1.1 Formation of Benzofuran from Benzene

The following chemical pathways leading to the formation of benzofuran from benzene were proposed, as shown in Figure 4.1. These pathways provide a more complete picture and would promote the formation of furan-embedded PACs even more.

The details of the quantum chemistry calculation can be found in ref. [152]. Here I briefly discuss the reaction pathways. Two likely reactions to initiate part **A** were proposed: oxygen atom (triplet) addition (**A1** + O(³P) → **A3** + H) and hydroxyl radical addition (**A1** + OH → **A9**). Acetylene addition to **A3** (**A3** + C₂H₂ → **A4**), followed by Ring Closure (RC) (**A4** → **A5**) and Hydrogen Elimination (HE) by DHE, **A5** → **A6** + H, or by HD reaction with another hydrogen atom (**A5** + H → **A6** + H₂) leads to the first pathway toward benzofuran (**A4** → **A6**) [82]. This route was previously proposed [82] and is included here for comparison purposes. Alternatively, due to the delocalized nature of phenoxy radical (**A3**), acetylene addition can occur to the benzene ring by reacting with the alternative resonance structures (see Figure 4.2) with radical site on the *ortho*-position. The second

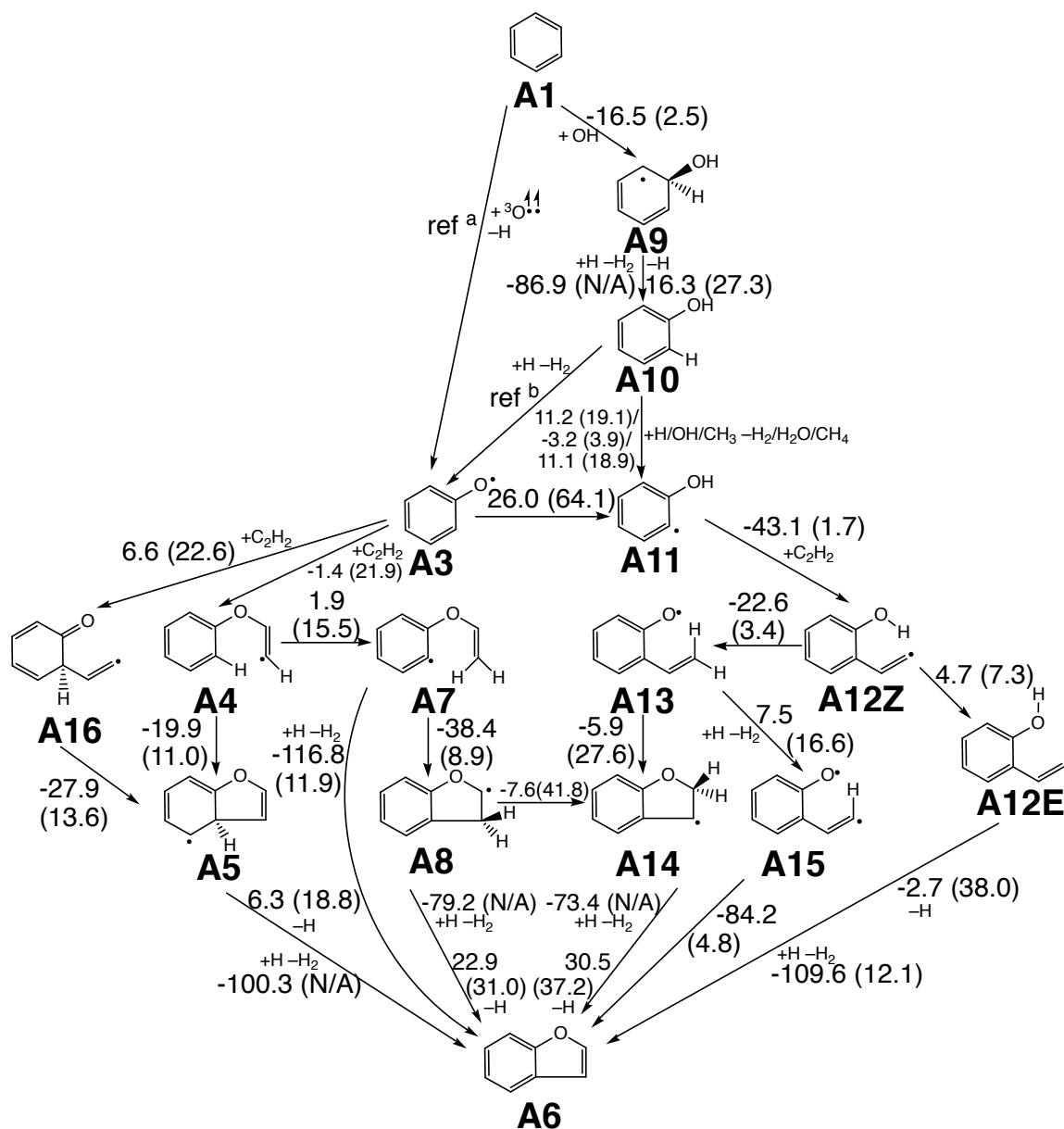


Figure 4.1: Reaction pathways for the formation of benzofuran from benzene. Heats of reaction and barrier heights (in parentheses) are placed on the reaction arrows and calculated by G3B3 compound method. Energy has the unit of kcal mol⁻¹. The pathway **A4** – **A5** – **A6** was originally proposed by Johansson *et al.* [82]. ^a Reaction **A1** + O → **A3** + H was studied by Taatjes *et al.* [161] and ^b reaction **A10** + H → **A3** + H₂ was studied by He *et al.* [75]

pathway (**A7** → **A6**) branches off from **A4**, where hydrogen migration can occur between the terminal position of vinyl group and the adjacent carbon on the aromatic ring to form **A7** (**A4** → **A7**). RC (**A7** → **A8**) is followed by HE through DHE (**A8** → **A6** + H), or HD

(**A8** + H → **A6** + H₂), leads to the formation of benzofuran, **A4** → **A6**. RC can also happen simultaneously with HE (**A7** + H → **A6** + H₂) instead of the above two-step pathway.

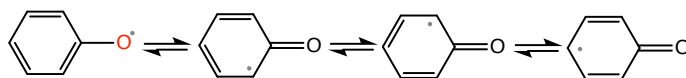


Figure 4.2: Resonance structures for **A3**, demonstrating its delocalized radical site.

For the right part of the pathways reported in Figure 4.1, starting from hydroxyl addition to benzene (**A1** + OH → **A9**), the adduct **A9** needs a HE and a hydrogen abstraction reaction before forming **A11**. The HE can happen either by DHE (**A9** → **A10** + H) or HD (**A9** + H → **A10** + H₂). Three types of H abstraction from **A10** are considered, *i.e.*, by H atom, OH radical, and CH₃ radical. The third and fourth pathways begin with acetylene addition to **A11** (**A11** + C₂H₂ → **A12Z**). The third pathway (**A12Z** → **A6**) follows the acetylene addition to **A11**. As opposed to the previous pathways, RC at this stage can happen only if HE happens at the same time since the direct RC intermediate would be a structure with formal charges on oxygen and the adjacent carbon. Similar to the second pathway, the fourth pathway (**A13** → **A6**) begins with a hydrogen migration from the hydroxyl group to the vinyl group of **A12Z**, forming **A13**. If RC happens first (**A13** → **A14**), a HE is followed through either DHE (**A14** → **A6** + H) or HD (**A14** + H → **A6** + H₂). If it is the other way around, *i.e.*, hydrogen abstraction first (**A13** + H → **A15** + H₂), a RC (**A15** → **A6**) is followed. It is worth nothing that this pathway forms a biradical intermediate, **A15**, while the ensuing ring closure reaction is an intramolecular radical-radical combination reaction. The possibility of inter-conversion between **A8** and **A14** via hydrogen migration is considered as well.

In summary, four new pathways were proposed from benzene to benzofuran, and can be grouped into two main branches, one through **A3** and the other through **A11**.

4.1.2 Formation of Dibenzofuran from Biphenyl

Dibenzofuran can be formed directly from benzofuran by forming a six-membered ring on the side of the benzofuran via HACA pathways. The details of these pathways are discussed in ref. [152]. Under certain conditions (*e.g.*, benzene flames), biphenyl peaks very early in the flame while acetylene is still accumulating [168]. Pathway **B** was based on the idea of forming dibenzofuran without acetylene involved. Starting with biphenyl, dibenzofuran can be formed through the addition of O or OH on the *ortho*-site and then close the five-membered furan ring. Figure 4.3 shows the details of this pathways.

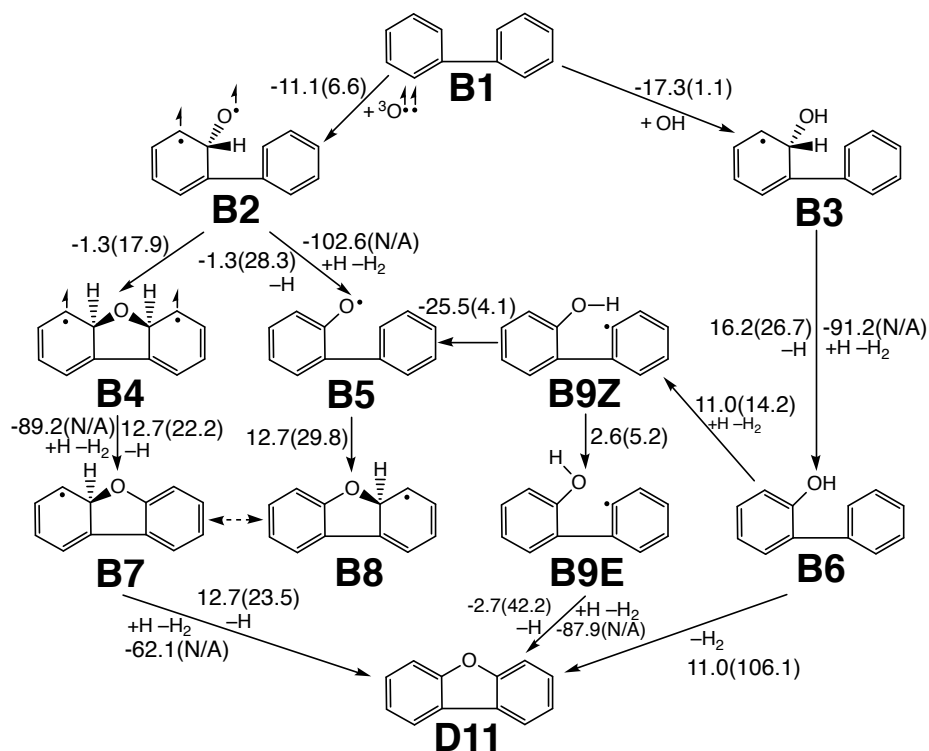


Figure 4.3: Reaction pathways for the formation of dibenzofuran from biphenyl. Heats of reaction and barrier heights (in parentheses) are placed on the reaction arrows and calculated by G3(MP2)B3 compound method. Energy has the unit of kcal mol⁻¹.

To produce dibenzofuran (**D11**) from biphenyl (**B1**), two overall reactions were proposed: $B1 + O(^3P) \rightarrow D11 + H_2$, and $B1 + OH \rightarrow D11 + H + H_2$. The first route is initiated by a triplet oxygen atom addition reaction ($B1 + O(^3P) \rightarrow B2$) to biphenyl (**B1**). There are two choices to go forth following the oxygen adduct, **B2**. One is a RC-HE-HE pathway:

a RC reaction can occur immediately, followed by two separate HE reactions. Note that H₂ elimination is not feasible since the adduct has a triplet multiplicity while the product, *i.e.*, **D11** and H₂ are both singlet. The other is a HE-RC-HE pathway, a HE can occur first, followed by a RC then another separate HE. And as before, HE can happen through either DHE or HD. For RC-HE-HE pathway, the first HE by DHE reaction is **B4** → **B7** + H, while by HD it is **B4** + H → **B7** + H₂. And the second HE by DHE is **B7** → **D11** + H, and by HD it is **B7** + H → **D11** + H₂. For HE-RC-HE pathway, the first HE can happen either by DHE (**B2** → **B5** + H), or through HD (**B2** + H → **B5** + H₂). Then follows the RC reaction (**B5** → **B8**). It should to be noted that **B7** and **B8** are mirror images of each other, and hence chemically identical. Therefore, the second HE reaction for HE-RC-HE pathway is the same as the second HE reaction for RC-HE-HE pathway.

For the overall reaction of **B1** + OH → **D11** + H + H₂, the initial addition reaction is **B1** + OH → **B3**. An HE follows the addition reaction, either by DHE (**B3** → **B6** + H), or by HD (**B3** + H → **B6** + H₂). A concerted RC with H₂ elimination reaction (**B6** → **D11** + H₂) can occur in theory following **B6** as well. Alternatively, a hydrogen abstraction reaction (**B6** + H → **B9Z** + H₂) can occur instead. Before the RC can occur, a rotation of the hydroxyl group (**B9Z** → **B9E**) is needed to expose the back side of the oxygen atom. On the other hand, **B9Z** could undergo a hydrogen migration reaction from hydroxyl group to the radical site (**B9Z** → **B5**), and connecting to the aforementioned HE-RC-HE mechanism. After the rotation of hydroxyl group that forms **B9E**, RC occurs simultaneously with HE either directly (**B9E** → **D11** + H), or through HD (**B9E** + H → **D11** + H₂).

4.1.3 Alternative and Competing Pathways Study

The reaction pathways from benzene (**A1**) or phenyl radical to phenoxy radical (**A3**) or phenol (**A10**) can happen with multiple gas-phase species and have long been studied. Benzene + O(³P) reaction was early studied by Leidreiter and Wagner [97], and its reaction rates have been used by multiple combustion mechanisms ever since. A more recent

study by Taatjes *et al.* [161] investigated the products of the benzene + O(³P) reaction experimentally and computationally. The channel leading to the production of phenoxy + H has the reaction rates of $2.0 \times 10^7 T^{1.8} e^{-2000/T}$, which is $6.4 \times 10^{12} \text{ cm}^3 \text{ mol}^{-1} \text{ s}^{-1}$ at 2000 K. The channel leading to the production of phenol has the reaction rates of $7.2 \times 10^{22} T^{-2.56} e^{-7546/T} + 1.5 \times 10^{21} T^{-2.60} e^{-3364/T}$, which is $6.6 \times 10^{12} \text{ cm}^3 \text{ mol}^{-1} \text{ s}^{-1}$ at 2000 K. Both channels show relatively similar importance at high temperatures, and the formation of phenol is the major channel for temperatures lower than 900 K. Kislov *et al.* [89] studied the rate coefficients and product branching ratios for the oxidation of phenyl and naphthyl radicals with oxygen (O₂). From the branching ratios of phenyl + O₂ reaction, formation of C₆H₅O + O route takes over 80% above 1500 K, making phenoxy radical the major product of this reaction. The phenyl + O₂ reaction rate forming C₆H₅O + O at 2000 K and 10 atm is $1.45 \times 10^{13} \text{ cm}^3 \text{ mol}^{-1} \text{ s}^{-1}$. Comparing with both channels of the reaction **A1** + O(³P), the phenyl + O₂ reaction is an important alternative pathway forming **A3**. Altarawneh *et al.* [6] studied the low-temperature oxidation of benzene with HO₂. For the multi-channel reaction phenyl + HO₂, the channel leading to the production of phenoxy + OH has the reaction rate of $1.4 \times 10^{11} T^{3.55} e^{-9000/T}$, while the channel leading to the production of phenol + O has the reaction rate of $1.8 \times 10^0 T^{3.71} e^{-9900/T}$. Two channels are highly temperature-dependent and have the rate constants of $8.1 \times 10^{10} \text{ cm}^3 \text{ mol}^{-1} \text{ s}^{-1}$ and $2.3 \times 10^{10} \text{ cm}^3 \text{ mol}^{-1} \text{ s}^{-1}$ respectively at 2000 K. Depending on the concentration of the gas-phase species, the reaction with HO₂ may also be a source for phenoxy radical (**A3**) and phenol (**A10**).

The pathway **A4** – **A5** – **A6** was originally proposed by Johansson *et al.* [82] when formation and emission of large furans start to get attentions. Later studies [43, 182], by implementing this pathway, confirmed that the formation of furan-embedded PACs could compete with HACA mechanism where both O and C₂H₂ concentrations are high. The pathways in part **A** of this article provide a more complete picture and would promote furan-embedded PACs formation even more. Johansson *et al.* calculated the potential

energy diagram by CBS-QB3 compound method. Their results are similar to ours (within 1 kcal mol⁻¹ difference), which were calculated by G3B3 compound method. We also added the hydrogen disproportionation reaction from **A5** to **A6**.

For the hydrogen abstraction from phenol, a lot of works have been focusing on the hydroxyl H (**A10** to **A3**). He *et al.* [75] studied the kinetics of hydrogen atom attaching on phenol at high temperatures. The reaction rates for phenol + H to produce phenoxy radical + H₂ is $1.15 \times 10^{14} e^{-6240/T}$, which is 5.1×10^{12} cm³ mol⁻¹ s⁻¹ at 2000 K. Altarawneh *et al.* [7] gave the reaction rates for hydrogen abstraction from hydroxyl H of the phenol (forming phenoxy radical) by HO₂ to be $7.6 \times 10^{11} e^{-6300/T}$. Abstractions by other gas-phase species such as O, OH, and O₂ can be found in these works [47, 150, 8]. For hydrogen abstraction from *ortho*-site H of phenol (**A10** to **A11**), we considered common gas-phase species H, OH, and CH₃. Comparing the hydrogen abstraction by H, abstracting from hydroxyl H has a rate of 5.1×10^{12} cm³ mol⁻¹ s⁻¹ at 2000 K, while our results for abstracting from *ortho*-site H has a rate of 1.1×10^{12} cm³ mol⁻¹ s⁻¹ at 2000 K. The difference is larger at lower temperatures, meaning that the hydrogen abstraction from hydroxyl H would dominate over the hydrogen abstraction from *ortho*-site H. Nevertheless, the hydrogen migration between **A3** and **A11** does give another route to **A11** once phenoxy radical is formed by the major-route hydrogen abstraction (from hydroxyl H).

Dames and Wang [32] studied the isomerization of benzylic and methylphenyl type radicals in single-ring aromatics, similar to our reaction **A3** to **A11**. The high-pressure limit reaction rates for the isomerization from 2-methylphenyl radical to benzyl is $3.34 \times 10^{13} e^{-23112/T}$, which is 3.2×10^8 s⁻¹ at 2000 K. The reaction rate for **A11** to **A3** at 2000 K is 6.8×10^8 s⁻¹. Both reactions show close rates because of similarity.

The competition between hydrogen disproportionation and hydrogen addition is worth to take a look. For example for the reaction **A7** + H, the hydrogen disproportionation would directly result the formation of benzofuran (**A6**) + H₂, while the hydrogen atom addition can also form a stable molecule, phenoxyvinyl, without the radical site. Hydrogen atom

addition to an aromatic carbon is a fast radical-radical combination reaction, which rate constant was estimated to be $2.0 \times 10^{13} \text{ cm}^3 \text{ mol}^{-1} \text{ s}^{-1}$ by Frenklach *et al.* [55]. While the reaction **A7** + H forming **A6** + H₂ has a rate constant of $6.7 \times 10^{11} \text{ cm}^3 \text{ mol}^{-1} \text{ s}^{-1}$ at 2000 K. Similar analysis goes for the reaction **A13** + H. The direct hydrogen atom addition to the phenoxy site has a reaction rate of $4.34 \times 10^{14} e^{-984/T}$ from literature [55], which is $2.65 \times 10^{14} \text{ cm}^3 \text{ mol}^{-1} \text{ s}^{-1}$ at 2000 K. While **A13** + H forming **A15** + H₂ has a rate constant of $2.6 \times 10^{12} \text{ cm}^3 \text{ mol}^{-1} \text{ s}^{-1}$ at 2000 K. With two magnitudes difference, the hydrogen atom addition would make the contribution of the hydrogen disproportionation smaller in a larger reaction network.

The hydrogen abstraction on the *ortho*-site aromatic carbon with the presence of different functional groups can be compared across literature to study the site effect, now with the pathway **A10** to **A11** adding phenol (hydroxyl group) into the picture. Kislov *et al.* [90] studied hydrogen abstraction from benzene (no functional group), phenylethene (vinyl group), and phenylacetylene (ethynyl group), and the reaction rate constants are $3.88 \times 10^8 T^{1.86} e^{-8039/T}$, $5.23 \times 10^5 T^{2.36} e^{-8513/T}$, and $1.29 \times 10^8 T^{1.89} e^{-8847/T}$ respectively when abstracted by hydrogen atoms. As shown in Figure 4.4 top panel, the rate constants of hydrogen abstraction from benzene by atomic hydrogen is the highest, while the rate constants for phenol is between that of phenylacetylene and phenylethene. Since the latter reactions are the first step of Frenklach and alternative Frenklach's routes of the HACA mechanism for activating aromatic sites, this result indeed shows that the benzofuran formation route initiated by **A11** is able to compete with HACA mechanism at the activation step when hydroxyl group presents.

The previous discussion is also applied to the reaction **A11** + C₂H₂ to **A12Z**. The acetylene additions to phenyl, 2-phenylethene, 2-phenylacetylene [90], and 2-hydroxybenzene radicals are compared for studying the site effect of different functional groups on *ortho*-site. As shown in Figure 4.4 bottom panel, the rate constants of acetylene addition on phenyl is the highest, while the rate constants for 2-hydroxybenzene is between that of 2-

phenylacetylene and 2-phenylethene below approximately 800 K. Since the latter reactions are the second step of Frenklach and alternative Frenklach’s routes of the HACA mechanism for attaching the second acetylene to the aromatic sites, this result again shows that the benzofuran formation route followed by **A11** – **A12Z** is able to compete with HACA mechanism at the acetylene addition step when hydroxyl group presents.

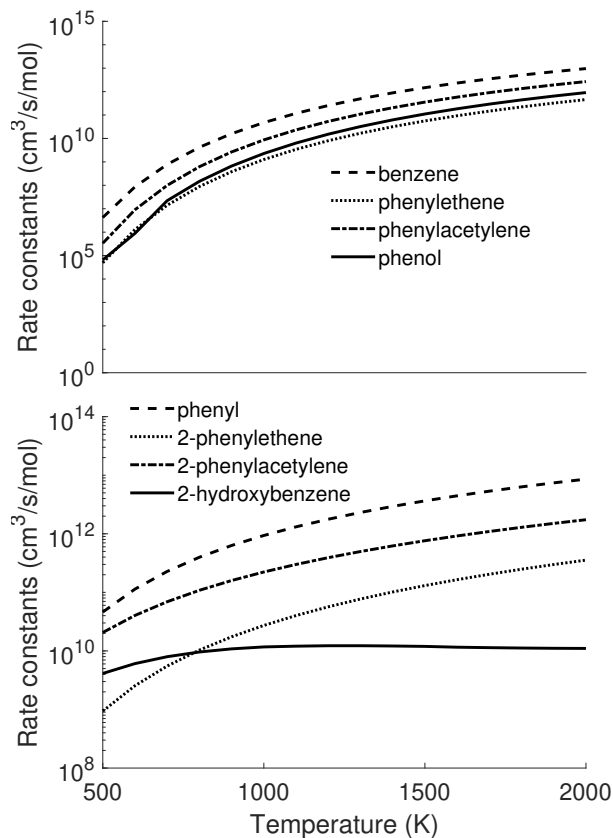


Figure 4.4: Reaction comparisons for hydrogen abstraction and acetylene addition with the presence of different functional groups

In addition, the reaction rate constants for acetylene addition to ethenylphenyl radical ($p\text{-C}_8\text{H}_7$) or to phenoxy radical (**A3** to **A4**) would also affect the relative importance of pathway **A3** to **A6** compared with the Bittner-Howard’s route [13] of the HACA mechanism. The rate constants for the C_2H_2 addition to $p\text{-C}_8\text{H}_7$ is $7.47 \times 10^5 T^{1.98} e^{-2549/T}$, which is $7.53 \times 10^{11} \text{ cm}^3 \text{ mol}^{-1} \text{ s}^{-1}$ at 2000 K [90]. While the results for the C_2H_2 addition to $\text{C}_6\text{H}_5\text{O}$ is $3.9 \times 10^{10} \text{ cm}^3 \text{ mol}^{-1} \text{ s}^{-1}$ at 2000 K. With one magnitude difference, it shows that C_2H_2 has a greater tendency to add to ethenylphenyl radical rather than phenoxy radi-

cal. Nevertheless, both Bittner-Howard's route and pathway **A3** – **A4** – **A5** – **A6** correspond to minor pathway of HACA mechanism [54] and benzofuran formation from the branching ratio study [152].

Overall, the results show that acetylene has a great tendency to add to the *ortho*-site of phenol at high temperatures, which could further lead to the ring closure and the formation of benzofuran. Once oxygen is attached to the edge of the aromatic ring, furan formation pathways are able to compete with the major routes of the HACA mechanism to form furan-embedded molecules when acetylene abundance is high too. More details of this study and additional pathways for forming dibenzofuran can be found in [152]. The reaction pathways in Figure 4.1 for the formation of benzofuran were included in the SNapS2 kinetic mechanism for the generic reactions from CO_f151 to CO_f158 in Table 3.10, while the reaction pathways in Figure 4.3 for the formation of dibenzofuran were included as CO_f159 to CO_f15d.

4.2 The Formation of Five-membered Rings

The presence of five-membered aromatic rings in PAHs and soot precursors has been reported in many studies [42, 176, 56, 192, 193, 165, 163, 45, 96, 82, 200, 16, 147]. One noteworthy example is the identification of methylene-bridged PAHs in catechol pyrolysis by Thomas *et al.* [163]. As suggested by this work, a five-membered ring could form from incorporating a C₁ unit onto an existing PAH skeleton. A detailed reaction mechanism study would help shed light on such possibility. More recent experimental studies, using AFM [147, 28] have reported on the molecular constituents of soot nanoparticles, showing a large complexity of structures, including peripheral five-membered rings of four types, namely acenaphthylene-type, acenaphthene-type, fluorene-type, and indane-type. The formation pathways of five-membered rings have long been studied as well. For example, the formation of acenaphthylene-type rings can occur via the HACA mechanism. Indane-type

five-membered rings have been studied by different groups. Mebel *et al.* [101, 117] studied the formation of indene through phenyl radical + $\mathcal{P}C_3H_4$ or $\mathcal{A}C_3H_4$, benzyl radical + C_2H_2 , as well as phenylacetylene + methyl radical. Kislov *et al.* [91] reported on the formation of indene by benzene and phenyl radical via *ab initio* methods. Pousse *et al.* [129] proposed the combustion mechanism of indane, including the conversion between indene and indane through multiple gas-phase species. Similarly to indene formation, benzoindene can be formed from naphthalene as demonstrated in a recent publication [206].

Within the scope of expanding the understanding for the formation of five-membered rings, I proposed the following reaction pathways for the formation of five-membered rings onto existing PAH framework. In particular, from a "zig-zag" (C_3 motif) site and a C_2 gas phase species to yield acenaphthylene/acenaphthene type hydrocarbons, and from an "armchair" (C_4 motif) site and a C_1 gas phase species leading to fluorene-type compounds. The formation of five-membered ring from a "free-edge" (C_2 motif) site and a C_3 gas phase species has been reported elsewhere [129, 117, 206]. Similarly, possible pathways for the formation of pyrene by phenanthrene reacting with methyl radical have been reported already in the literature Georganta *et al.* [62].

4.2.1 Five-membered Ring Formation on Zig-Zag Site from Naphthalene

Reaction pathways to form five-membered rings on the zig-zag site begin with naphthalene are shown in Figure 4.5.

As initial step, we considered the reactions of naphthalene (**N1**) either with a radical, C_2H_5 and C_2H_3 , or by first undergoing hydrogen abstraction to form **N2**. **N2** radical can then react with non-radical C_2 species C_2H_2 , C_2H_4 , or C_2H_6 . Furthermore, we considered radical-radical combination reactions for **N2**, leading to the formation of **N5** and **N6** by reacting with C_2H_3 or C_2H_5 radicals.

The intermediates formed at this stage are naphthalene with an ethyl group (**N6**), its

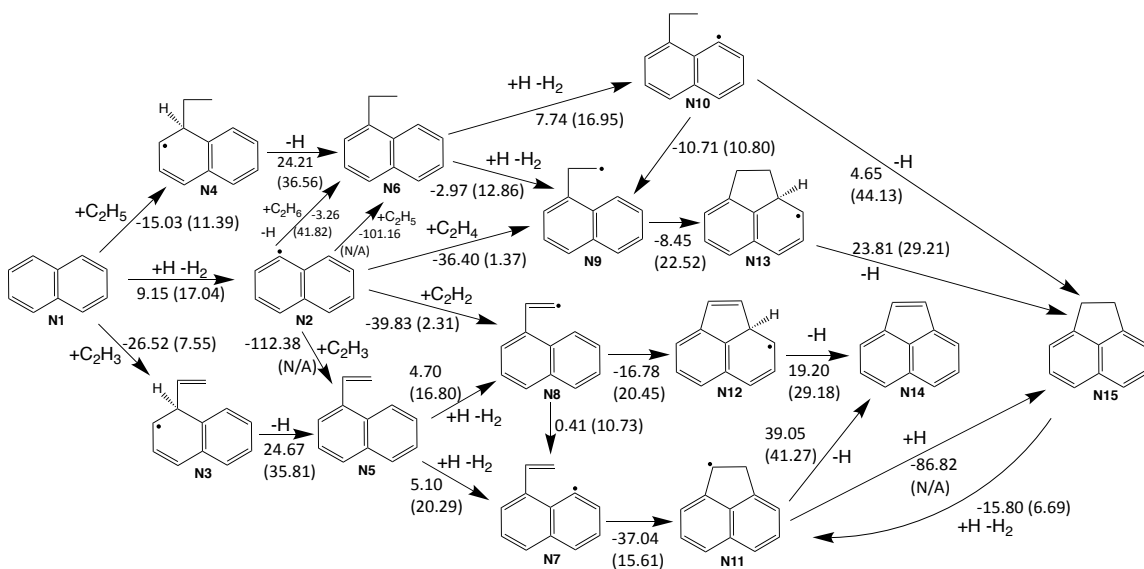


Figure 4.5: Reaction pathways for the formation of five-membered ring from a zig-zag site and a C_2 gas phase species. Heats of reaction and barrier heights (in parentheses) are placed on the reaction arrows and calculated by G3B3 compound method. Energy has the unit of kcal mol^{-1} .

radical on terminal site (**N9**), naphthalene with a vinyl group (**N5**) and its radical on terminal site (**N8**). The alternative to radical on terminal site, is radical on the naphthalene ring, **N10** and **N7** for ethyl and vinyl group, respectively. Inter-conversion between these two types of radicals, **N8** \rightarrow **N7** and **N10** \rightarrow **N9**, were also considered. The saturated five-membered ring **N15** can be directly formed from the intermediate **N10**. **N15** can also be formed through a two-step mechanism, RC then HE, from the other radical **N9**.

The unsaturated five-membered ring **N14** can be directly formed from the intermediate **N7** with radical on the ring via a two-step RC-HE pathway. The pathway to form **N14** from the other radical **N8** via two-step RC-HE is the ring closure step of the classical HACA pathway. An alternative pathway to form a saturated five-membered ring, **N15** goes through the formation of **N11** first, then undergoing a radical-radical combination reaction with hydrogen atom. The conversion from unsaturated five-membered ring **N14** to saturated five-membered ring **N15** can be achieved via two successive hydrogen addition reactions, **N14** + H \rightarrow **N11** and **N11** + H \rightarrow **N15**. The conversion from **N15** to **N14**, on the other hand, could most likely occur via a hydrogen abstraction reaction first, followed by a

hydrogen elimination reaction: $\text{N15} + \text{H} \rightarrow \text{N11} + \text{H}_2$ and $\text{N11} \rightarrow \text{N14} + \text{H}$.

4.2.2 Five-membered Ring Formation on Armchair Site from Biphenyl

Formation of five-membered ring starting from an armchair site on biphenyl or phenanthrene schematically mirror each other identically. Therefore here I only discuss the pathways from biphenyl, as shown in Figure 4.6. More information on the formation pathways from phenanthrene can be found in ref. [153].

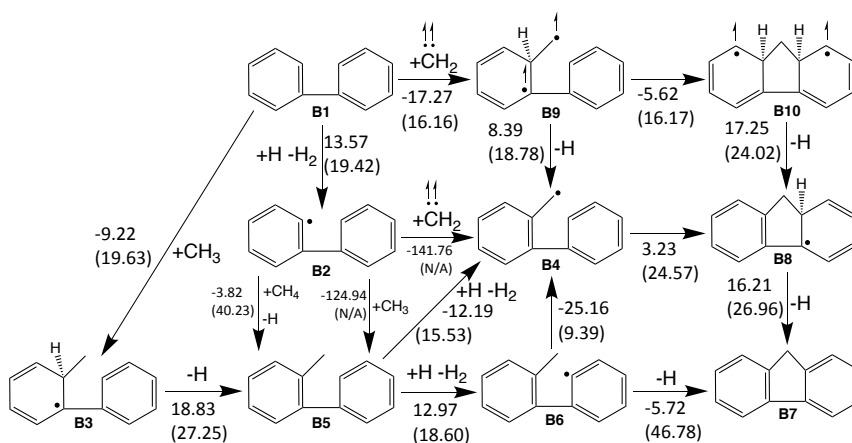


Figure 4.6: Reaction pathways for the formation of five-membered ring from an armchair site and a C_1 gas phase species. Heats of reaction and barrier heights (in parentheses) are placed on the reaction arrows and calculated by G3B3 compound method. Energy has the unit of kcal mol^{-1} .

Similar to the previous part, the initial reaction of biphenyl **B1** can occur by reacting with either radicals, CH_3 or triplet-carbene (CH_2), or by first undergoing hydrogen abstraction and produce **B2**. We elected to not consider singlet-carbene addition since such reaction usually result in three-membered ring and is likely irrelevant to five-membered ring formation. The two pathways, addition of CH_3 radical and hydrogen abstraction, converge into forming **B5** after one more reaction respectively. The second reaction for addition of CH_3 is a HE, while for the hydrogen abstraction, the follow-up reaction is a substitution reaction with CH_4 .

In order to facilitate RC, a hydrogen abstraction is needed first from this point onward.

This can occur at the terminal site of the newly added methyl group (forming **B4**), or at the other ring adjacent (forming **B6**). The two newly formed radicals (**B4** and **B6**) can convert into each other via hydrogen migration. Alternatively, **B2** can undergo radical-radical combination reactions with CH_3 and CH_2 to form **B5** and **B4**, respectively. RC reaction from **B6** is an one-step substitution reaction in forming **B7**, while RC from **B4** is followed by a HE reaction, $\text{B4} \rightarrow \text{B7} + \text{H}$.

Looking at the result of triplet-carbene addition **B9**, since **B9** is of triplet electronic configuration, it cannot form a singlet stable structure in one step, unless spin-crossing is considered, which is outside the scope of this study. It is possible to have a ring closure reaction directly from **B9**, resulting in forming **B10**, followed by two sequential hydrogen elimination reactions, forming **B8** and **B7**, respectively. Alternatively, a hydrogen elimination reaction can occur first to **B9** and form **B4**, and the rest has been discussed already.

4.2.3 Reaction Pathways in a Closed Homogeneous Batch Reactor

The relative importance of various kinetic pathways for the production of acenaphthylene (**N14**) and acenaphthene (**N15**) was investigated in a closed homogeneous zero-dimensional reactor. We used the CHEMKIN-Pro's 0-D Closed Homogeneous Batch Reactor [135] to study the relative importance of the proposed pathways under combustion conditions. The mole fraction of the initial gas-phase species comes from the simulations using CHEMKIN-Pro's PREMIX code to model an atmospheric-pressure laminar premixed ethylene-air flame with a cold gas velocity of 9.8 cm s^{-1} and an equivalence ratio of 2.03. The details of the flame can be found in [147, 28], including the measured temperature profile, which was provided to the CHEMKIN in order to minimize the inaccuracy of modeling heat loss. The gas-phase simulation results of this flame are discussed in [184]. The mole fractions of H, H_2 , C_2H_2 , C_2H_3 , C_2H_4 , C_2H_5 , C_2H_6 and naphthalene are 3×10^{-4} , 8×10^{-2} , 2×10^{-2} , 1×10^{-5} , 2×10^{-2} , 7×10^{-5} , 1×10^{-3} and 6×10^{-5} correspondingly. The remaining is considered to be nitrogen. The simulations are run at 1 atm and 2000 K with a residence

time of 20 ms. For the kinetic mechanism, we compiled the proposed reactions into the CHEMKIN format. As results, a total of 46 species and 57 reactions are included in the mechanism.

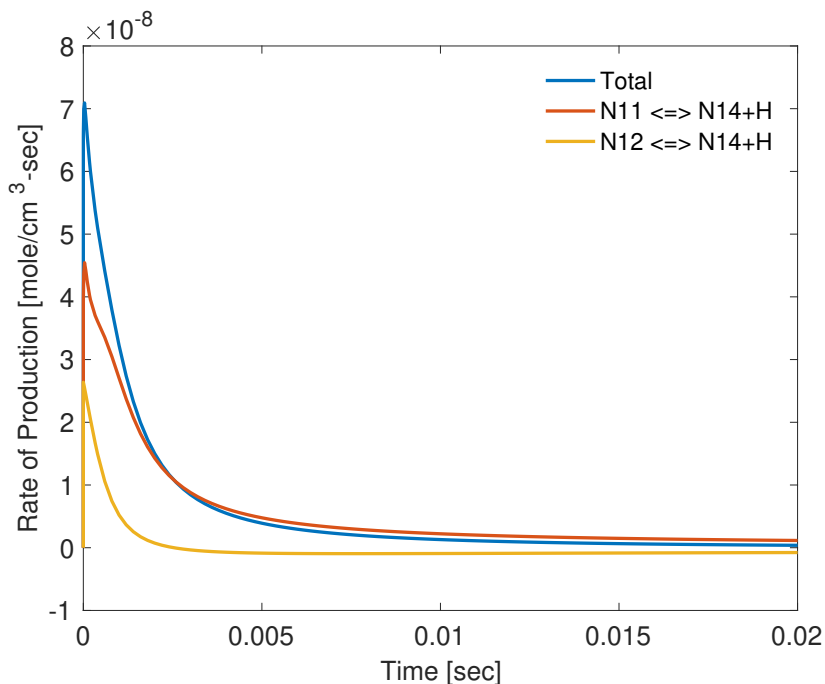


Figure 4.7: The rate of production for the formation of acenaphthylene (**N14**).

As reported in Figure 4.7, both pathways from **N11** and **N12** are important for the formation of acenaphthylene, and pathways from **N11** have a higher rate of production compared with the others. The results highlight the importance of the HACA as major pathways for the formation of acenaphthylene. Acenaphthene (**N15**) starts to convert to **N11** after 1 ms, as shown in Figure 4.8.

The production of acenaphthene happens mostly via $\text{N11} + \text{H} \rightarrow \text{acenaphthene}$, while the consumption is due to $\text{acenaphthene} + \text{H} \rightarrow \text{N11} + \text{H}_2$. From Figure 4.8, the net production rate of acenaphthene becomes negative after 1 ms. There exists an equilibrium between acenaphthylene and acenaphthene under this condition. The formation of acenaphthene is an important path for acenaphthylene, and similarly, **N13** is a significant exit for acenaphthene. Thus it is important to include the new proposed reactions to improve the predictions

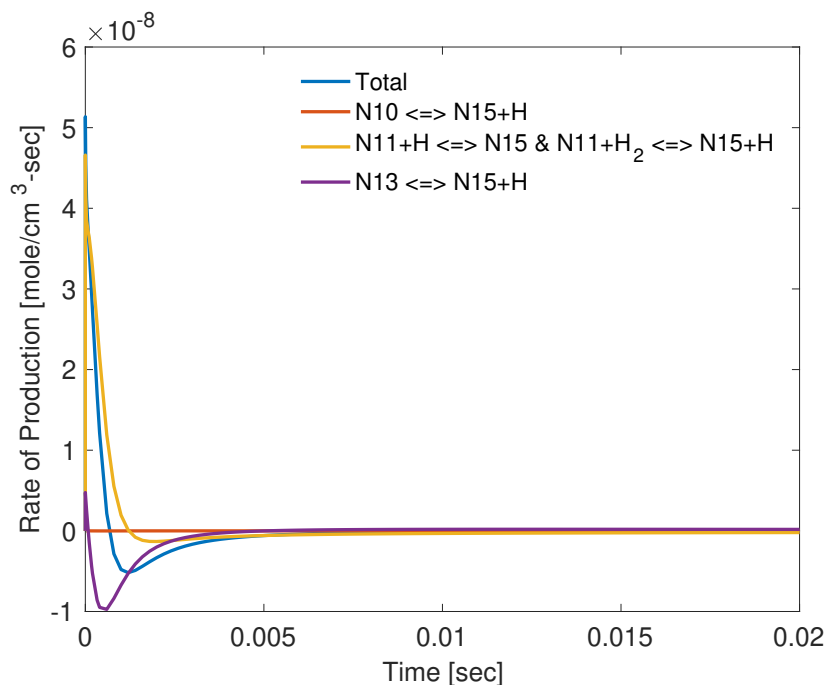


Figure 4.8: The rate of production for the formation of acenaphthene (**N15**).

of kinetic mechanisms for acenaphthylene and acenaphthene.

The 0-D Closed Homogeneous Batch Reactor is also used to study Part **B** for the formation of **B7** (fluorene). The main pathways for Part **B** are **B1** → **B3** → **B5** → **B4** → **B8** → **B7**. PAHs with radical sites could cross-link and make biphenyl-type armchair site more accessible for pathways in Part **B**.

The new reaction pathways provide a more complete description for the formation of PAHs containing five-membered rings, more importantly, the embedded five-membered rings such as methylene-bridged PAHs identified in catechol pyrolysis, that can play an important role not only in the gas-phase chemistry of aromatics but also as pathways to five-membered rings on armchair sites and cross-linking for soot models.

CHAPTER 5

Validations of the S_{NapS2} in Various Combustion Conditions

The characteristics of the PACs predicted with the kinetic mechanism were compared against different experimental measurements: mass spectra measured in a counterflow diffusion flame [182], the oxygen-to-carbon ratios obtained at different locations of a coflow diffusion flame [144], and the molecular structures observed in a premixed laminar flame [184]. These successful validations demonstrate that the S_{NapS2} kinetic mechanism provides a high-fidelity, and yet generic, description of the PAC formation under various combustion conditions, making S_{NapS2} the first-of-its-kind to have such extensive flexibility and wealth of information. It greatly contributes to reveal the underlying chemical pathways to the experimental observations. The following sections are adapted from these publications [182, 144, 184].

5.1 Mass Spectrum in an Ethylene Counterflow Diffusion Flame

The experiments were carried out at Sandia National Laboratories by Dr. K. Olof Johansson, Mr. Paul E. Schrader, and Prof. Hope A. Michelsen, while the CFD simulations were conducted by Prof. Doohyun Kim at Hongik University. Thus in this dissertation, I only

briefly introduce these results as part of the flame system for clarity, and focus mainly on the stochastic modeling results. The following section is adapted from this publication [182].

5.1.1 The Flame System

The details of the experimental setup can be found in [182]. The flame is an atmospheric-pressure ethylene/oxygen/argon counterflow diffusion flame. Fuel side delivered a mixture of 0.23 slm (standard liters per minute at 0 °C and 101.325 kPa) ethylene and 1.10 slm argon; the oxidizer side supplied a mixture of 0.25 slm oxygen and 1.20 slm argon. The gas-phase composition along the centerline of the flame was determined using flame-sampling Molecular-Beam Mass Spectrometry with Vacuum-Ultraviolet Photoionization (VUV-MBMS). The species measured using VUV-MBMS had masses less than ~ 200 u. The Aerosol Mass Spectrometry with Vacuum-Ultraviolet Photoionization (VUV-AMS) was employed to extend the mass range of measured species to ~ 550 u.

The details of the CFD simulation can be found in [182] as well. The CFD results were validated against the experimentally measured temperature and species profiles and showed very good agreements. Figure 5.1 shows the temperature contours at steady state on the central plane of the counterflow flame from CFD results. The flame, located on the oxidizer side, is stabilized by the fuel diffusion across the stagnation plane and has a maximum temperature of 1970 K at a Distance From the Fuel Outlet (DFFO) of 6.1 mm.

5.1.2 Stochastic Modeling

The growth of soot precursors was modeled using SNapS2. As input to the SNapS2 simulations, I used the gas-phase composition and temperature data obtained from the CFD simulations, interpolating between mesh points. The flow streamlines of the counterflow flame were obtained using MATLAB by solving the equations of motion given each position and gas-phase velocity. Cyclopentadiene, benzene, and toluene were chosen as seeds for this study from the criteria discussed in methodology. To obtain enough statistical data

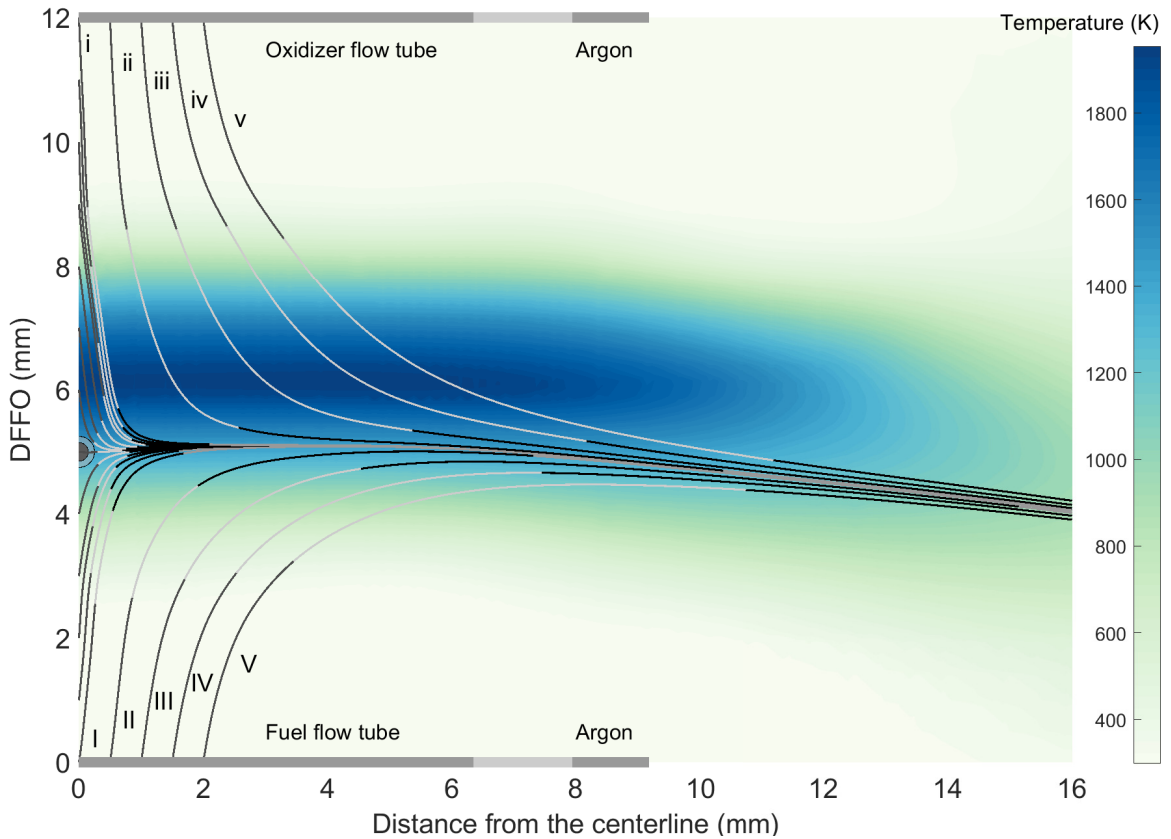


Figure 5.1: Snapshot of the central plane of the counterflow flame obtained via CFD simulations. Background color indicates temperature, and lines represent flow streamlines, labeled by Roman numerals (both lowercase and uppercase). Colored segments on each streamline separate different transit time (0.02 s, 0.04 s, and 0.06 s) along the line. At a DFFO of 5.0 mm, the black semicircle shows the experimental probe size, and the shadowed semicircle around it represents the computational probe sampling area used by SNapS2. Dark gray bars at DFFOs of 0 mm and 12 mm display the radius of the center and outer flow tubes, separated by tube thickness in light gray.

for the stochastic model, around 300 simulations at each starting points were simulated. A total of 110 starting points along the centerline and the selected flow streamlines were used, generally separated by 1 ms on each streamline, for a total of 32,000 SNapS2 traces. The contribution of each seeds to the whole mass spectrum was then weighed by its concentration at the starting point.

As the first validation of SNapS2, I compared the mass spectra generated by SNapS2 with data obtained from the VUV-AMS measurements. First, I estimated the region sampled by the experimental probe to define the sampling region for the SNapS2 simulations.

The experimental setup provides sub-mm vertical resolution because the probe tip opening diameter was 0.3 mm. Nevertheless, the probe likely extracted sample from a volume corresponding to a vertical region that is somewhat larger than the probe-tip opening. Therefore, we assumed that the probed region was a semicircle with a diameter of 0.5 mm (shown in Figure 5.1). Second, I chose to analyze the mass spectra at a DFFO of 5.0 mm, close to the stagnation plane where the growth of soot precursors is high. Since the VUV-AMS measurements have a 0.2 mm shift towards the oxidizer side comparing with the CFD results along the DFFO, the AMS data at a DFFO of 5.15 mm was compared with the SNapS2-generated mass spectrum at a DFFO of 5.0 mm. Figure 5.2 shows the comparison between the experimental aerosol mass spectrum and the mass spectrum predicted by SNapS2.

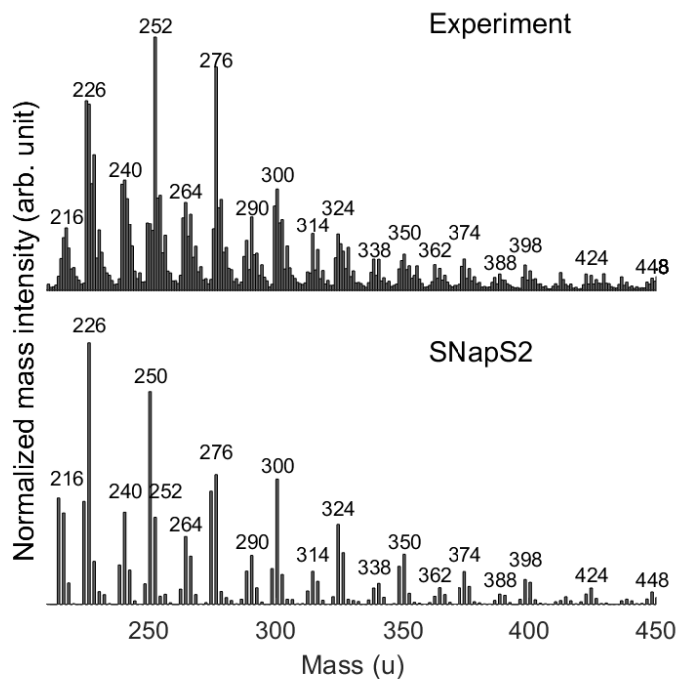


Figure 5.2: Mass spectra at a DFFO of 5.0 mm. The experimental aerosol mass spectrum shown in the top panel was obtained with an ionization photon energy of 9.5 eV at a DFFO of 5.15 mm. The mass spectrum predicted by SNapS2 at a DFFO of 5.0 mm is shown in the bottom panel.

The comparison between the experimental and simulated mass spectra demonstrates excellent agreement, indicating that SNapS2 produces a high fidelity model of the soot

precursors formation in the counterflow flame: all major peaks in the range 200 u to 450 u are reproduced, and the relative intensity (both within peak clusters and between clusters over extended mass ranges) are well captured.

For the experimental results, transport efficiencies in the sampling line and aerosol mass spectrometer lead to reduced peak intensities on the low-mass side of the mass spectrum [84], and may explain why the experimental mass peaks at 216 u and 226 u, for example, have lower intensities relative to higher masses than predicted by the simulations. In addition, the SNapS2 simulations predict a rapid and monotonic decrease in mass-peak intensity with species size for both the even and the odd-carbon-numbered peak sequences. The denser packing of mass peaks in the experimental spectrum, compared with the simulated spectrum, stems from ^{13}C intensity shifts that add significant intensity on numerous odd masses within peak clusters in the experimental spectrum.

In general, this validation on the mass spectrum shows that the SNapS2 code and kinetic mechanism are able to reassemble the pure hydrocarbon PACs in flames in terms of the mass intensity and chemical formulas. This is a big leap compared with SNapS, for which only even-numbered-carbon peaks were able to be reproduced in a benzene premixed flame. This advancement in the SNapS2 modeling results demonstrate that the SNapS2 kinetic mechanism does provide a more complete description of the PAC formation, which captures the major routes for the pure hydrocarbon growth in combustion systems.

5.2 Oxygen content in a Coflow Diffusion Jet A-1 Surrogate Flame

This work is a collaboration with Mr. Jacob C. Saldinger from the Violi Group and published in [144]. The following section is adapted from this publication.

5.2.1 The Flame System

The system consists of a coflow diffusion laminar flame with a Jet A-1 surrogate fuel (69 % *n*-decane, 11 % *n*-propylcyclohexane, and 20 % *n*-propylbenzene) [31]. The details of the CFD simulations can be found in Saffaripour *et al.* [140] while additional experimental details used in validation can be found elsewhere [88, 19].

In order to describe the environment to use in the SNapS2 simulations, we used the CFD data from a previous work [140] to build two-dimensional profiles of species mole fractions, temperatures, and velocities for the flame. Velocities were used to identify the center streamline, as shown in Figure 5.3, using the streamline function implemented in MATLAB [112]. Of note, we have defined the centerline as the streamline originating at a radius of 0.5 mm. This small discrepancy is needed to avoid discontinuities and numerical artifacts arising from the boundaries in the CFD simulations, and we tested that this choice does not affect the gas phase appreciably.

5.2.2 Stochastic Modeling

The formation of PACs was simulated by SNapS2. In these simulations, the starting seed molecule was grown until the end of the streamline was reached or the mass exceeded 600 u, to match the experimental sampling range. In order to capture early growth, we started our simulations at a Height Above the Burner (HAB) of 0 mm and at intervals of 1 ms or 5 ms depending if the concentration of the molecules used as a seed has already reached (or not) the 5 % concentration threshold. At each time interval, we ran 100 simulations of the seed molecule with the highest peak concentration (benzene in this flame) while the number of simulations for the remaining seed molecules was determined relative to each molecule's maximum concentration. Seed contributions to final properties were normalized by the number of simulations performed at each time step so that the number of simulations did not affect a molecule's relative intensity. Overall, we performed approximately 12,000 simulations along the center streamline. In these simulations, we observed

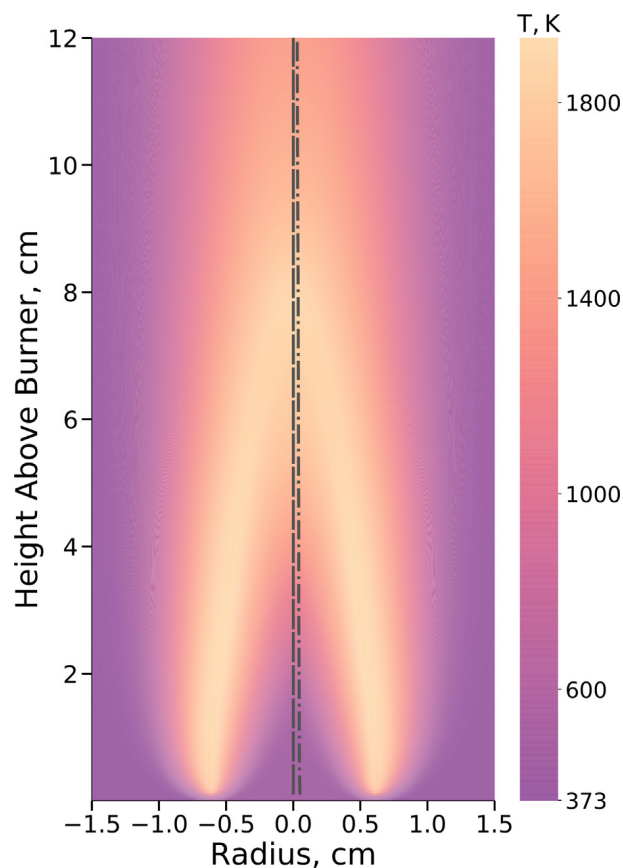


Figure 5.3: Temperature profile from CFD simulations [140]. The streamline at a radius of 0.5 mm is shown as a dash-dotted line while the true centerline is a dashed line.

approximately 2 million unique compounds and 4 million unique reactions.

The experimental electron ionization mass spectrometry used to validate our results identified a large range of oxy-PACs between 150 u and 600 u [19], indicating that the oxy-PACs are an important contributor to the diversity of PACs. Figure 5.4 shows the comparison in the Oxygen-to-Carbon Ratio (O/C) between experimental and simulated compounds along the center streamline at different HABs. To provide a clearer comparison, a small number of PACs with more than 10 oxygen atoms and a larger number PACs without oxygen were omitted from the figure. This choice reflects the experimental difficulty of detecting signals from these compounds. On one hand, highly oxygenated species, consisting of molecules with 11-13 oxygen atoms, contained a large number of hydroperoxides (and derived groups) that are difficult to detect experimentally [190, 202]. On the other hand,

apolar PACs, like most of the species with O/C of zero, cannot be measured experimentally due to the ionization spray technique used.

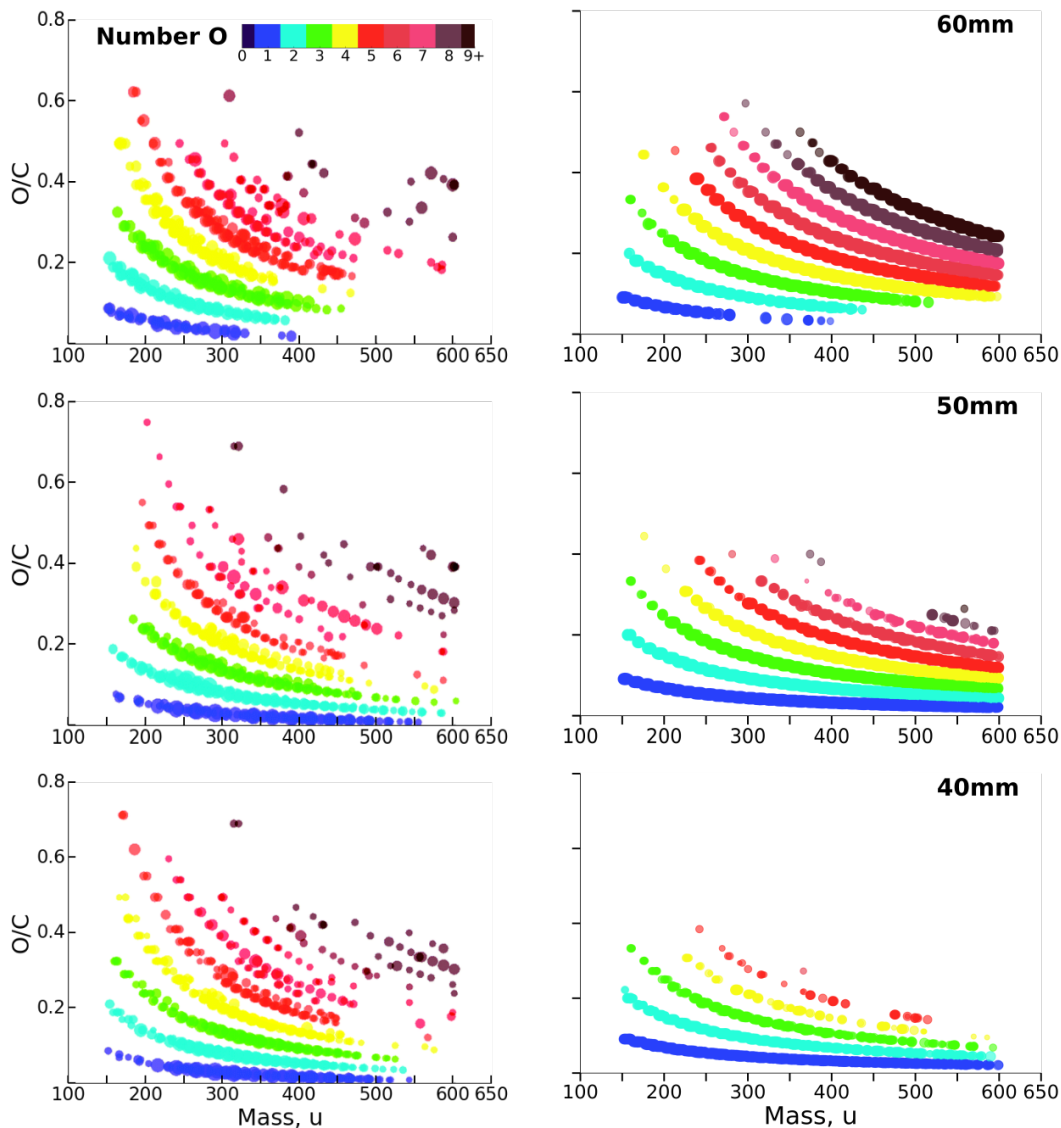


Figure 5.4: Oxygen-to-carbon ratio plotted against the molecular mass for different locations along the center streamline. The experimental results are shown on the left and the SNapS2 results on the right. The size of the circles in each plot is proportional to the logarithm of species relative concentration. Experimental results are reproduced/adapted from ref. [19] with permission from the PCCP Owner Societies.

With the exception of a few low masses, highly oxygenated species, the range of oxy-PACs in mass and number of oxygen atoms generally match between 150 u and 450 u at

HABs of 40 mm, 50 mm, and 60 mm. There are, however, some revealing discrepancies. The most noteworthy deviation is the under prediction of oxygen in our simulations at lower HABs. At an HAB of 30 mm where experiments observe a large number of diverse PACs up to 600 u, little growth is observed in the simulations. One possible reason for this discrepancy could be that there exists some low-temperature PAC oxygen chemistry [186] not captured in the kinetic mechanism. Prior to this region, the temperature along the centerline is relatively low and as such our simulations show only a few reactions mostly involving PACs with a single or no oxygen atoms. An alternate explanation is that the experimental measurements of the soot precursors do not accurately represent the true undisrupted gas-phase environment. The rapidly increased mass growth and oxygenation of up to 600 u and 6 oxygens seen at 40 mm demonstrates that the PACs' formation in this area is very spatially sensitive. Minor streamline disruptions during thermophoretic sampling [141] may be significant enough to bring about this discrepancy. Furthermore, although not as pronounced as in other flame configurations, studies of thermophoresis in coflow diffusion flames have identified complex two dimensional migration patterns which cause larger soot precursors to travel at a different rate and direction than the bulk gas-phase [86]. Thus, PACs thermally diffusing from higher HABs [73] or nearby streamlines may account for this difference. In addition, electron-spray ionization tends to produce results that are biased towards more oxygenated compounds when samples with lower O/C ratios are present [12] and as such it could be possible that these compounds are present in very small amounts but appear at high concentrations. Finally, while our results suggest the majority of these oxygenated compounds grow within the flame, it is not possible to rule out, as the authors of the experimental study acknowledge [19], that some growth may occur after experimental sampling [35].

Other deviations in our simulations are likely due to the intrinsic limitations of SNapS2. First, simulations fail to capture some low mass, highly oxygenated compounds. Unlike other differences, this issue is persistent at all heights in the flame. Such low masses and

high O/C ratios suggest these molecules are most likely small acyclic or highly saturated molecules. These molecules are likely not products of aromatic growth as the majority of species observed in experiment with an O/C ratio of greater than 0.5 have less than 15 carbons and an Hydrogen-to-Carbon Ratio (H/C) between 1 and 2.25 which falls above the PAC cata-condensed [155] limit. While SNapS2 does include the growth of aliphatic chains and non-aromatic rings in the kinetic mechanism, these low mass, non-aromatic molecules are not captured as our seed selection and mechanism emphasizes polycyclic aromatic growth. Second, for HABs of 50 mm and 60 mm, the model over-predicts high mass compounds (between 450 u and 600 u), especially with less than 5 oxygen atoms, that are not observed in experiment. This is most likely due to the removal from the gas-phase of heavier species through physical growth [2] or radical-radical combination reactions with other PACs [81]. The importance of radical-radical combinations of PACs relative to other growth mechanisms has been observed [43] to become a significant factor in predicting mass growth at higher masses although eventually this is offset by the low concentrations of these large PACs. Although the role of these reactions in this flame may differ, stochastic modeling of the counterflow flame in previous section [182] have found good agreement with experimental results up to approximately 450 u without including these radical-radical reactions. Physical growth is thought to significantly contribute to mass growth in coflow diffusion flames as masses approach 600 u [2]. This hypothesis is also sustained by the observation that this discrepancy occurs primarily for PACs with low oxygen content, which is inline with the findings by Elvati *et al.* [44, 46] suggesting that oxygen can inhibit physical dimerization.

In general, despite the complexity of the system, we were able to match the previous experimentally observed range of oxygenation and aromaticity at multiple locations along the centerline of the flame. Although we observe generally an excellent agreement, our simulations fall short in two areas: description of growth of almost purely aliphatic species and secondary growth which involves PAC-PAC interactions. This study further validated the

oxygen chemistry of the kinetic mechanism. In addition to the validation of the pure hydrocarbon growth in the counterflow flame, SNapS2 is able to predict the chemical formulas of the PACs being formed in different combustion systems.

5.3 Molecular Structures in an Ethylene Premixed Flame

The details of large PAC structures have remained largely a mystery with several proposed hypotheses and models. Recent advances in experimental techniques have allowed us to view the atomic structure of a few PACs. Namely, using AFM [147, 28], molecules from an ethylene-air laminar premixed flame were analyzed and assigned detailed molecular structures. Despite some inherent limitations of AFM, observations from these images are of immense interest in the modeling field as they provide much needed feedback to improve successful models and eliminate incorrect ones. I applied the SNapS2 to model this flame, and compared the molecular structures between SNapS2 simulations and AFM observations. The following section is adapted from this publication [184].

5.3.1 The Flame System and the Gas-phase Modeling

The flame system used in the AFM studies is a laminar atmospheric ethylene-air premixed flame with a carbon-to-oxygen atomic ratio of 0.67 (equivalence ratio 2.03) and a cold gas velocity of 9.8 cm s^{-1} . I modeled the gas-phase environment of this flame with the PREMIX code of CHEMKIN [135] and the KAUST mechanism II [185] as the kinetic mechanism. The CHEMKIN simulations used the experimental temperature profile [28] to improve the accuracy of heat modeling. The temperature profile and the mole fractions of gas-phase species with molar masses less than benzene were then used as inputs for the SNapS2.

5.3.2 Stochastic Modeling

In order to compare the effect of oxygen chemistry in this flame, I ran the SNapS2 simulations with both the full kinetic mechanism and a reduced mechanism which excludes the formation of oxy-PACs. Since the contribution to computed PAC properties is weighted by the concentration of the seed molecules, I selected benzene as the seed molecule as it has the highest mole fraction (by at least one order of magnitude) compared to other small cyclic molecules along the entire flame. I set the upper limit of the molecular mass to be 1000 u (which corresponds to the molecules with around 80 carbon atoms) since other growth mechanisms that are not yet included in SNapS2 are likely to dominate the growth above this threshold [41, 154, 45], *e.g.*, radical-radical reactions [43, 81]. I run a total of 37,000 traces and then analyzed the results at an HAB of 8 mm and 14 mm, which correspond to the nucleation and growth zone from experiments [28].

Similar to the AFM images, the SNapS2 simulations predict a large diversity of PACs in this flame. By analyzing the simulations, I observe that most of the PAC growth takes place before 8 mm, in agreement with experiments [28] identifying the nucleation zone at 8 mm (or before). For this reason, the PACs observed at 8 mm and 14 mm do not exhibit radically different structures, O/C ratios, or H/C ratios. In Figure 5.5, I show 32 examples of molecules sampled at an HAB of 8 mm. These molecules (which represent less than 0.005% of all the SNapS2-generated unique structures at this height) show the presence of oxy-PACs, condensed aromatics, curved molecules, different types of five-membered rings, PACs with only six-membered rings, as well as aliphatic structures. All the SNapS2 simulated molecules at two locations with two mechanisms have been provided in ref. [184].

5.3.2.1 Oxygenated PACs

There are only three oxygenated species identified from the AFM studies, a phenol, a ketone and a derivative of benzopyran (labeled in the original work as **PS7**, **PS2**, and **IS9** respectively). Each molecule, however, requires a different formation pathway, which in-

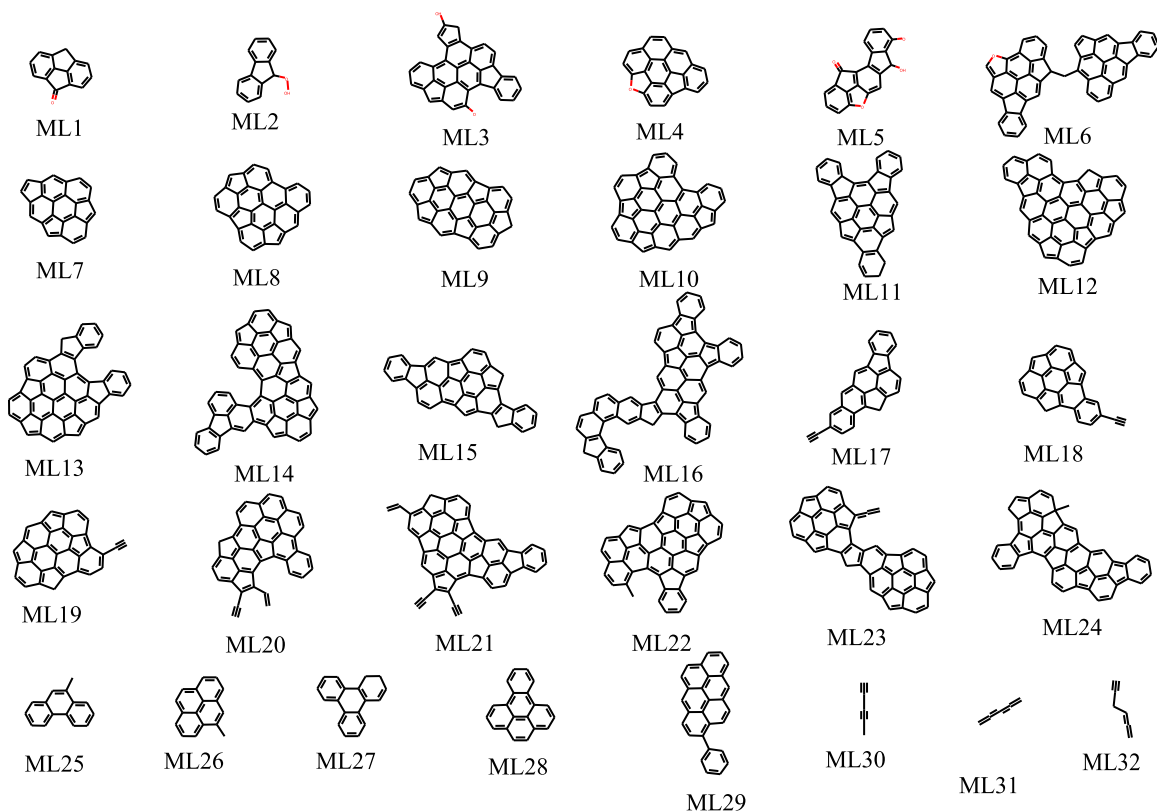


Figure 5.5: Example molecules simulated by the SNapS2 at an HAB of 8 mm of the pre-mixed flame

indicates the complexity of the oxygen reactions that occur in the flame. Due to a number of reactions including the formation of peroxols and ketones [207] and furan-embedded PACs [152], the simulations also show molecules containing phenols, peroxols, ketones, and furans (**ML1** to **ML6**) (see Figure 5.6). Among the experimentally observed oxygenated functional groups, however, the kinetic mechanism currently cannot reproduce the oxygen-embedded six-membered rings, like the one in **IS9**.

While the structures from the AFM images cannot provide definitive indication of the relative concentrations, the oxy-PACs seem to appear much less frequently than the pure hydrocarbons compared to the simulations. I hypothesize that this may be due to two factors. First, the SNapS2 mechanism may lack enough reactions for the decomposition/evolution of furan-embedded PACs, which leads to an overestimation of these types of functional groups. Second, the AFM sample may be partially biased against oxy-PACs,

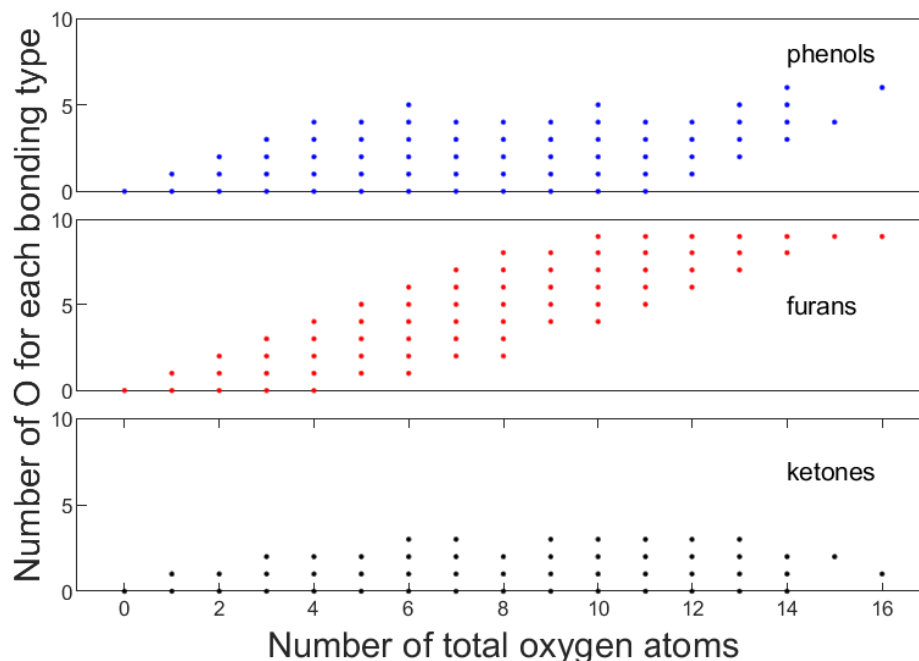


Figure 5.6: Possible number of chemical groups involving oxygen observed in simulated SNapS2-generated molecules at 8 mm. Number of phenols (blue, upper panel), furans (red, middle panel), and ketones (black, lower panel) with respect to the number of oxygen atoms.

which are more likely to form curved molecules and have generally weaker non-bonded interactions [43, 46, 45], making them harder to sample. Details about the O/C ratio of the SNapS2-generated molecules are shown in Figure 5.7.

The O/C ratio for the molecules at 8 mm and 14 mm do not show distinct distribution along different number of carbons atoms. This similarity from the SNapS2 simulation is also observed in experiments. Both Raman spectroscopy and AFM measurements indicate that the average size of the molecules at 8 mm and 14 mm are similar [28]. Therefore, even while I focus on two HABs, the results can likely be generalized to other locations in the flame.

5.3.2.2 Hydrogen-to-Carbon Ratio

The sampled structures from AFM suggest a minimal presence of oxy-PACs. However, when considering the H/C ratio at an HAB of 8 mm, inclusion of the oxygen chemistry

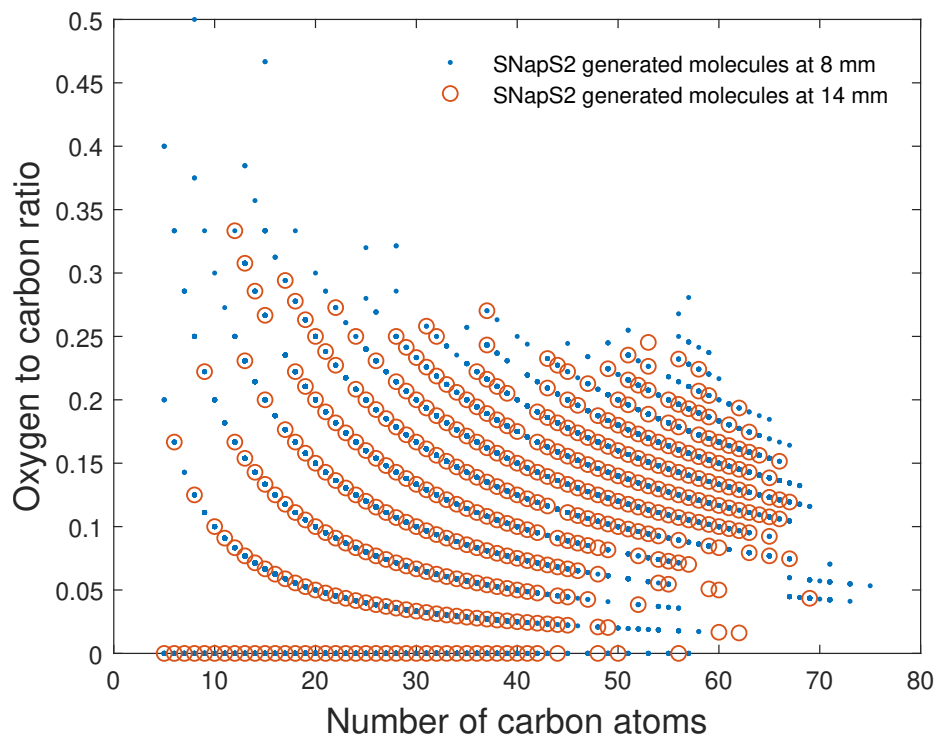


Figure 5.7: Oxygen-to-carbon ratio for SNapS2-generated molecules with respect to the number of oxygen atoms at 8 mm (blue dots) and 14 mm (red circles).

results in better agreement with experiment (see Figure 5.8). Of note, the radical electrons that are present in the SNapS2-generated molecules were converted to hydrogen atoms to ease the comparison with experimental results.

SNapS2-generated molecules with the full mechanism have a lower H/C ratio compared to molecules with an equal carbon number simulated with the reduced mechanism. This is expected as oxygen functional groups such as ketones will result in a lower H/C ratio than condensed aromatics due to the presence of the the double bond (C=O). For this reason, the full mechanism results in a large number of structures below the stabilomer line [159]. Some structures below the stabilomer line are also present for the pure hydrocarbon model as $-C\equiv CH$ groups and curvature also contribute to a lower H/C ratio. I note that there is generally a good agreement between experiment (based on AFM-identified PACs) and simulations. Comparing the H/C ratios at 8 mm and 14 mm, as shown in Figure 5.9, I do not observe any relevant change regardless of whether I use the full or reduced mechanism. As

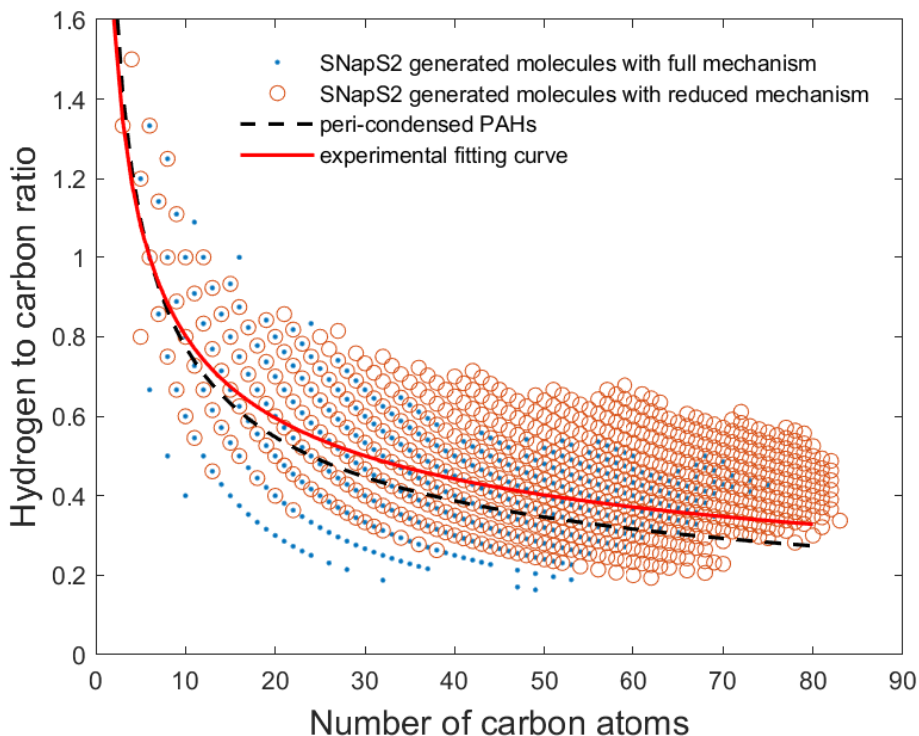


Figure 5.8: Hydrogen-to-carbon ratio with respect to the number of carbon atoms for SNapS2-generated molecules with full mechanism (blue dots) and reduced mechanism (red circles) at 8 mm. Peri-condensed PAHs (black dash line) and experimental fitting curve (red solid line) are from ref. [28].

we explained for the O/C ratios, this is also observed from the experiments, likely because most of the PAC chemical growth takes place before the nucleation zone (8 mm).

To complement the information provided by the H/C ratio, I also analyzed the characteristics of acyclic carbons, as shown in Figure 5.10. Among the groups with acyclic carbons, the methyl group seems to be very common in both AFM images (*e.g.*, **IS11**, **IS17**, and **IS57**) and SNapS2-generated molecules (*e.g.*, **ML22**, **ML24**, and **ML26**). However, while the simulation results show a large number of $-C\equiv CH$ groups (**ML17** through **ML21**) they are not seen in the AFM images. The formation of $-C\equiv CH$ group is an important step in a major pathway of the HACA pathways, which is considered the leading mechanism for pure hydrocarbon growth under many conditions, and therefore some $-C\equiv CH$ groups are expected to see in the AFM samples as well. I currently have no definitive explanation for this discrepancy on whether this phenomenon is an effect of the sampling/measure or if

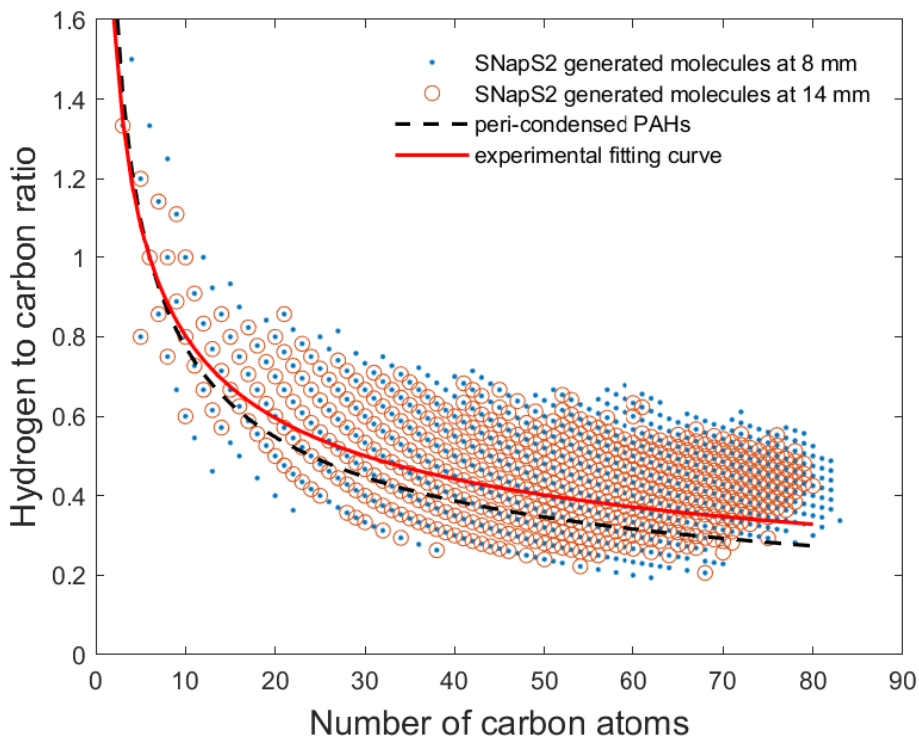


Figure 5.9: Hydrogen-to-carbon ratio with respect to the number of carbon atoms for SNapS2-generated pure hydrocarbons at 8 mm (blue dots) and 14 mm (red circles). Peri-condensed PAHs (black dash line) and experimental fitting curve (red solid line) are from ref. [28].

something is missing in the kinetic mechanism.

5.3.2.3 Ring Structures

While I observed a few example molecules containing only six-membered rings (**ML25** to **ML29**), most of the SNapS2-generated molecules contain at least one five-membered ring. For SNapS2-generated PACs, the number of five-membered rings is markedly lower than the number of six-membered rings, and the difference becomes larger at a higher number of carbon atoms, as shown in Figure 5.11. At the same time, the results indicate that at least a small number of five-membered rings are a general feature of the PACs. The results show more five-membered ring structures than the AFM images, but this difference can partially arise from the experimental difficulty to sample or analyze curved molecules. Therefore, I removed from simulation data the molecules with embedded five-membered

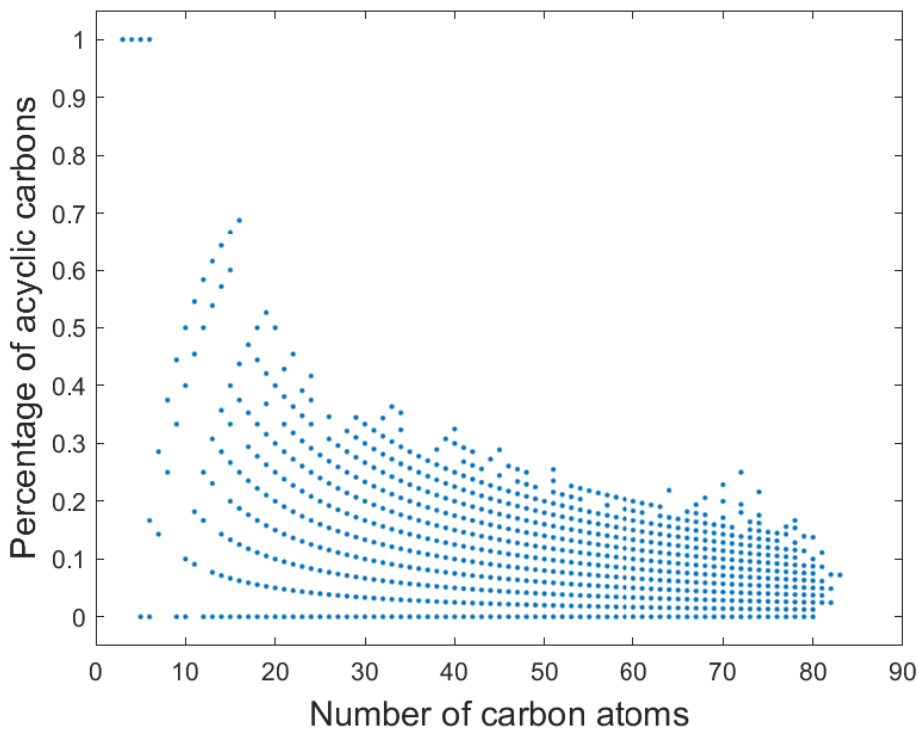


Figure 5.10: The percentage of acyclic carbon with respect to the number of carbon atoms for the SNapS2-generated molecules at an HAB of 8 mm of the premixed flame

rings, and compared the number of non-embedded five-membered rings from the remaining structures with the PACs from AFM images, as shown in Figure 5.12.

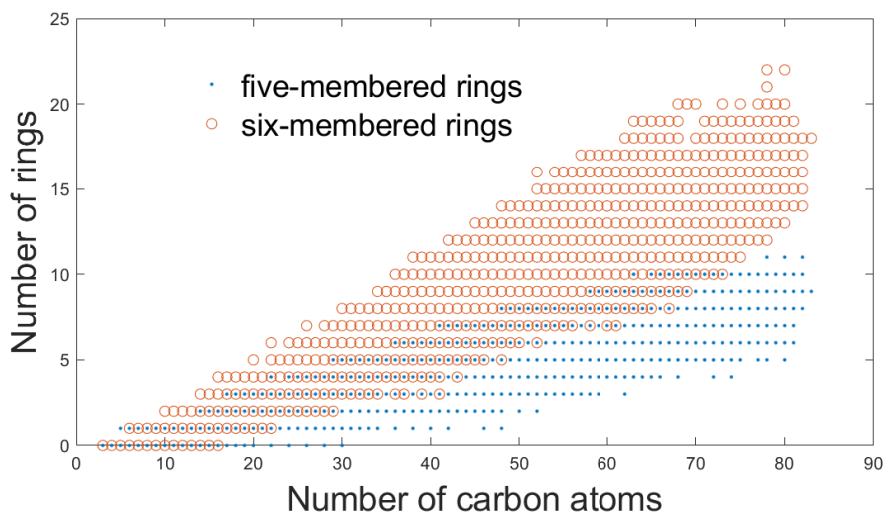


Figure 5.11: The number of five-membered (blue dots) and six-membered (red circles) rings with respect to the number of carbon atoms for the SNapS2-generated molecules at an HAB of 8 mm of the premixed flame

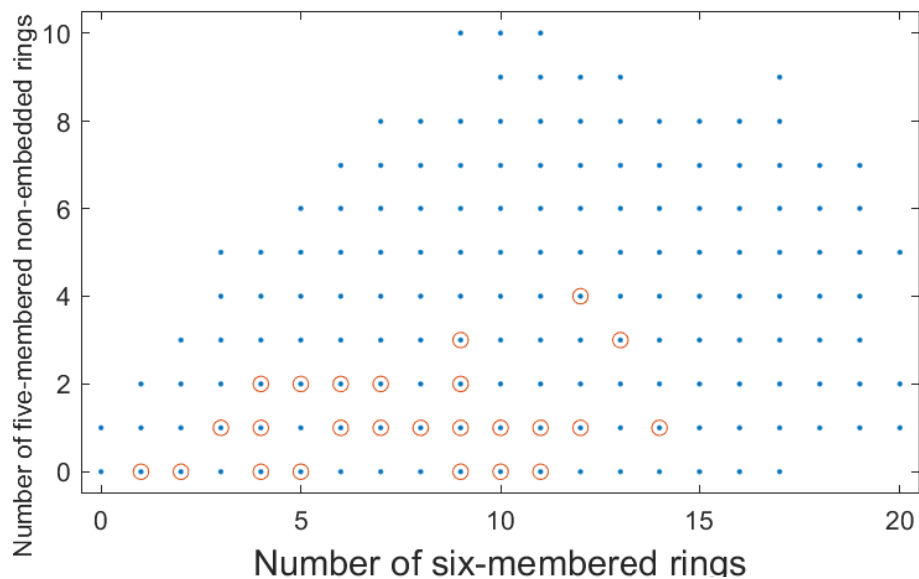


Figure 5.12: The number of non-embedded five-membered rings with respect to the number of six-membered rings for SNapS2-generated molecules (blue dots) and assigned PACs from AFM images (red circles) [28].

The comparison indicates that considering only the non-embedded five-membered rings, SNapS2-generated molecules may still have more five-membered rings compared to experimental data. The most likely reason for the overestimation is a lack of five-member ring oxidation or migration pathways in the current available literature, in addition to the reactions already included in the SNapS2 kinetic mechanism (such as ref. [55, 60]).

There are four types of five-membered rings identified by the AFM study, namely acenaphthylene-type, acenaphthene-type, fluorene-type, and indane-type. SNapS2 simulations show examples of the first three types (**ML7** to **ML24**) but the SNapS2 kinetic mechanism currently does not contain pathways that will lead to the formation of indane-type five-membered rings. Figure 5.13, which shows the frequency of different types of five-membered rings in the simulated structure, indicates that fluorene-type five-membered ring are prevalent in this flame. While there is some literature on the formation pathways of five-membered rings other than acenaphthylene type [129, 116], there is generally a lack of systematic study for the formation pathways of different types of five-membered rings and in the light of these and the AFM results, a more detailed analysis of five-membered

ring formation pathways is discussed previously in Chapter 4.2 in light of this. A more accurate description of the five-membered ring chemistry is also important because the large PACs which seem to be formed by cross-linking, can also be formed from small gas-phase species, as shown by **ML6**, **ML16**, and **ML23** which are similar to **IS30** and **IS43** from AFM studies.

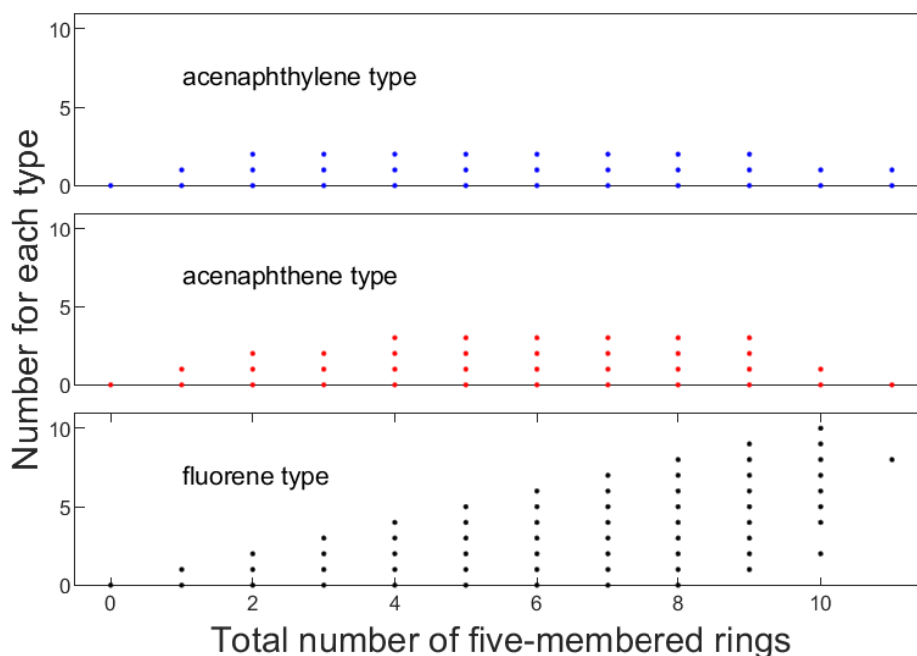


Figure 5.13: Frequency of the three types of five-membered rings formed in the SNApS2-generated molecules at 8 mm.

Of note, AFM images also show non-aromatic six-membered rings like **IS13** and **IS29**, a type of structure that SNApS2 simulations also produce like **ML11** and **ML27**, showing again the degree of accuracy in the prediction of SNApS2.

5.3.2.4 Curvatures of PACs

As mentioned above, I observe a large number of molecules, for example, **ML8**, **ML9**, **ML10**, **ML12**, **ML19**, **ML20**, **ML21**, and **ML22** which contain curvature. Since curved structures were difficult to sample or characterize in the cited AFM work, here I focus the discussion on the amount and frequency of the curvature I observe in SNApS2 traces more

than the atomistic details of the curved molecules. There are different ways to quantify the curvature of the molecules, but here I chose to use the value of the shortest principal axis of inertia (so that carbon would contribute more than hydrogen atoms) and divide it by the sum of all three axes, to make it size-independent. The results are shown in Figure 5.14.

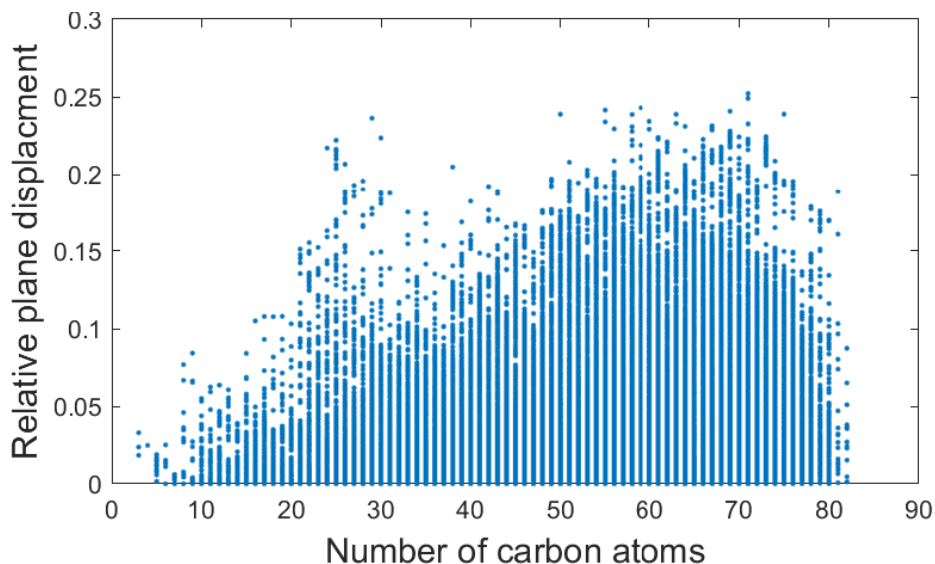


Figure 5.14: The relative plane displacement with respect to the number of carbon atoms

The plot shows a large number of molecules with little to no curvature, namely less than 0.05 (which is approximately the value caused by the presence of the aliphatic chain in ethylbenzene). A general increase in the curvature occurs with higher carbon numbers as more five-membered rings are added and additional growth occurs around previously embedded five-membered rings, while the drop above approximately 70 carbons is simply related to the simulation's upper mass limit. Interestingly, a peak for a set of molecules between 20 and 30 carbons can be observed, which is consistent with the number of carbons needed for a structure with embedded five-membered rings (such as **ML18**).

In general, the SNapS2-generated PACs show great similarities with the ones assigned experimentally showing that the kinetic mechanism includes the formation pathways of many experimentally observed functional groups. Together with the validations on the mass spectrum and oxygen contents, the SNapS2 kinetic mechanism provides a high-fidelity, and

yet generic model of the PAC formation under various combustion conditions, despite the constant need to expand the pool of possible reactions and refine kinetic rates when direct atomistic data is available. The SNapS2 showed a unique capability to match experimental findings and a strong ability to predict molecular structures of PACs formed in combustion, thus proves to be extremely useful in shedding light on the evolution of molecules from gas phase to soot precursors and contributes to reveal the underlying mechanisms to the experimental observations.

CHAPTER 6

Applications of the SNapS2 Beyond the Limitation of Diagnostics

SNapS2 code and the kinetic mechanism have shown its capability to provide valuable insights on the formation of aromatics beyond the limitation of diagnostics. For one application [182], spatial dependence of the PAC growth in an ethylene counterflow diffusion flame was characterized by SNapS2 simulations, revealing distinct PAC growth pathways for the streamlines starting from fuel side and oxidizer side. Given the fidelity of the SNapS2 predictions, it was also used to examine conditions that are impossible to test experimentally, like completely decoupling the effects of flame temperature when studying the effects of ethanol doping on the formation of aromatics [183], highlighting the chemical pathways that result in soot reduction. Both applications show the uniqueness and great potential of the model to obtain insights of the PAC formation when measurements are hard to obtain or experiments are difficult to control. I will discuss these two applications of SNapS2 in details in the following sections. The following sections are adapted from these publications [182, 183].

6.1 Spatial Dependence of the PAC Growth in an Ethylene Counterflow Diffusion Flame

While the diagnostics nowadays could provide sub-mm resolution for sampling the aerosol PAHs and soot particles, it is still very hard to study the impact of the local thermodynamic conditions on the spatial dependence of PACs because the effects of diffusion and sampling area are hard to be decoupled. Now with the SNapS2 code and mechanism being validated, it can be applied to shed light on this puzzle. The following section is adapted from this publication [182].

6.1.1 The Flame System

As combustion system, counterflow diffusion flames are ideal to study the effect of spatial differences in local environments. This configuration offers also the opportunity to isolate the reaction zone of the diffusion flame from radical trapping, heat loss and partial premixing at the burner [172], making them very attractive for the analysis of flame chemistry. The flame system in this study is the same as the one in Chapter 5.1.1. The graphs in Figure 6.1 report the CFD results for the time evolution of selected gas-phase species along two streamlines (i and l), highlighting the different chemical environments between the fuel side and the oxidizer side of the flame.

6.1.2 Reactivity Along the Centerline and Streamlines

To analyze the differences that stem from approximating the counterflow flame with a 1D model, I started by modeling the growth of soot precursors along the centerline. These SNapS2 simulations, however, did not result in any significant growth of soot precursors. When starting from the fuel side, I observed a negligible number of reactions because of the low temperature and radical concentrations. Simulations started on the oxidizer side displayed higher reactivity compared with those detected on the fuel side. However the

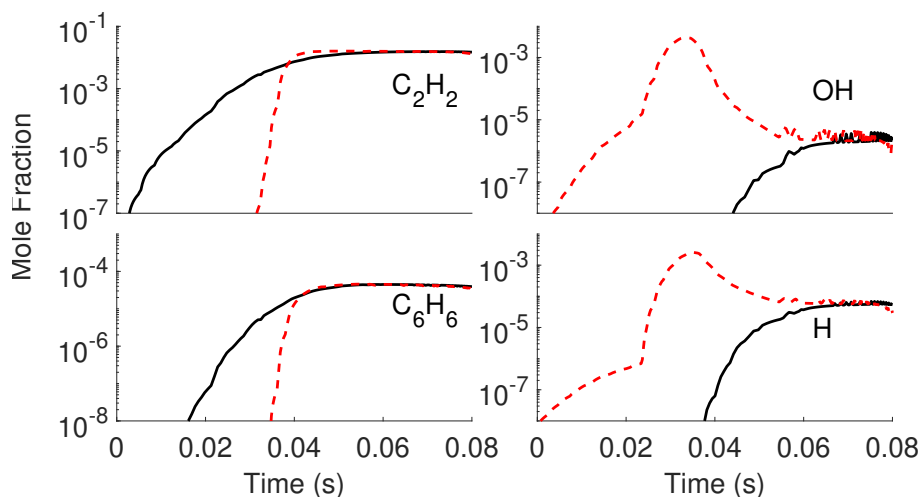


Figure 6.1: Time evolution of selected species. The evolution of selected species mole fractions are shown as a function of time along two streamlines identified in Figure 5.1. Species mole fractions for streamline i are shown as black solid lines, and for streamline l are shown as red dashed lines.

chemical changes were mostly limited to forward and corresponding reverse reactions (*e.g.*, oxygen addition that resulted in the formation of some small phenols, ethers, and furans), yielding no significant molecular growth. The results were consistent regardless of whether I used the centerline gas-phase concentrations from the CFD model or the one-dimensional CHEMKIN simulations as SNapS2 input. The outcome is not surprising, considering that the growth along the centerline can only happen in close proximity to the stagnation plane and over relatively long times. However, species lifetimes in this highly reactive region are limited by different diffusion phenomena that remove species from the reactive region. These phenomena, in addition to the small mass flow (compared to the total inlet flows) around the centerline, make the molecular growth along the centerline insignificant.

The analysis of the molecular evolution along the streamlines as shown in Figure 5.1, draws a different picture. Similarly to the centerline case, species starting from the oxidizer side undergo a large number of early reactions that are limited to forward and reverse reactions of oxygen addition but, when approaching the maximum temperature region, the molecules go through rapid growth forming a large number of oxy-PACs containing phenols, ethers and furan rings. On the fuel side, the molecular growth is negligible until the

streamlines approach the stagnation plane (a DFFO of 5.0 mm). At this point, SNapS2 simulations indicate a rapid molecular growth driven by the HACA mechanism, that is, the formation of five-membered and six-membered hydrocarbon rings through hydrogen abstraction (by various species) and acetylene addition, in agreement with previous studies [93, 127, 83, 81]. The mole fraction of the atomic hydrogen stays around 10^{-4} in this region, as shown in Figure 6.1. The difference in the dominant growth pathways between the oxidizer and fuel sides is consistent with the high acetylene and benzene concentrations and low amount of oxygen-containing gas-phase species (*e.g.*, hydroxyl radical) near the stagnation plane.

6.1.3 Spatial Dependence of the PAC Formation

Unlike the growth on the fuel side, where mostly pure hydrocarbons are formed by HACA pathways (*e.g.*, Figure 5.2), species following the streamlines on the oxidizer side go through different stages as they travel through distinct parts of the flame. This phenomenon can be seen from the SNapS2 simulation results for streamline *i*. While no significant molecular growth and extremely low atomic hydrogen mole fractions (shown in Figure 6.1) are observed before the transit time of 33 ms, a rapid molecular growth is detected when atomic hydrogen starts to accumulate in the gas-phase. Figure 6.2 shows the evolution of the mass spectra for streamline *i* at three different locations.

The top panel shows that the molecules crossing the maximum temperature region (DFFO of 5.9 mm, a Distance From the Centerline (DFC) of 0.57 mm, and transit time of 38 ms) are predicted to have a variety of structures with a relatively continuous distribution of masses, except for a few discernible peaks up to ~ 280 u. Compared with the mass spectra shown in Figure 5.2, there is a higher density of mass peaks because of the presence of oxygenated compounds at values of mass that would fall between peaks in a mostly pure hydrocarbon spectrum. The analysis of the reactions in this region shows that, while HACA pathways are responsible for the pure hydrocarbon part of the molecular growth,

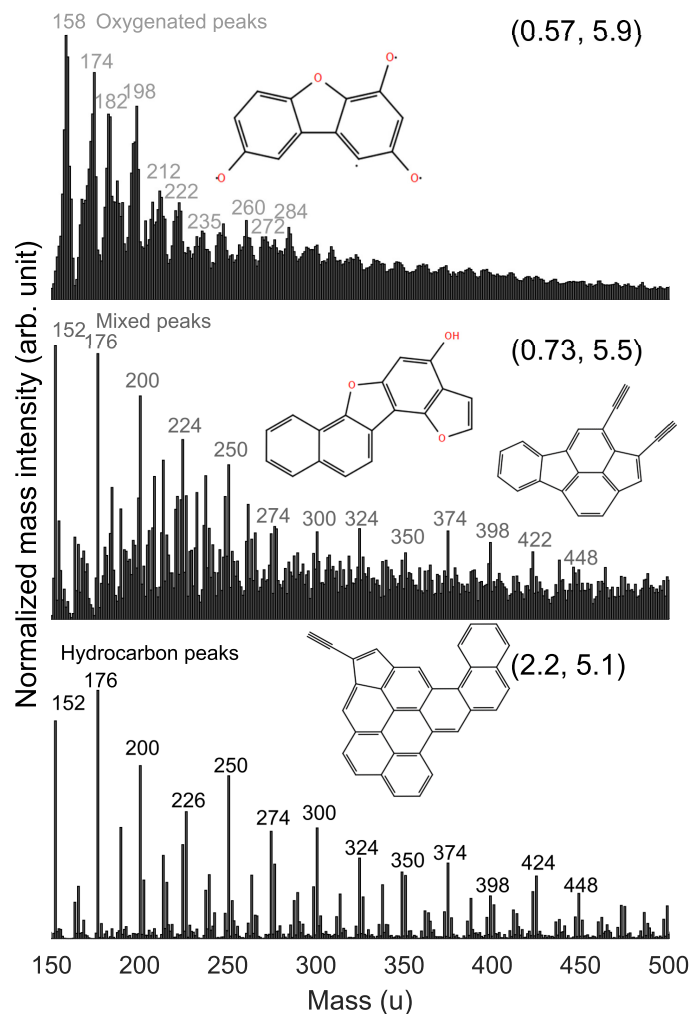


Figure 6.2: SNapS2-generated mass spectra at different locations along the streamline i. The coordinates (listed as DFC and DFFO in mm) of the center of the circular sampling region with diameter of 0.1 mm are reported on the top right corner between parentheses; molecular structures of example molecules that contribute to the peaks at 212 u (top), 274 u (middle), and 424 u (bottom) are shown in the respective panel.

a lot of phenols, ethers and furan-type structures are formed because of the high atomic oxygen concentration. The peaks of oxy-PACs predicted by SNapS2 correspond to those observed experimentally under very similar conditions [82].

The middle panel reports the changes in soot precursors mass right after passing through the maximum temperature region (at a DFFO of 5.5 mm, a DFC of 0.73 mm, time of 42 ms), where the mole fraction of atomic oxygen significantly decreases while acetylene

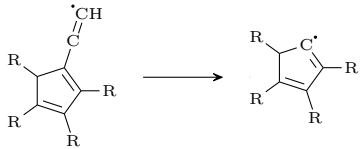
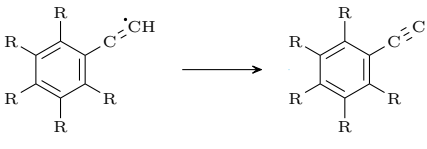
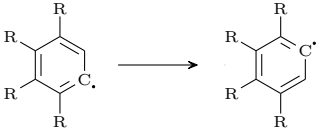
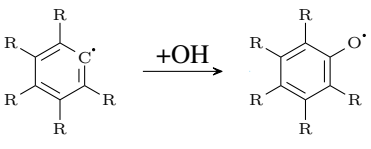
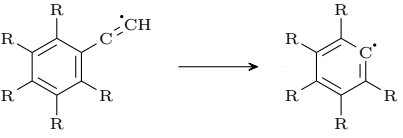
reaches its peak mole fraction. As expected, the molecular growth via HACA pathways become to be important and the number of molecules containing oxygen declines, as does the oxygen-to-carbon ratio. These phenomena can be seen in the appearance of stronger and isolated peaks in the mass spectra, despite the persistence of signal over the entire mass range. These peaks can be attributed to both pure hydrocarbons and oxygenated compounds. For example, the mass peak at 274 u is due to both oxy-PACs and pure hydrocarbons in approximately equal amounts; in the panel I show one example molecule from each group.

The situation changes again when approaching the stagnation plane (at a DFFO of 5.1 mm, a DFC of 2.2 mm, time of 60 ms), as shown in the lower panel. In this region, the growth is dominated by the HACA pathways, and pure hydrocarbons are mainly formed, leading to the well-defined peaks in the mass spectrum. At this point, the abundance of oxygenated compounds has dropped drastically; for example, the analysis of the structures with a mass of 424 u shows that only 2.8% of the molecules contributing to this mass peak contain oxygen atoms.

Statistical analysis of the reactions at these locations confirms the results discussed above. Table 6.1 shows the percentage of 5 generic reactions at the three locations corresponding to Figure 6.2, weighed by the lifespan of the reacting PACs. These 5 reactions are the ones with the highest percentage at (0.57, 5.9). As shown in the table, closer to the stagnation plane, there is a significant decrease in forming oxygenated species (reaction row 4) while HACA (pathway through row 2) starts to take over the whole chemical growth. It is worth mentioning that since the percentage is weighed by the lifespan of the reacting PACs, the acetylene breaking (row 1 and row 5) would take much longer time than acetylene attachment when chemical reactivity is very high at (0.57, 5.9). In terms of reaction numbers, more acetylene-attachment reactions occurs while taking much less time than acetylene breaking.

The results shown in Figure 6.2 and Table 6.1 demonstrate that the growth pathways

Table 6.1: The time percentages of 5 reactions at three locations of the flame in terms of (DFC, DFFO), weighed by the lifespan of the reacting PACs from SNapS2-simulated traces

Generic Reaction	(0.57, 5.9)	(0.73, 5.5)	(2.2, 5.1)
	13.3%	6.2%	0.7%
	12.2%	28.9%	37.5%
	10.1%	2.8%	0.06%
	6.4%	1.5%	0.04%
	6.1%	3.8%	0.8%

along the flow streamlines have a much more complicated evolution than the one that could be inferred by sampling only the centerline. Indeed, a variety of compounds are formed exclusively in certain parts of the flames, because of the strong dependencies on the exact time-history of the gas-phase (*i.e.*, composition and temperature)..

As conclusion, this study shows how the molecular chemical growth and the relative importance of different kinetic mechanisms change in different regions of the flame. Whereas HACA pathways dominate pure hydrocarbon growth on the fuel side of the flame and near stagnation plane, oxy-PACs are preferentially formed on the oxidizer side when crossing the maximum temperature region; in this location the high temperature and high concentration of oxygen atoms favor the formation of oxy-PACs. These oxy-PACs evolve to phenols

and ethers if they cross a region with low acetylene concentration; they grow to furan-embedded PACs if the acetylene concentration is high. Overall, these results show the importance of simulating the counterflow flame as a two- or three-dimensional system to capture the spatial dependence of soot precursors growth. Furthermore, the results show the importance of oxygen chemistry to accurately predict molecular growth in some spatial regions of the flame.

6.2 Effect of Ethanol on the Formation of Aromatics

Transportation is the largest consumer of petroleum-derived fuels in the world and the main emitter of atmospheric pollutants in urban centers [164]. Due to a growing energy demand, severe air pollution in cities, and more stringent environmental regulations in the road-transport sector, there is an enormous need to develop and find alternative fuel sources and technologies to reduce air pollutants from vehicular emissions. Ethanol has attracted widespread interest because it is easily obtained from renewable resources (bio-ethanol) and due to its versatile chemistry can be used as a fuel extender for petroleum-derived fuels, as an octane enhancer, and as a pure fuel [10]. The oxygen atom in ethanol's chemical structure can significantly change the main oxidation and molecular growth pathways [43]. Reactions not occurring during hydrocarbon combustion can be activated or enhanced by oxygen-borne atoms leading to high mass structures with covalently bonded oxygen, such as furan-embedded PACs [152].

There are many studies on how the doping of fuels with oxygenates (*e.g.*, methanol, ethanol, and methyl tertiary-butyl ether) alters the chemistry of the gas-phase [80, 95, 98, 63, 71] and the characteristics of the resulting soot particles [142, 29, 156, 72]. Among the main differences, the flame temperature [162], acetylene, and benzene mole fractions [195, 95, 51, 63, 142] generally decrease with increasing amount of ethanol doping, while hydrogen molecule and water mole fractions increase [63]. The increase in produced water

is considered to influence soot formation by altering the concentration of hydrogen atoms through the reaction $\text{H}_2\text{O} + \text{H} \longrightarrow \text{OH} + \text{H}_2$ [137, 142]. Experiments from shock-tube pyrolysis [59, 5] and premixed flames [142, 156] generally show that the addition of ethanol leads to a reduction in both size and total volume fraction of soot, although counterflow flame configurations show different behaviors on the fuel and the oxidizer side [143].

Less is known, however, about how ethanol doping changes the chemical composition and structure of large PACs that lead to incipient soot particles. Several recent studies [157, 82, 43, 182] have revealed the importance of including oxy-PAC structures in order to reconcile growth models with experimental observations. Elvati *et al.* [45, 43, 46, 44] indicated that the dimerization of PACs in general is affected by the shape of the molecules as well as the oxygen content, and that oxy-PACs have less tendency to form dimers than pure hydrocarbons with similar mass. Thus, a detailed modeling of PAC formation with ethanol doping would help us further understand the effect oxygenated fuels have on the transformation of small gas-phase species into soot particles.

In this work, I report the latest findings on the effect ethanol addition has on the formation and growth of aromatics in premixed ethylene flames. Six ethylene and ethanol-doped ethylene flames were analyzed using a combination of deterministic gas-phase modeling and stochastic computational techniques. I assessed and compared the relative importance of the observed molecular growth mechanisms for different flame conditions and stages in the combustion process. This section is adapted from this publication [183].

6.2.1 The Flame System

Past studies indicate that the flame temperature generally decreases when increasing the amount of ethanol doping [162]. For example, Wu *et al.* [195] observed this effect when characterizing a total of six ethylene/air and ethylene/ethanol/air flames. Since temperature profiles differ among these flames, temperature and gas-phase chemistry cannot be completely decoupled when studying the effects of ethanol doping. To avoid focusing on

temperature related differences, I modeled a set of flames keeping the temperature profiles nearly constant by solving the energy equations and adjusting the cold gas velocity to study the effect ethanol doping. A similar approach has been reported in benzene flames by Golea *et al.* [71]. I chose the ethylene/air (pure, or 0% doping) premixed flame by Wu *et al.* [195], which has an equivalence ratio (ϕ) of 2.34 and mass flux of $7.82 \text{ mg s}^{-1} \text{ cm}^{-2}$, as my reference system. Then the flame system was chosen to be a set of ethylene/ethanol/air flames with equivalence ratios of 2.34 and 2.64, and doping percentages (m/m) of 0 %, 20 % and 40 %.

6.2.2 Gas-phase Kinetic Mechanism

Several previous studies have developed multiple ethylene/ethanol combustion mechanisms. Wu *et al.* [195] used the base mechanism from Howard *et al.* [139], and augmented the ethanol reactions from Marinov [109]. Gerasimov *et al.* [63] tested three mechanisms against experimental measurements: the first consists of a base mechanism from Frenklach and coworkers [9, 180] and ethanol oxidation chemistry from Marinov [109]; the second from the USC-Mech-II mechanism [181] and again the ethanol oxidation from Marinov [109]; the last one, proposed by Konnov [94], includes the reactions for both ethylene and ethanol. Elvati *et al.* [43] has also applied a base ethylene mechanism developed by D'Anna and Kent [33] supplemented with ethanol oxidation reactions from Marinov [109]. However, none of these mechanisms include a variety of large PAHs.

In this study, I merged the KAUST mechanism II (KM2) [185] with the ethanol oxidation from Sarathy *et al.* [145]. Since the KM2 mechanism has species up to coronene (*i.e.*, $\text{C}_{24}\text{H}_{12}$), the newly merged mechanism enables to study the effect of ethanol doping on large PAHs up to 300 u with deterministic simulations. A total of 13 species and 111 reactions related to ethanol were merged with the KM2 mechanism.

6.2.3 Gas-phase Simulations

6.2.3.1 Gas-phase Mechanism Validation

To validate the new mechanism, I ran the PREMIX code implemented in the CHEMKIN software [135] with the merged mechanism. The results were compared with the gas-phase measurements by Gerasimov *et al.* [63] measuring premixed atmospheric-pressure fuel-rich ethylene/ oxygen/ argon (pure flame) and ethylene/ethanol/oxygen/argon (doped flame) with the same equivalence ratio ($\phi = 1.7$). The pure flame has a mole fraction of $C_2H_4/O_2/Ar = 0.088/0.155/0.757$, while the doped flame replaces 50% of ethylene with ethanol and has a mole fraction of $C_2H_4/C_2H_5OH/O_2/Ar = 0.044/0.044/0.155/0.757$. The flow rate for both flames was maintained at $25.8 \text{ cm}^3 \text{ s}^{-1}$. The experimental temperature profiles were input into the PREMIX code to minimize the uncertainty when modeling the heat loss from the energy equations. Figure 6.3 compares the results with experimental measurements for both pure and doped flames.

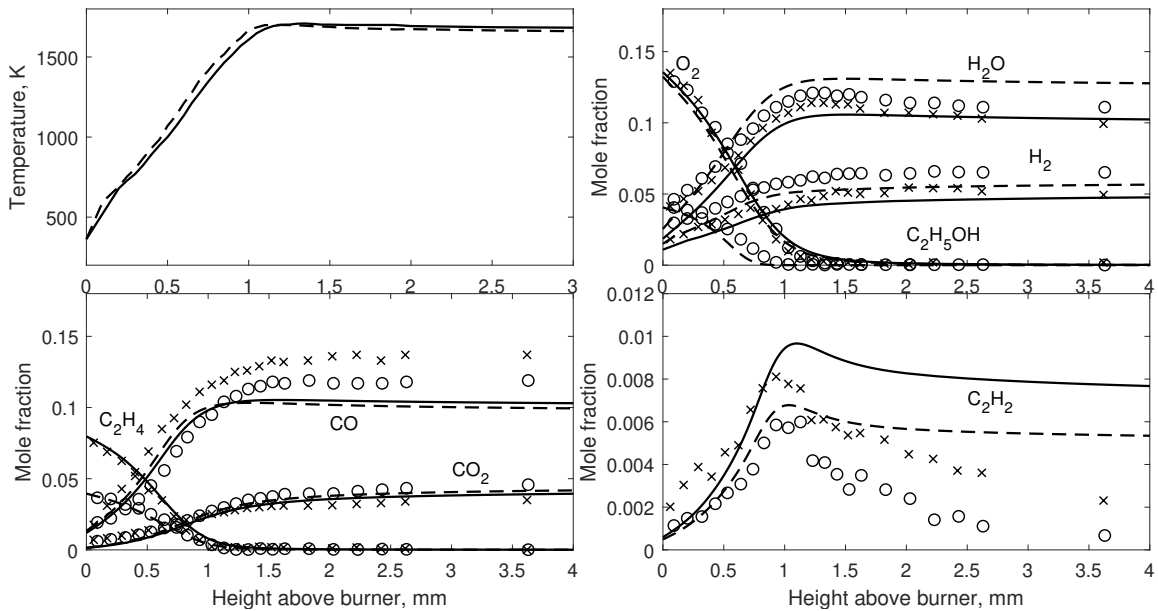


Figure 6.3: Comparison between experimentally and computed properties of the pure (solid lines) and 50% doped (dashed lines) systems. Upper left panel shows the experimentally measured temperature [63], while the other panels show the mole fraction evolution of selected gas-phase species, from modeling (lines) and experiments (symbols) of pure (cross) and doped flame (circles).

At almost all heights, the new mechanism predicts the fuel (C_2H_4 and C_2H_5OH), oxidizer (O_2), and the final combustion products' (H_2O , CO , and CO_2) mole fractions with less than 20% deviation from the experimental measurements. While the new mechanism captures some of the intermediate species profiles such as H_2 , others, such as C_2H_2 , are not well-predicted after the peak location. Despite this discrepancy, the computed C_2H_2 mole fraction profile is similar to previous simulation work of this flame by Gerasimov *et al.* [63] and the relative difference in C_2H_2 mole fraction between the pure and doped flames matches well with experimental data.

Still, it is important to consider the degree to which this C_2H_2 deviation might affect the stochastic modeling results. First, the mechanism is able to capture the C_2H_2 mole fraction profile before the concentration peak, which represents the region of the flame with the most rapid PAC chemical growth. Furthermore, although the computed mole fraction of C_2H_2 can be up to three times larger than the experimental values, this discrepancy will only result in a small difference on the comparatively large rate of a typical acetylene addition reaction (*e.g.*, $1.65 \times 10^{12} \text{ cm}^3 \text{ mol}^{-1} \text{ s}^{-1}$ for C_2H_2 addition to phenyl radical at 1500 K [103]). Thus even with these differences in C_2H_2 mole fraction, I expect the PAC growth rate to be affected only marginally.

In addition, I verified that the merged mechanism does not substantially change the base mechanism (KM2). Simulations performed with both the base and the merged mechanisms on the pure ethylene flame resulted in only minor differences (less than 1%) across all species. Overall, I consider the gas-phase mechanism adequate for my simulations.

6.2.3.2 Gas-phase Modeling Results

With the new mechanism being validated, now I applied this mechanism to the chosen flame system, *i.e.*, a set of ethylene/ethanol/air flames with equivalence ratios of 2.34 and 2.64, and doping percentages (m/m) of 0 %, 20 % and 40 %, using the PREMIX code implemented in the CHEMKIN software [135], to keep the temperature profiles nearly constant

by solving the energy equations and adjusting the cold gas velocity. Then the computed gas-phase species in the set of six flames was compared to assess the effect of ethanol doping on gas-phase species distributions. Figure 6.4 shows the mole fractions of gas-phase species C_6H_6 , C_2H_2 , H_2 , and H_2O for all six flame conditions. Mole fractions of H_2O are similar for both equivalence ratios, while higher equivalence ratios yield larger mole fractions of C_6H_6 , C_2H_2 , and H_2 which is to be expected for a more sooting flame. Within the same equivalence ratio, increasing ethanol doping percentage results in less C_2H_2 and C_6H_6 and more H_2 and H_2O .

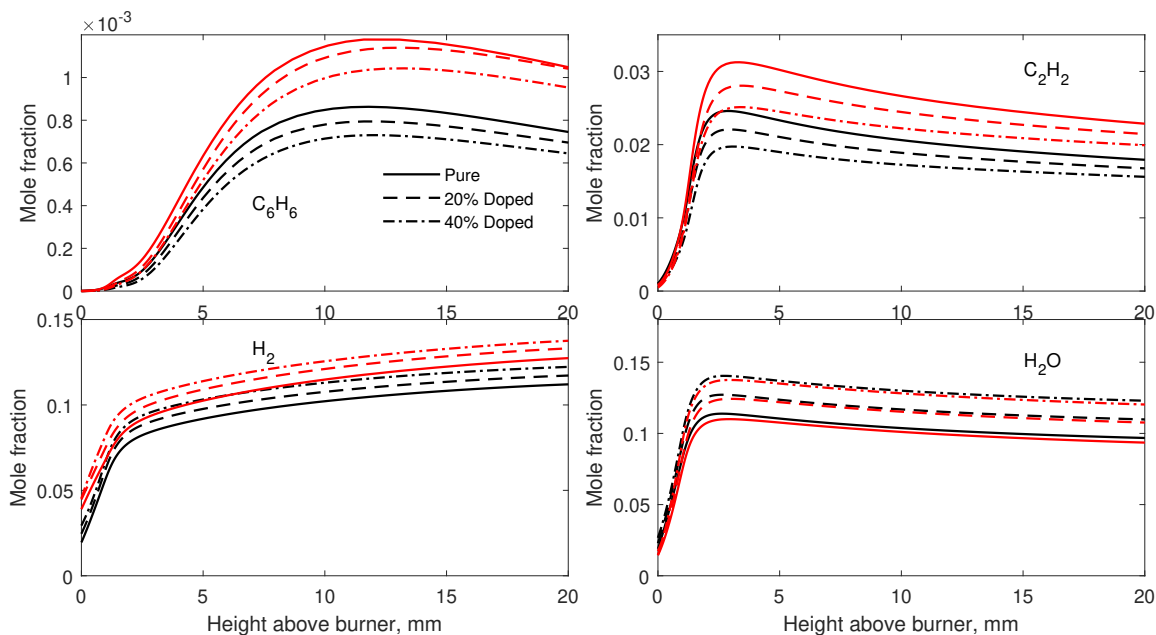


Figure 6.4: Mole fraction profiles of selected species from gas-phase modeling results for the set of six flames. Solid lines represent pure flames, dashed lines 20% doped flames, dash-dot line 40% doped flames; equivalence ratio is indicated by the color: black for 2.34 and red for 2.64.

These trends agree with the observations from previous experimental studies. Several studies observed a reduction of C_2H_2 when doping with ethanol and considered this to be one of the reasons for a decrease in soot formation [80, 98, 195, 51, 142]. The reduction of C_6H_6 , which is the principal species for small aromatics, was observed by Wu *et al.* [195]. Finally, an increase in H_2O was seen by Salamanca *et al.* who suggested that it reduced soot formation by removing H atoms through the reaction $H_2O + H \rightarrow OH + H_2$ [142].

Since the KM2 mechanism contains species with molecular masses up to coronene, I also analyzed how the amount of small aromatics (one to two rings) and large PAHs (three or more rings) are affected by ethanol doping (see Figure 6.5).

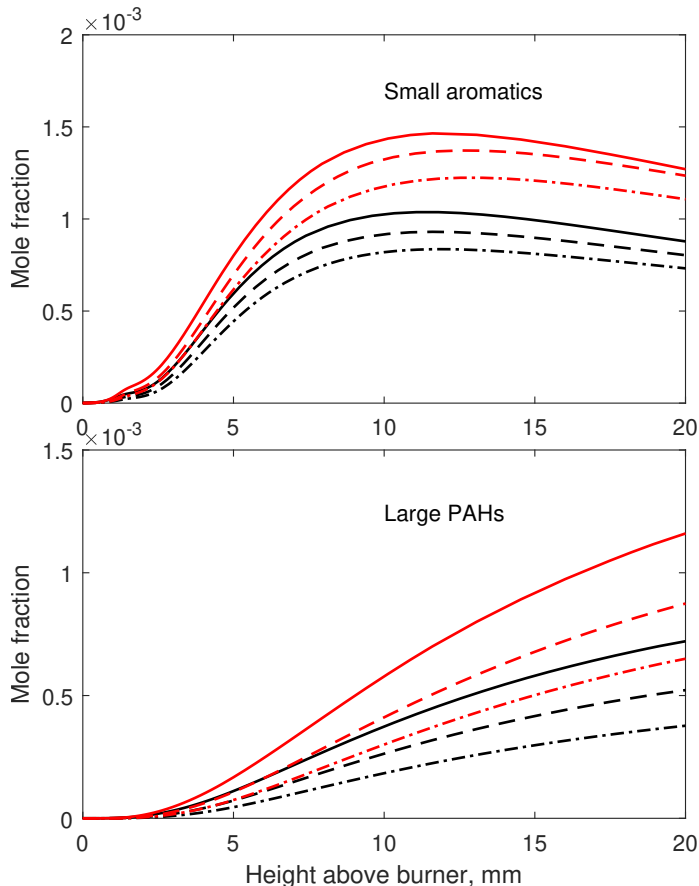


Figure 6.5: Mole fractions of small aromatics (one to two rings, upper) and large PAHs (three or more rings, lower) from gas-phase simulations for the set of six flames. Solid lines represent pure flames, dashed lines 20% doped flames, dash-dot line 40% doped flames; equivalence ratio is indicated by the color: black for 2.34 and red for 2.64.

Benzene makes up most of the small aromatics (one or two aromatic rings). Thus, the mole fraction profiles look very similar to the C_6H_6 profiles shown in Figure 6.4. The small aromatics grow rapidly after an HAB of 2 mm, where both H and C_2H_2 reach their peak values (H profile is shown in Figure 6.7), and start to decay after an HAB of 10 mm where they are consumed to form other species such as larger PAHs. The mole fraction of large PAHs is mostly comprised of acenaphthylene (A2R5, $C_{12}H_8$), cy-

clopenta[cd]pyrene (A4R5, C₁₈H₁₀), and anthanthrene (C₂₂H₁₂). Unlike small aromatics, the large PAHs steadily accumulate in the gas-phase since no consumption of these species is included in the model (*e.g.*, physical aggregation). Interestingly, two of the most common large aromatics contain five-membered rings and at all times have mole fractions larger than pyrene. This observation demonstrates the important role that five-membered rings play in PAC growth mechanisms [96], even when a simplified PAC mechanism is considered.

For all cases, the mole fractions of both small aromatics and large PAHs decay with an increase in ethanol doping percentage. A reduction of 20% and 50% of large PAHs is observed when doping 20% and 40% ethanol into ethylene/air premixed flames.

6.2.4 Stochastic Simulations

Some of the small gas-phase species from the CHEMKIN results were used as inputs to SNapS2 to study the PAC formation mechanisms. Benzene, cyclopentadiene, and phenol were selected as seeds for the SNapS2 simulations using the criteria introduced in Chapter 2. A total of 32,000 traces were simulated across all three seeds and six conditions, and the final properties were obtained by weighting each trace based on the seed mole fractions at the starting location of each trace. While SNapS2 can simulate chemical growth of PACs of any size, different processes start to be relevant at high molecular mass (above 800 u – 1000 u) [41, 154, 45] and therefore I stopped the simulations when species reached a mass of 600 u. In the 32,000 simulations, I observed a total of ~ 61.5 million reactions, of which 10.2 million were unique, and 6.1 million different PACs.

While gas-phase modeling can simulate growth trends for a select number of small aromatics and large PAHs, it cannot reproduce the vast diversity of the PACs as it is limited by the number of species. On the other hand, SNapS2 provides detailed atomistic information of the PAC evolution in the flame. To compare the two types of modeling, I computed the PAC chemical growth rate for the flames, by averaging the molecular growth of different traces starting at the same location, and the cumulative chemical growth, obtained by inte-

grating the chemical growth rate from height above the burner of 0 mm. Of note, different time intervals should be considered when integrating to compensate for differences in the gas flow rate. The results for all the flames are shown in Figure 6.6.

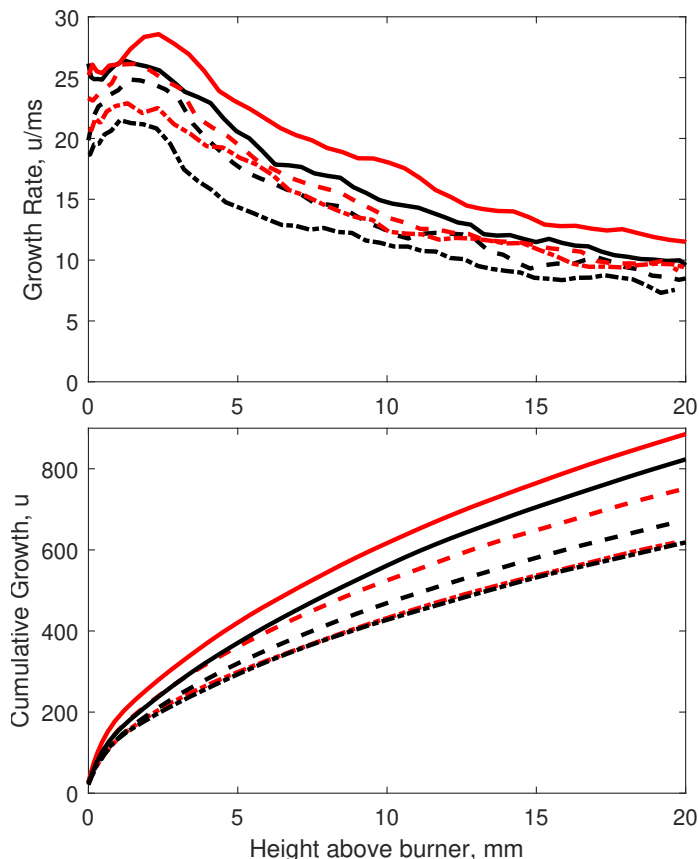


Figure 6.6: Average (upper panel) and cumulative (lower panel) chemical growth of PACs as a function of height above the burner from SNapS2 simulations for the set of six flames. Solid lines represent pure flames, dashed lines 20% doped flames, dash-dot line 40% doped flames; equivalence ratio is indicated by the color: black for 2.34 and red for 2.64.

The plot shows a noticeable reduction in PAC chemical growth when increasing the ethanol doping percentage and when decreasing the equivalence ratio. This is in agreement with the results of the CHEMKIN simulations (Figure 6.5 lower panel). However, SNapS2 simulations indicate that the growth starts earlier than the deterministic gas-phase simulations due to the inclusion of reactions for the formation of PACs with oxygenated groups.

To understand the contribution of oxygenated species to the growth of PACs, I com-

puted the percentage of PACs that contained at least one oxygen at different HABs. To avoid biasing the results by including a large number of unstable species, all the PACs were weighted by their lifetime. Oxy-PACs were largely observed between 2 mm and 4 mm, which correspond to the region with the maximum growth rate and around the location where both O and H concentrations peak, as shown in Figure 6.7. Collectively, these results indicate that a large portion of the initial growth is due to the oxy-PACs, and that is the reason why it was not captured by the deterministic simulations.

While there are some small differences between the 6 flames, both the location and the fraction of oxy-PACs is not markedly affected by the doping level or the ϕ . This is in line with the low sensitivity of the O and H mole fractions to the doping percentage, except for a small increase in H with increasing ethanol content, likely a result of removing the effect of temperature. A similar effect on the O and H mole fractions has been shown by Golea *et al.* [71] when doping premixed benzene flames with ethanol and removing the temperature effects.

This similarity has important implications, since O is critical for PAH oxidation as indicated by several studies [82, 55]. Considering that the reaction pathways for oxy-PACs usually start by attaching an O atom to an aromatic site, it is reasonable to assume that similar mole fractions of gas-phase oxidizing radicals is the reason for similar percentages of oxy-PACs. At the same time, the increase in H mole fraction corresponds to decrease in PAC growth, whether considering the deterministic model or the stochastic simulations.

It is worth noting that when the temperatures were not held constant by changing the flow velocity, this trend would not hold either. Doping ethanol generally decreases the flame temperature [162]. This would then lower the O and H concentrations, as lower flame temperatures will usually lead to lower radical concentrations, and therefore the percentage of oxy-PACs is also expected to decrease.

The mole fraction of C_2H_2 also peaks around the same location as O, which makes this environment ideal for the formation of furan-embedded PACs [82, 182]. Analysis of the

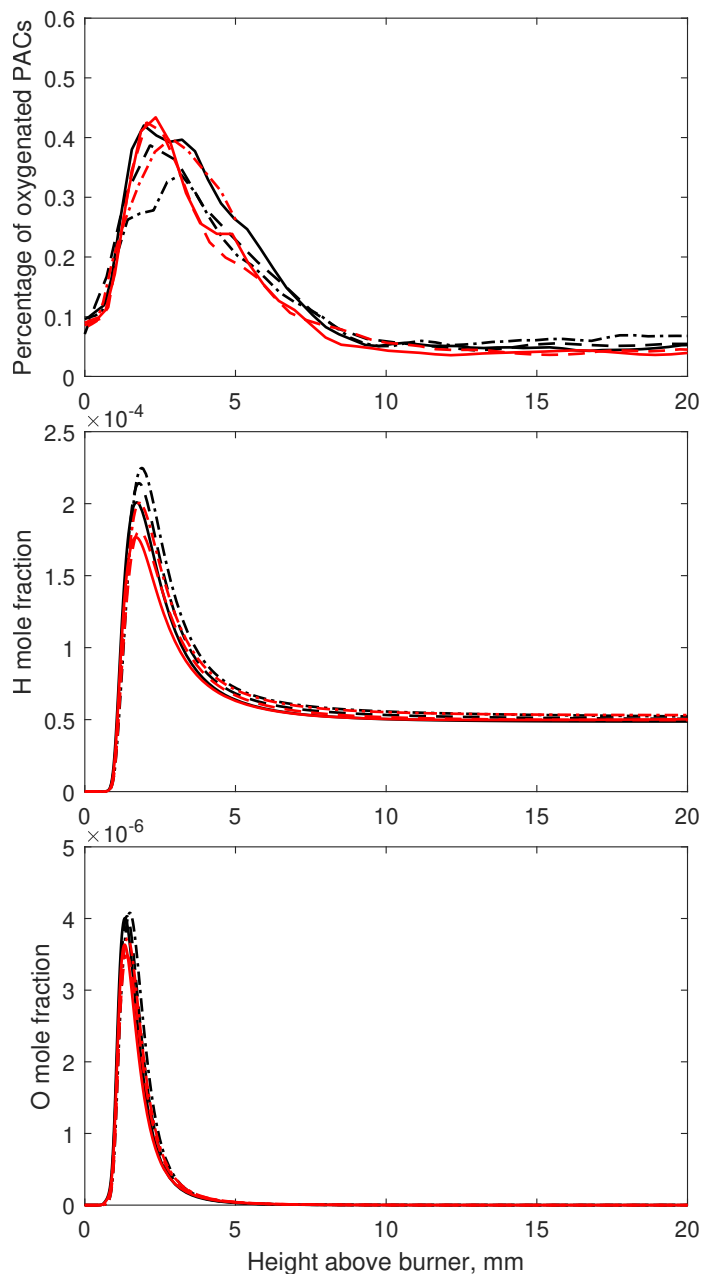


Figure 6.7: Upper panel: percentage of oxy-PACs in different flames as a function of HAB from SNapS2 simulations; Middle and bottom panel: the mole fraction profiles for atomic hydrogen and atomic oxygen from gas-phase simulations correspondingly. Solid lines represent pure flames, dashed lines 20% doped flames, dash-dot line 40% doped flames; equivalence ratio is indicated by the color: black for 2.34 and red for 2.64.

formed oxygenated structures shows that most of the oxy-PACs are phenols, 15% are furans, and a small amount are ethers. Interestingly, SNapS2 simulations indicate that the formation and decomposition of PACs containing oxygenated groups happen frequently.

Figure 6.8 shows the evolution of three examples of traces for the pure ethylene/air premixed flame with an equivalence ratio of 2.34. While some of the furan rings are preserved at high HAB (trace 1, upper), others disappear (trace 2, middle). As the formation of phenols and ethers are highly reversible at these conditions, aromatic molecules frequently transform between pure hydrocarbons and oxy-PACs.

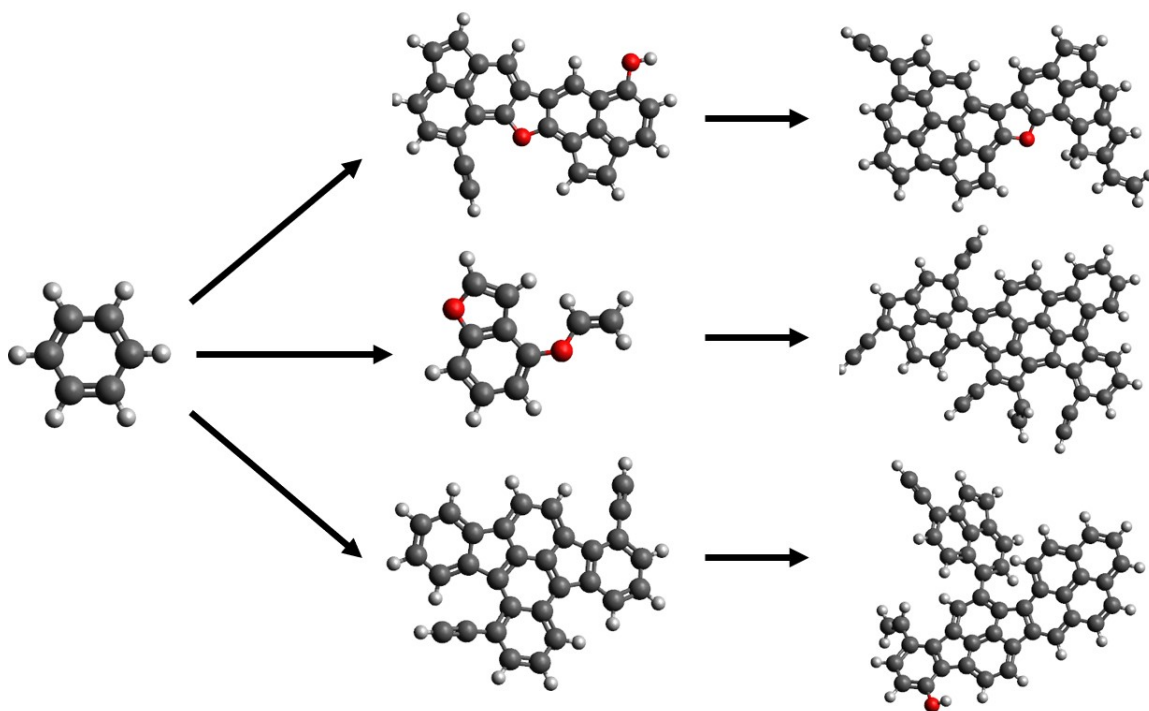
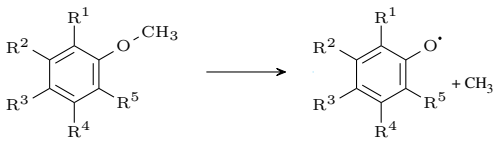
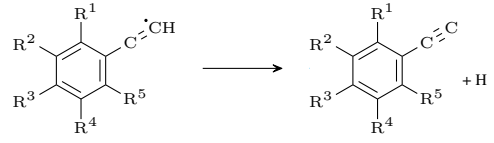
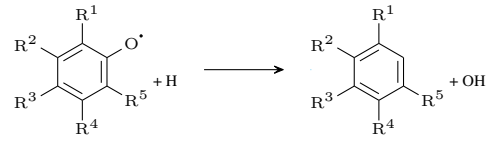
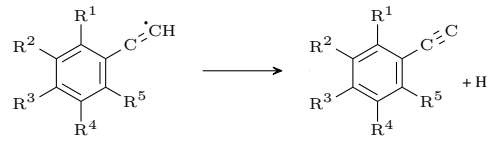
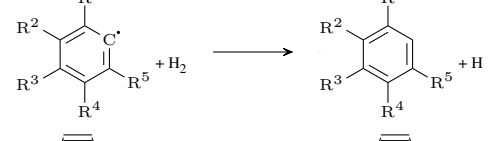
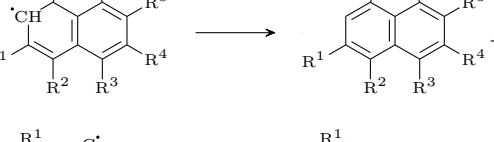
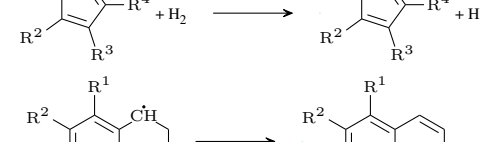
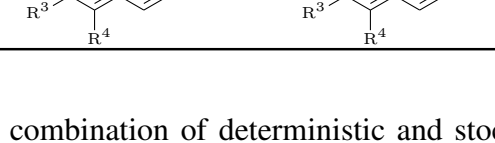


Figure 6.8: Example of compounds predicted in the pure ethylene/air premixed flame with equivalence ratio of 2.34 using benzene as seed molecule. Atoms in dark, grey, and red correspond to carbon, hydrogen, and oxygen atoms. The molecules on the second and third column are sampled at an HAB of 2 mm and 10 mm respectively.

Statistical analysis of the reactions happening at different flame locations helps elucidate the PAC growth phenomena. Table 6.2 shows the top 5 generic reactions at HABs of 2 mm and 10 mm, weighed by the lifetime of the reacting PACs for the pure ethylene/air premixed flame with an equivalence ratio of 2.34. This analysis validates many of the points discussed above. Oxygen chemistry dominates around an HAB of 2 mm, while the major formation route for HACA is more relevant at 10 mm. At the same time the rapid decomposition of the oxy-PACs indicates that these reactions provide only an initial increase

in PACs size and that they are not responsible for the sustained growth of PACs.

Table 6.2: Most frequent/relevant/important reactions occurring in SNapS2 simulation in the pure ethylene/ air premixed flame with equivalence ratio of 2.34, at different HAB.

Reaction (HAB = 2 mm)	Relevance
	17.6%
	12.4%
$R^1-CH_3 + H \longrightarrow R^1-\dot{C}H_2 + H_2$	9.8%
	9.4%
$R^1-\dot{C}H_2 + H_2 \longrightarrow R^1-CH_3 + H$	9.3%
Reaction (HAB = 10 mm)	Relevance
	27.4%
	24.5%
	11.4%
	10.8%
	9.7%

In this study, a combination of deterministic and stochastic simulations was used to study the effect of ethanol addition on the formation of PACs. Six ethylene/air premixed

flames with two equivalence ratios (2.34 and 2.64) and three different amounts of ethanol doping (0 %, 20 % and 40 % by mass) were analyzed. By adjusting the cold gas velocity, an almost identical temperature profile was kept among all the systems in order to remove the effect of temperature from our analysis.

The gas-phase was modeled with a newly merged combustion mechanism that includes both ethanol oxidation and the growth of large PAHs. This mechanism was validated against experimental measurements from literature. The simulations for the selected system show that the addition of ethanol causes a slight increase of H but a reduction of acetylene, small aromatics, and large PAHs in agreement with previous works available in the literature. By increasing the ethanol doping percentage, C_2H_2 , C_6H_6 , small aromatics and large PAHs show more reductions from deterministic simulations.

These reductions are also observed from the stochastic simulations, where both chemical growth rate and cumulative growth of the PACs are reduced when the ethanol doping percentage is increased. The doping however does not strongly affect the amount of oxygenated PACs nor the type of oxygenated groups, because the mole fraction profiles of both atomic oxygen and atomic hydrogen are almost identical among six flames, as a result of decoupling the effect of flame temperature. The number of oxy-PACs reach a maximum at a height above burner around 2 mm–3 mm where they constitute 45% of all the PACs: most of the oxygenated structures are phenols, mixed with approximately 15% of furans, and a small amount of ethers. The rate of PAC growth then gradually slows down, with pure hydrocarbon growth mechanisms being the main contributors in this region of the flame. Overall, the results indicate that the formation pathways of oxygenated PACs can compete with pure hydrocarbon growth mechanisms in the rapid growth region up to a height above burner of 2 mm–3 mm. These oxy-PACs are responsible for the rapid growth of the precursors at low HABs, while HACA reactions cause a slower growth that is sustained along the whole flame.

CHAPTER 7

Conclusions and Future Work

Understanding the formation of polycyclic aromatic compounds (PACs) in combustion not only bridges the knowledge gap between the small gas-phase species and incipient soot particles, but may also help address the global emission issues of both PACs and soot. In this thesis, I present a fully-reversible, thermodynamically-consistent, and sterically-resolved kinetic mechanism with 396 generic reactions describing PAC growth in combustion. These reactions were then implemented by 430 reactive SMARTS for a stochastic modeling code (*i.e.*, SNapS2) recently developed by the Violi Group. While the SNapS2 code utilizes kinetic Monte Carlo scheme to enable simulations of the chemical growth in different gas-phase environments (*e.g.*, chemical vapor deposition, non-thermal plasma), the kinetic mechanism is targeted at the formation of PACs in combustion systems. Reactions are gathered and categorized from various literature to address some new experimental and computational discoveries, such as the presence of furan-embedded PACs, ketones, aliphatic side chains, and types of five-membered rings, as well as the growth mechanisms of aromatics other than the hydrogen-abstraction-acetylene(C_2H_2)-addition mechanism. Some missing reaction pathways were identified from experimental evidences and simulations, namely the formation of furan-embedded PACs and types of five-membered rings. Quantum chemistry calculations have been carried out for those pathways. These newly discovered reactions were then compared with major competing pathways and further included in the kinetic mechanism as well.

The characteristics of the PACs predicted with the kinetic mechanism were compared against different experimental measurements: mass spectra measured in a counterflow diffusion flame, the oxygen-to-carbon ratios obtained at different locations of a coflow diffusion flame, and the molecular structures observed in a premixed laminar flame. The simulation results show excellent agreement with experimental mass spectrum taken by aerosol mass spectrometry coupled with vacuum-ultraviolet photoionization in the range of 200 u to 450 u in terms of peak locations and intensities in an ethylene counterflow flame, reproduce the diverse array of oxygenated PACs observed experimentally between 150 u and 450 u in a coflow diffusion Jet A-1 surrogate flame, and capture the PACs in terms of a large variety of functional groups characterized experimentally by atomic force microscopy in an ethylene premixed flame. These successful validations demonstrate that the SNapS2 kinetic mechanism provides a high-fidelity, and yet generic description of the PAC formation under various combustion conditions, making SNapS2 the first-of-its-kind to have such extensive validations. The SNapS2 code and the kinetic mechanism showed a unique capability to match experimental findings, thus proves to be extremely useful in shedding light on the evolution of molecules from gas phase to soot precursors and contributes to reveal the underlying mechanisms to the experimental observations.

In addition to these validations, SNapS2 code and the kinetic mechanism have also shown its capability to provide valuable insights on the formation of aromatics beyond the limitation of diagnostics. As one application of the SNapS2, spatial dependence of the PAC growth in an ethylene counterflow diffusion flame was characterized, revealing different PAC growth mechanisms for the streamlines starting from fuel side and oxidiser side. Whereas HACA pathways dominate pure hydrocarbon growth on the fuel side of the flame and near stagnation plane, oxy-PACs are preferentially formed on the oxidizer side when crossing the maximum temperature region; in this location the high temperature and high concentration of oxygen atoms favor the formation of oxy-PACs. These oxy-PACs evolve to phenols and ethers if they cross a region with low acetylene concentration; they grow to

furan-embedded PACs if the acetylene concentration is high. Overall, these results show the importance of simulating the counterflow flame as a two- or three-dimensional system to capture the spatial dependence of soot precursors growth. Furthermore, the results show the importance of oxygen chemistry to accurately predict molecular growth in some spatial regions of the flame.

Given the fidelity of the SNapS2 predictions, it was also used to examine conditions that are impossible to test experimentally, like completely decoupling the effects of flame temperature when studying the effects of ethanol doping on the formation of aromatics, highlighting the chemical pathways that result in soot reduction. From stochastic modeling results, both chemical growth rate and cumulative growth of the PACs are reduced when the ethanol doping percentage is increased. The doping however does not strongly affect the amount of oxy-PACs nor the type of oxygenated groups, because the mole fraction profiles of both atomic oxygen and atomic hydrogen are almost identical among all the flames, as a result of decoupling the effect of flame temperature. The number of oxy-PACs reach a maximum at a height above burner around 2 mm–3 mm where they constitute 45% of all the PACs: most of the oxygenated structures are phenols, mixed with approximately 15% of furans, and a small amount of ethers. The rate of PAC growth then gradually slows down, with pure hydrocarbon growth mechanisms being the main contributors in this region of the flame. Overall, the results indicate that the formation pathways of oxygenated PACs can compete with pure hydrocarbon growth mechanisms in the rapid growth region up to a height above burner of 2 mm–3 mm. These oxy-PACs are responsible for the rapid growth of the precursors at low HABs, while HACA reactions cause a slower growth that is sustained along the whole flame. Both applications show the uniqueness and great potential of the model to obtain insights of the PAC formation when measurements are hard to obtain or experiments are difficult to control.

The future work includes implementation of the radical-radical combination and the study of the physical growth. While SNapS2 code and the kinetic mechanism have done

an extraordinary job on predicting the PAC formation in the range of 200 u to 450 u from both the mass spectrum and oxygen content, it starts to be less accurate beyond 600 u. The reason for that is likely to be the radical-radical combination [81, 43]. In the current SNapS2 code, the molecules can only react with small gas-phase species (with molecular mass less than benzene) and they cannot meet each other. But if two PACs both have radical sites, they could react and likely react fast, *i.e.*, the radical-radical combination. Elvati *et al.* [43] have done some investigations on this topic, and showed that by including radical-radical combination, the mass spectrum is significantly shifted toward higher masses. So the next step for the SNapS2 could be the implementation of this. In addition, utilizing the PACs obtain from SNapS2, the building blocks of the primary particles, further study of the physical growth [45, 43, 46, 44] would be beneficial. Physical growth becomes relevant for molecular masses beyond 1000 u. A combination of the SNapS2 and a physical growth model would help reveal the soot formation process in great detail.

Altogether, this dissertation laid a solid foundation that not only helps explain the experimental observations for the formation of soot precursors, but also provides a powerful tool for exploring the gas-phase nanoparticle growth that could drive the development of novel combustion technologies or the design of new nanomaterials.

BIBLIOGRAPHY

- [1] ABDEL-SHAFY, H. I., AND MANSOUR, M. S. M. A review on polycyclic aromatic hydrocarbons: Source, environmental impact, effect on human health and remediation. *Egypt. J. Pet.* 25, 1 (2016), 107–123. 1
- [2] ADKINS, E., AND MILLER, J. Extinction measurements for optical band gap determination of soot in a series of nitrogen-diluted ethylene/air non-premixed flames. *Phys. Chem. Chem. Phys.* 17, 4 (2015), 2686–2695. 67
- [3] AGUILERA-IPARRAGUIRRE, J., CURRAN, H. J., KLOPPER, W., AND SIMMIE, J. M. Accurate Benchmark Calculation of the Reaction Barrier Height for Hydrogen Abstraction by the Hydroperoxyl Radical from Methane. Implications for C_nH_{2n+2} where $n = 2 \rightarrow 4$. *J. Phys. Chem. A* 112, 30 (July 2008), 7047–7054. 24
- [4] AKAZAWA, M., KOJIMA, Y., AND KATO, Y. Formation of Polycyclic Compounds from Phenols by Fast Pyrolysis. *EC Agriculture* 1, 2 (feb 2015), 67–85. 41
- [5] ALEXIOU, A., AND WILLIAMS, A. Soot formation in shock-tube pyrolysis of toluene, toluene-methanol, toluene-ethanol, and toluene-oxygen mixtures. *Combust. Flame* 104, 1 (1996), 51 – 65. 88
- [6] ALTARAWNEH, M., AL-MUHTASEB, A. H., DLUGOGORSKI, B. Z., KENNEDY, E. M., AND MACKIE, J. C. Theoretical Study on the Thermodynamic Properties and Self-Decomposition of Methylbenzenediol Isomers. *J. Phys. Chem. A* 114, 43 (Nov. 2010), 11751–11760. 23, 47
- [7] ALTARAWNEH, M., AL-MUHTASEB, A. H., DLUGOGORSKI, B. Z., KENNEDY, E. M., AND MACKIE, J. C. Rate constants for hydrogen abstraction reactions by the hydroperoxyl radical from methanol, ethenol, acetaldehyde, toluene, and phenol. *J. Comput. Chem.* 32, 8 (June 2011), 1725–1733. 23, 27, 48
- [8] ALZUETA, M. U., GLARBORG, P., AND DAM-JOHANSEN, K. Experimental and kinetic modeling study of the oxidation of benzene. *Int. J. Chem. Kinet.* 32, 8 (2000), 498–522. 23, 27, 48
- [9] APPEL, J., BOCKHORN, H., AND FRENKLACH, M. Kinetic modeling of soot formation with detailed chemistry and physics: Laminar premixed flames of C_2 hydrocarbons. *Combust. Flame* 121, 1 (Apr. 2000), 122–136. 4, 7, 89

- [10] BALAT, M., AND BALAT, H. Recent trends in global production and utilization of bio-ethanol fuel. *Appl. Energy* 86, 11 (2009), 2273–2282. 87
- [11] BAO, J. L., ZHENG, J., AND TRUHLAR, D. G. Kinetics of Hydrogen Radical Reactions with Toluene Including Chemical Activation Theory Employing System-Specific Quantum RRK Theory Calibrated by Variational Transition State Theory. *J. Am. Chem. Soc.* 138, 8 (Mar. 2016), 2690–2704. 23
- [12] BATEMAN, A., LASKIN, J., LASKIN, A., AND NIZKORODOV, S. Applications of high-resolution electrospray ionization mass spectrometry to measurements of average oxygen to carbon ratios in secondary organic aerosols. *Environ. Sci. Technol.* 46, 15 (2012), 8315–8324. 66
- [13] BITTNER, J., AND HOWARD, J. Composition profiles and reaction mechanisms in a near-sooting premixed benzene/oxygen/argon flame. *Proc. Combust. Inst.* 18, 1 (1981), 1105–1116. Eighteenth Symposium (International) on Combustion. 4, 33, 50
- [14] BÖHM, H., AND JANDER, H. PAH formation in acetylene–benzene pyrolysis. *Phys. Chem. Chem. Phys.* 1, 16 (1999), 3775–3781. 4, 20
- [15] BOTERO, M. L., CHEN, D., GONZÁLEZ-CALERA, S., JEFFERSON, D., AND KRAFT, M. HRTEM evaluation of soot particles produced by the non-premixed combustion of liquid fuels. *Carbon* 96 (2016), 459–473. 5, 6
- [16] BOTERO, M. L., SHENG, Y., AKROYD, J., MARTIN, J., DREYER, J. A., YANG, W., AND KRAFT, M. Internal structure of soot particles in a diffusion flame. *Carbon* 141 (2019), 635 – 642. 51
- [17] BURCAT, A., RUSCIC, B., CHEMISTRY, AND OF TECH., T. I. I. Third millenium ideal gas and condensed phase thermochemical database for combustion (with update from active thermochemical tables). 17
- [18] BURKE, S. M., METCALFE, W., HERBINET, O., BATTIN-LECLERC, F., HAAS, F. M., SANTNER, J., DRYER, F. L., AND CURRAN, H. J. An experimental and modeling study of propene oxidation. Part 1: Speciation measurements in jet-stirred and flow reactors. *Combust. Flame* 161, 11 (Nov. 2014), 2765–2784. 24
- [19] CAIN, J., LASKIN, A., KHOLGHY, M. R., THOMSON, M. J., AND WANG, H. Molecular characterization of organic content of soot along the centerline of a coflow diffusion flame. *Phys. Chem. Chem. Phys.* 16, 47 (Oct. 2014), 25862–25875. 5, 41, 63, 64, 65, 66
- [20] CAIN, J. P., GASSMAN, P. L., WANG, H., AND LASKIN, A. Micro-FTIR study of soot chemical composition - Evidence of aliphatic hydrocarbons on nascent soot surfaces. *Phys. Chem. Chem. Phys.* 12, 20 (2010), 5206–5218. 5, 32

- [21] CARSTENSEN, H.-H., AND DEAN, A. M. Rate constant rules for the automated generation of gas-phase reaction mechanisms. *J. Phys. Chem. A* 113, 2 (Jan. 2009), 367–380. 23, 26
- [22] CARSTENSEN, H.-H., DEAN, A. M., AND DEUTSCHMANN, O. Rate constants for the H abstraction from alkanes (R–H) by R[•] O₂ radicals: A systematic study on the impact of R and R. *Proc. Combust. Inst.* 31, 1 (2007), 149–157. 23
- [23] CELNIK, M., RAJ, A., WEST, R., PATTERSON, R., AND KRAFT, M. Aromatic site description of soot particles. *Combust. Flame* 155, 1-2 (Oct. 2008), 161–180. 9
- [24] CHUNG, S. H., AND VIOLI, A. Insights on the nanoparticle formation process in counterflow diffusion flames. *Carbon* 45, 12 (Oct. 2007), 2400–2410. 8, 9, 23, 35
- [25] COHEN, N., AND WESTBERG, K. R. The use of transition-state theory to extrapolate rate coefficients for reactions of O atoms with alkanes. *Int. J. Chem. Kinet.* 18, 1 (Jan. 1986), 99–140. 24
- [26] COMMODO, M., D’ANNA, A., FALCO, G. D., LARCIPRETE, R., AND MINUTOLO, P. Illuminating the earliest stages of the soot formation by photoemission and Raman spectroscopy. *Combust. Flame* 181 (2017), 188–197. 5, 6, 41
- [27] COMMODO, M., FALCO, G. D., LARCIPRETE, R., D’ANNA, A., AND MINUTOLO, P. On the hydrophilic/hydrophobic character of carbonaceous nanoparticles formed in laminar premixed flames. *Exp. Therm. Fluid Sci.* 73 (2016), 56 – 63. Special issue on Ninth Mediterranean Combustion Symposium. 41
- [28] COMMODO, M., KAISER, K., FALCO, G. D., MINUTOLO, P., SCHULZ, F., D’ANNA, A., AND GROSS, L. On the early stages of soot formation: Molecular structure elucidation by high-resolution atomic force microscopy. *Combust. Flame* 205 (2019), 154–164. 5, 6, 11, 32, 33, 38, 51, 55, 68, 69, 71, 73, 74, 76
- [29] COMMODO, M., TESSITORE, G., FALCO, G. D., MINUTOLO, P., AND D’ANNA, A. Photoionization Study of Soot Precursor Nanoparticles in Laminar Premixed Ethylene/Ethanol Flames. *Combust. Sci. Technol.* 186, 4-5 (2014), 621–633. 87
- [30] DA SILVA, G., COLE, J. A., AND BOZZELLI, J. W. Kinetics of the Cyclopentadienyl + Acetylene, Fulvenallene + H, and 1-Ethynylcyclopentadiene + H Reactions. *J. Phys. Chem. A* 114, 6 (Feb. 2010), 2275–2283. 32
- [31] DAGAUT, P., AND GAÏL, S. Chemical Kinetic Study of the Effect of a Biofuel Additive on Jet-A1 Combustion. *J. Phys. Chem. A* 111, 19 (2007), 3992–4000. 63
- [32] DAMES, E., AND WANG, H. Isomerization kinetics of benzylic and methylphenyl type radicals in single-ring aromatics. *Proc. Combust. Inst.* 34, 1 (Jan. 2013), 307–314. 39, 40, 48

- [33] D'ANNA, A., AND KENT, J. A model of particulate and species formation applied to laminar, nonpremixed flames for three aliphatic-hydrocarbon fuels. *Combust. Flame* 152, 4 (2008), 573–587. 89
- [34] D'ANNA, A., AND VIOLI, A. A kinetic model for the formation of aromatic hydrocarbons in premixed laminar flames. *Proc. Combust. Inst.* 27, 1 (Jan. 1998), 425–433. 31, 34
- [35] DAVIS, C., FELLIN, P., AND OTSON, R. A review of sampling methods for polyaromatic hydrocarbons in air. *J. Air Waste Manag. Assoc.* 37, 12 (1987), 1397–1408. 66
- [36] DAVIS, M. E., AND DAVIS, R. J. *Fundamentals of Chemical Reaction Engineering*. McGraw-Hill Chemical Engineering Series. McGraw-Hill Education, 2003. 7, 18
- [37] DAVIS, S. G., LAW, C. K., AND WANG, H. Propyne Pyrolysis in a Flow Reactor: An Experimental, RRKM, and Detailed Kinetic Modeling Study. *J. Phys. Chem. A* 103, 30 (1999), 5889–5899. 38, 39
- [38] DAYLIGHT CHEMICAL INFORMATION SYSTEMS, INC. Simplified molecular input line entry specification, 2019. 18
- [39] DAYLIGHT CHEMICAL INFORMATION SYSTEMS, INC. Smiles arbitrary target specification, 2019. 18
- [40] DU, D., AXELBAUM, R., AND LAW, C. The influence of carbon dioxide and oxygen as additives on soot formation in diffusion flames. *Symposium (International) on Combustion* 23, 1 (Jan. 1991), 1501–1507. 41
- [41] D'ANNA, A. Combustion-formed nanoparticles. *Proc. Combust. Inst.* 32, 1 (2009), 593–613. 69, 94
- [42] D'ANNA, A., VIOLI, A., D'ALESSIO, A., AND SAROFIM, A. A reaction pathway for nanoparticle formation in rich premixed flames. *Combust. Flame* 127, 1-2 (Oct. 2001), 1995–2003. 51
- [43] ELVATI, P., DILLSTROM, V., AND VIOLI, A. Oxygen driven soot formation. *Proc. Combust. Inst.* 36, 1 (2017), 825–832. 1, 3, 11, 34, 38, 41, 42, 47, 67, 69, 71, 87, 88, 89, 104
- [44] ELVATI, P., TURRENTINE, K., AND VIOLI, A. The role of molecular properties on the dimerization of aromatic compounds. *Proc. Combust. Inst.* 37, 1 (2019), 1099–1105. 1, 34, 41, 67, 88, 104
- [45] ELVATI, P., AND VIOLI, A. Thermodynamics of poly-aromatic hydrocarbon clustering and the effects of substituted aliphatic chains. *Proc. Combust. Inst.* 34, 1 (2013), 1837–1843. 1, 34, 51, 69, 71, 88, 94, 104

- [46] ELVATI, P., AND VIOLI, A. Homo-dimerization of oxygenated polycyclic aromatic hydrocarbons under flame conditions. *Fuel* 222 (2018), 307 – 311. 1, 34, 41, 67, 71, 88, 104
- [47] EMDEE, J. L., BREZINSKY, K., AND GLASSMAN, I. A kinetic model for the oxidation of toluene near 1200 K. *J. Phys. Chem.* 96, 5 (Mar. 1992), 2151–2161. 27, 48
- [48] F. MAUSS, AND H. BOCKHORN. Soot Formation in Premixed Hydrocarbon Flames: Prediction of Temperature and Pressure Dependence. *Zeitschrift für Physikalische Chemie* 188, 1 (Jan. 1995), 45–60. 3
- [49] FAHR, A., AND STEIN, S. E. Gas-phase reactions of phenyl radicals with aromatic molecules. *J. Phys. Chem. A* 92, 17 (Aug. 1988), 4951–4955. 27
- [50] FORST, W. Unimolecular Reactions - A Concise Introduction. Cambridge University Press, 2003, p. 172. 41
- [51] FRASSOLDATI, A., FARAVELLI, T., RANZI, E., KOHSE-HÖINGHAUS, K., AND WESTMORELAND, P. R. Kinetic modeling study of ethanol and dimethyl ether addition to premixed low-pressure propene–oxygen–argon flames. *Combust. Flame* 158, 7 (2011), 1264–1276. 87, 92
- [52] FRENKLACH, M. On surface growth mechanism of soot particles. *Proc. Combust. Inst.* 26, 2 (1996), 2285–2293. 3, 9, 23, 30
- [53] FRENKLACH, M. Reaction mechanism of soot formation in flames. *Phys. Chem. Chem. Phys.* 4, 11 (May 2002), 2028–2037. 2, 23, 33
- [54] FRENKLACH, M., CLARY, D. W., GARDINER, W. C., AND STEIN, S. E. Detailed kinetic modeling of soot formation in shock-tube pyrolysis of acetylene. *Proc. Combust. Inst.* 20, 1 (1985), 887–901. 2, 4, 33, 51
- [55] FRENKLACH, M., LIU, Z., SINGH, R. I., GALIMOVA, G. R., AZYAZOV, V. N., AND MEBEL, A. M. Detailed, sterically-resolved modeling of soot oxidation: Role of O atoms, interplay with particle nanostructure, and emergence of inner particle burning. *Combust. Flame* 188 (Feb. 2018), 284–306. 9, 10, 23, 29, 35, 37, 38, 49, 76, 96
- [56] FRENKLACH, M., SCHUETZ, C. A., AND PING, J. Migration mechanism of aromatic-edge growth. *Proc. Combust. Inst.* 30, 1 (Jan. 2005), 1389–1396. 2, 9, 29, 33, 39, 51
- [57] FRENKLACH, M., SINGH, R. I., AND MEBEL, A. M. On the low-temperature limit of HACA. *Proc. Combust. Inst.* 37, 1 (2019), 969–976. 2, 4, 23, 33
- [58] FRENKLACH, M., AND WANG, H. Detailed modeling of soot particle nucleation and growth. *Proc. Combust. Inst.* 23, 1 (Jan. 1991), 1559–1566. 2, 4, 33

- [59] FRENKLACH, M., AND YUAN, T. Effect of alcohol addition on shock-initiated formation of soot from benzene. *Proceedings of the 16th International Symposium on Shock Tubes and Waves*, 16 (1987), 487–493. 88
- [60] GALIMOVA, G., AZYAZOV, V., AND MEBEL, A. Reaction mechanism, rate constants, and product yields for the oxidation of Cyclopentadienyl and embedded five-member ring radicals with hydroxyl. *Combust. Flame* 187 (Jan. 2018), 147–164. 35, 38, 76
- [61] GARDINER, W. C. Shock tube studies of combustion chemistry. In *Shock Waves* (Berlin, Heidelberg, 1992), K. Takayama, Ed., Springer Berlin Heidelberg, pp. 49–60. 3
- [62] GEORGANTA, E., RAHMAN, R. K., RAJ, A., AND SINHA, S. Growth of polycyclic aromatic hydrocarbons (pahs) by methyl radicals: Pyrene formation from phenanthrene. *Combust. Flame* 185 (2017), 129 – 141. 52
- [63] GERASIMOV, I. E., KNYAZKOV, D. A., YAKIMOV, S. A., BOLSHOVA, T. A., SHMAKOV, A. G., AND KOROBENICHEV, O. P. Structure of atmospheric-pressure fuel-rich premixed ethylene flame with and without ethanol. *Combust. Flame* 159, 5 (2012), 1840–1850. 87, 89, 90, 91
- [64] GIACCAI, J. A., AND MILLER, J. H. Examination of the electronic structure of oxygen-containing PAH dimers and trimers. *Proc. Combust. Inst.* 37, 1 (2019), 903–910. 34, 41
- [65] GILLESPIE, D. T. A general method for numerically simulating the stochastic time evolution of coupled chemical reactions. *J. Comput. Phys.* 22, 4 (Dec. 1976), 403–434. 8
- [66] GILLESPIE, D. T. Exact stochastic simulation of coupled chemical reactions. *J. Phys. Chem.* 81, 25 (Dec. 1977), 2340–2361. Publisher: American Chemical Society. 8
- [67] GILLESPIE, D. T., HELLANDER, A., AND PETZOLD, L. R. Perspective: Stochastic algorithms for chemical kinetics. *J. Chem. Phys.* 138, 17 (May 2013), 170901. 7, 8, 15
- [68] GIRI, B. R., FERNANDES, R. X., BENTZ, T., HIPPLER, H., AND OLZMANN, M. High-temperature kinetics of propyne and allene: Decomposition vs. isomerization. *Proc. Combust. Inst.* 33, 1 (2011), 267–272. 38, 39
- [69] GOEL, A., HEBGEN, P., SANDE, J. B. V., AND HOWARD, J. B. Combustion synthesis of fullerenes and fullerene nanostructures. *Carbon* 40, 2 (2002), 177–182. 2
- [70] GOLDSMITH, C. F., KLIPPENSTEIN, S. J., AND GREEN, W. H. Theoretical rate coefficients for allyl + HO₂ and allyloxy decomposition. *Proc. Combust. Inst.* 33, 1 (2011), 273–282. 24

- [71] GOLEA, D., REZGUI, Y., GUEMINI, M., AND HAMDANE, S. Reduction of PAH and soot precursors in benzene flames by addition of ethanol. *J. Phys. Chem. A* 116, 14 (Dec. 2012), 3625–3642. 87, 89, 96
- [72] GRIFFIN, E. A., CHRISTENSEN, M., AND GÜLDER, O. L. Effect of ethanol addition on soot formation in laminar methane diffusion flames at pressures above atmospheric. *Combust. Flame* 193 (2018), 306 – 312. 87
- [73] GUO, H., LIU, F., SMALLWOOD, G., AND GULDER, O. A numerical investigation of thermal diffusion influence on soot formation in ethylene/air diffusion flames. *Int. J. Comput. Fluid Dyn.* 18, 2 (2004), 139–151. 66
- [74] HANSON, R., AND DAVIDSON, D. Recent advances in laser absorption and shock tube methods for studies of combustion chemistry. *Prog. Energy Combust. Sci.* 44 (Oct. 2014), 103–114. 3
- [75] HE, Y. Z., MALLARD, W. G., AND TSANG, W. Kinetics of hydrogen and hydroxyl radical attack on phenol at high temperatures. *J. Phys. Chem.* 92, 8 (Apr. 1988), 2196–2201. 27, 43, 48
- [76] HEALY, D., DONATO, N. S., AUL, C. J., PETERSEN, E. L., ZINNER, C. M., BOURQUE, G., AND CURRAN, H. J. Isobutane ignition delay time measurements at high pressure and detailed chemical kinetic simulations. *Combust. Flame* 157, 8 (Aug. 2010), 1540–1551. 24
- [77] HEALY, D., DONATO, N. S., AUL, C. J., PETERSEN, E. L., ZINNER, C. M., BOURQUE, G., AND CURRAN, H. J. n-Butane: Ignition delay measurements at high pressure and detailed chemical kinetic simulations. *Combust. Flame* 157, 8 (Aug. 2010), 1526–1539. 24
- [78] HEMELSOET, K., MORAN, D., VAN SPEYBROECK, V., WAROQUIER, M., AND RADOM, L. An Assessment of Theoretical Procedures for Predicting the Thermochemistry and Kinetics of Hydrogen Abstraction by Methyl Radical from Benzene. *J. Phys. Chem. A* 110, 28 (July 2006), 8942–8951. 23
- [79] HWANG, J., CHUNG, S., AND LEE, W. Effects of oxygen and propane addition on soot formation in counterflow ethylene flames and the role of C3 chemistry. *Symposium (International) on Combustion* 27, 1 (Jan. 1998), 1531–1538. 41
- [80] INAL, F., AND SENKAN, S. Effects of oxygenate additives on polycyclic aromatic hydrocarbons (PAHs) and soot formation. *Combust. Sci. Technol.* 174, 9 (2002), 1–19. 41, 87, 92
- [81] JOHANSSON, K. O., DILLSTROM, T., ELVATI, P., CAMPBELL, M. F., SCHRADER, P. E., POPOLAN-VAIDA, D. M., RICHARDS-HENDERSON, N. K., WILSON, K. R., VIOLI, A., AND MICHELSEN, H. A. Radical–radical reactions, pyrene nucleation, and incipient soot formation in combustion. *Proc. Combust. Inst.* 36, 1 (2017), 799–806. 37, 67, 69, 83, 104

- [82] JOHANSSON, K. O., DILLSTROM, T., MONTI, M., EL GABALY, F., CAMPBELL, M. F., SCHRADER, P. E., POPOLAN-VAIDA, D. M., RICHARDS-HENDERSON, N. K., WILSON, K. R., VIOLI, A., AND MICHELSEN, H. A. Formation and emission of large furans and oxygenated hydrocarbons from flames. *Proc. Natl. Acad. Sci. U.S.A.* *113*, 30 (July 2016), 8374–8379. 5, 6, 11, 34, 37, 38, 41, 42, 43, 47, 51, 84, 88, 96
- [83] JOHANSSON, K. O., LAI, J. Y. W., SKEEN, S. A., POPOLAN-VAIDA, D. M., WILSON, K. R., HANSEN, N., VIOLI, A., AND MICHELSEN, H. A. Soot precursor formation and limitations of the stabilomer grid. *Proc. Combust. Inst.* *35*, 2 (2015), 1819–1826. 83
- [84] JOHANSSON, K. O., ZÁDOR, J., ELVATI, P., CAMPBELL, M. F., SCHRADER, P. E., RICHARDS-HENDERSON, N. K., WILSON, K. R., VIOLI, A., AND MICHELSEN, H. A. Critical Assessment of Photoionization Efficiency Measurements for Characterization of Soot-Precursor Species. *J. Phys. Chem. A* *121*, 23 (2017), 4475–4485. 62
- [85] JU, L., AND WANG, D. Kinetic Isotope Effects for the $H_2 + C_2H \rightleftharpoons C_2H_2 + H$ Reaction Based on the Ab Initio Calculations and a Global Potential Energy Surface. *Int. J. Chem. Kinet.* *42*, 5 (2010), 289–298. 24
- [86] KANG, K., HWANG, J., CHUNG, S., AND LEE, W. Soot zone structure and sooting limit in diffusion flames: Comparison of counterflow and co-flow flames. *Combust. Flame* *109*, 1 (1997), 266 – 281. 66
- [87] KEE, R. J., RUPLEY, F. M., AND MILLER, J. A. Chemkin-ii: A fortran chemical kinetics package for the analysis of gas-phase chemical kinetics. 7, 17
- [88] KHOLGHY, M., SAFFARIPOUR, M., YIP, C., AND THOMSON, M. The evolution of soot morphology in a laminar coflow diffusion flame of a surrogate for Jet A-1. *Combust. Flame* *160*, 10 (2013), 2119–2130. 63
- [89] KISLOV, V., SINGH, R., EDWARDS, D., MEBEL, A., AND FRENKLACH, M. Rate coefficients and product branching ratios for the oxidation of phenyl and naphthyl radicals: A theoretical RRKM-ME study. *Proc. Combust. Inst.* *35*, 2 (2015), 1861–1869. 23, 47
- [90] KISLOV, V. V., ISLAMOVA, N. I., KOLKER, A. M., LIN, S. H., AND MEBEL, A. M. Hydrogen Abstraction Acetylene Addition and Diels–Alder Mechanisms of PAH Formation: A Detailed Study Using First Principles Calculations. *J. Chem. Theory Comput.* *1*, 5 (Sept. 2005), 908–924. 4, 23, 24, 28, 29, 30, 31, 33, 39, 49, 50
- [91] KISLOV, V. V., AND MEBEL, A. M. Ab initio g3-type/statistical theory study of the formation of indene in combustion flames. i. pathways involving benzene and phenyl radical. *J. Phys. Chem. A* *111*, 19 (2007), 3922–3931. 52

- [92] KISLOV, V. V., MEBEL, A. M., AND LIN, S. H. Ab Initio and DFT Study of the Formation Mechanisms of Polycyclic Aromatic Hydrocarbons: The Phenanthrene Synthesis from Biphenyl and Naphthalene. *J. Phys. Chem. A* 106, 25 (June 2002), 6171–6182. 30
- [93] KISLOV, V. V., SADOVNIKOV, A. I., AND MEBEL, A. M. Formation Mechanism of Polycyclic Aromatic Hydrocarbons beyond the Second Aromatic Ring. *J. Phys. Chem. A* 117, 23 (2013), 4794–4816. 83
- [94] KONNOV, A. Implementation of the NCN pathway of prompt-NO formation in the detailed reaction mechanism. *Combust. Flame* 156, 11 (2009), 2093–2105. 89
- [95] KOROBEGINICHEV, O. P., YAKIMOV, S. A., KNYAZKOV, D. A., BOLSHOVA, T. A., SHMAKOV, A. G., YANG, J., AND QI, F. A study of low-pressure premixed ethylene flame with and without ethanol using photoionization mass spectrometry and modeling. *Proc. Combust. Inst.* 33, 1 (2011), 569 – 576. 87
- [96] LAI, J. Y. W., ELVATI, P., AND VIOLI, A. Stochastic atomistic simulation of polycyclic aromatic hydrocarbon growth in combustion. *Phys. Chem. Chem. Phys.* 16, 17 (2014), 7969. 2, 8, 9, 10, 11, 14, 19, 20, 21, 51, 94
- [97] LEIDREITER, H. I., AND WAGNER, H. G. An Investigation of the Reaction between O(³ P) and Benzene at High Temperatures. *Z. Phys. Chem.* 165, Part_1 (Jan. 1989), 1–7. 23, 46
- [98] LEPLAT, N., DAGAUT, P., TOGBÉ, C., AND VANDOOREN, J. Numerical and experimental study of ethanol combustion and oxidation in laminar premixed flames and in jet-stirred reactor. *Combust. Flame* 158, 4 (2011), 705–725. 87, 92
- [99] LEUNG, K., LINDSTEDT, R., AND JONES, W. A simplified reaction mechanism for soot formation in nonpremixed flames. *Combust. Flame* 87, 3-4 (Dec. 1991), 289–305. 41
- [100] LI, Y., GAN, Y., AND CAO, Z. Computational insight into excited states of the ring-opening radicals from the pyrolysis of furan biofuels: Computational Insight into Excited States of the Ring-Opening Radicals from the Pyrolysis of Furan Biofuels. *J. Comput. Chem.* (Oct. 2018). 41
- [101] LINDSTEDT, P., MAURICE, L., AND MEYER, M. Thermodynamic and kinetic issues in the formation and oxidation of aromatic species. *Faraday Discuss.* 119 (2002), 409–432. 52
- [102] LIU, H., MA, S., ZHANG, Z., ZHENG, Z., AND YAO, M. Study of the control strategies on soot reduction under early-injection conditions on a diesel engine. *Fuel* 139 (2015), 472–481. 2
- [103] LIU, P., LI, Z., BENNETT, A., LIN, H., SARATHY, S. M., AND ROBERTS, W. L. The site effect on PAHs formation in HACA-based mass growth process. *Combust. Flame* 199 (Jan. 2019), 54–68. 28, 29, 30, 33, 91

- [104] LIU, P., ZHANG, Y., LI, Z., BENNETT, A., LIN, H., SARATHY, S. M., AND ROBERTS, W. L. Computational study of polycyclic aromatic hydrocarbons growth by vinylacetylene addition. *Combust. Flame* 202 (Apr. 2019), 276–291. 4, 5, 31, 34
- [105] LIU, X., WANG, H., WEI, L., LIU, J., REITZ, R. D., AND YAO, M. Development of a reduced toluene reference fuel (TRF)-2,5-dimethylfuran-polycyclic aromatic hydrocarbon (PAH) mechanism for engine applications. *Combust. Flame* 165 (Mar. 2016), 453–465. 41
- [106] LONG, A. E., MERCHANT, S. S., VANDEPUTTE, A. G., CARSTENSEN, H.-H., VERVUST, A. J., MARIN, G. B., VAN GEEM, K. M., AND GREEN, W. H. Pressure dependent kinetic analysis of pathways to naphthalene from cyclopentadienyl recombination. *Combust. Flame* 187 (Jan. 2018), 247–256. 34
- [107] MALICK, D. K., PETERSSON, G. A., AND MONTGOMERY, J. A. Transition states for chemical reactions I. Geometry and classical barrier height. *J. Chem. Phys.* 108, 14 (Apr. 1998), 5704–5713. 41
- [108] MARICQ, M. M. An examination of soot composition in premixed hydrocarbon flames via laser ablation particle mass spectrometry. *J. Aerosol Sci.* 40, 10 (Oct. 2009), 844–857. 3
- [109] MARINOV, N. M. A detailed chemical kinetic model for high temperature ethanol oxidation. *Int. J. Chem. Kinet.* 31, 3 (1999), 183–220. 89
- [110] MARINOV, N. M., PITZ, W. J., WESTBROOK, C. K., VINCITORE, A. M., CASTALDI, M. J., SENKAN, S. M., AND MELIUS, C. F. Aromatic and Polycyclic Aromatic Hydrocarbon Formation in a Laminar Premixed n-Butane Flame. *Combust. Flame* 114, 1–2 (July 1998), 192–213. 24
- [111] MARTIN, J. W., BOWAL, K., MENON, A., SLAVCHOV, R. I., AKROYD, J., MOSBACH, S., AND KRAFT, M. Polar curved polycyclic aromatic hydrocarbons in soot formation. *Proc. Combust. Inst.* 37, 1 (2019), 1117–1123. 5, 6, 32
- [112] MATLAB. *version R2019a*. The MathWorks Inc., Natick, Massachusetts, 2019. 63
- [113] MCENALLY, C. S., AND PFEFFERLE, L. D. The effects of dimethyl ether and ethanol on benzene and soot formation in ethylene nonpremixed flames. *Proc. Combust. Inst.* 31, 1 (Jan. 2007), 603–610. 41
- [114] MCQUARRIE, D. A. Stochastic approach to chemical kinetics. *J. Appl. Probab.* 4, 3 (1967), 413–478. 8
- [115] MEBEL, A., LANDERA, A., AND KAISER, R. Formation Mechanisms of Naphthalene and Indene: From the Interstellar Medium to Combustion Flames. *J. Phys. Chem. A* 121, 5 (Sept. 2017), 901–926. 4, 28, 31, 34

- [116] MEBEL, A. M., GEORGIEVSKII, Y., JASPER, A. W., AND ET. AL. Temperature- and pressure-dependent rate coefficients for the HACA pathways from benzene to naphthalene. *Proc. Combust. Inst.* 36, 1 (2017), 919–926. 76
- [117] MEBEL, A. M., GEORGIEVSKII, Y., JASPER, A. W., AND KLIPPENSTEIN, S. J. Pressure-dependent rate constants for PAH growth: formation of indene and its conversion to naphthalene. *Faraday Discuss.* 195 (2016), 637–670. 4, 5, 28, 29, 31, 52
- [118] MEBEL, A. M., AND KISLOV, V. V. Can the $C_5H_5 + C_5H_5 \rightarrow C_{10}H_{10} + C_{10}H_9 + H$ / $C_{10}H_8 + H_2$ Reaction Produce Naphthalene? An Ab Initio/RRKM Study. *J. Phys. Chem. A* 113, 36 (Sept. 2009), 9825–9833. 34
- [119] MEBEL, A. M., LIN, M. C., CHAKRABORTY, D., PARK, J., LIN, S. H., AND LEE, Y. T. Ab initio molecular orbital/Rice–Ramsperger–Kassel–Marcus theory study of multichannel rate constants for the unimolecular decomposition of benzene and the $H+C_6H_5$ reaction over the ground electronic state. *J. Chem. Phys.* 114, 19 (2001), 8421. 23
- [120] MILLER, J. A., AND KLIPPENSTEIN, S. J. From the Multiple-Well Master Equation to Phenomenological Rate Coefficients: Reactions on a C₃H₄ Potential Energy Surface. *J. Phys. Chem. A* 107, 15 (2003), 2680–2692. 38, 39
- [121] MILLER, J. A., AND KLIPPENSTEIN, S. J. Dissociation of Propyl Radicals and Other Reactions on a C₃H₇ Potential. *J. Phys. Chem. A* 117, 13 (Apr. 2013), 2718–2727. 24
- [122] MOC, J., AND SIMMIE, J. M. Hydrogen Abstraction from n-Butanol by the Hydroxyl Radical: High Level Ab Initio Study of the Relative Significance of Various Abstraction Channels and the Role of Weakly Bound Intermediates. *J. Phys. Chem. A* 114, 17 (2010), 5558–5564. 23
- [123] MURAKAMI, Y., SAEJUNG, T., OHASHI, C., AND FUJII, N. Investigation of a New Pathway Forming Naphthalene by the Recombination Reaction of Cyclopentadienyl Radicals. *Chem. Lett.* 32, 12 (Dec. 2003), 1112–1113. 32, 34
- [124] NAROŽNIK, M., AND NIEDZIELSKI, J. Propylene photolysis at 6.7 eV: calculation of the quantum yields for the secondary processes. *J. Photochem.* 32, 3 (Mar. 1986), 281–292. 24
- [125] ORME, J. P., CURRAN, H. J., AND SIMMIE, J. M. Experimental and Modeling Study of Methyl Cyclohexane Pyrolysis and Oxidation. *J. Phys. Chem. A* 110, 1 (Jan. 2006), 114–131. 24
- [126] PARK, J., XU, Z. F., AND LIN, M. C. Thermal decomposition of ethanol. II. A computational study of the kinetics and mechanism for the $H+C_2H_5OH$ reaction. *J. Chem. Phys.* 118, 22 (June 2003), 9990–9996. 27

- [127] PARKER, D. S. N., KAISER, R. I., BANDYOPADHYAY, B., KOSTKO, O., TROY, T. P., AND AHMED, M. Unexpected Chemistry from the Reaction of Naphthyl and Acetylene at Combustion-Like Temperatures. *Angew. Chem.* 127, 18 (2015), 5511–5514. 83
- [128] POUSSE, E., GLAUDE, P. A., FOURNET, R., AND BATTIN-LECLERC, F. Experimental study of the structure of a lean premixed indane/CH₄/O₂/Ar flame. *Combustion, Explosion, and Shock Waves* 46, 2 (Mar. 2010), 132–139. 37, 42
- [129] POUSSE, E., TIAN, Z., GLAUDE, P., FOURNET, R., AND BATTIN-LECLERC, F. A lean methane premixed laminar flame doped with components of diesel fuel part III: Indane and comparison between n-butylbenzene, n-propylcyclohexane and indane. *Combust. Flame* 157, 7 (2010), 1236 – 1260. 52, 76
- [130] RAJ, A., AL RASHIDI, M. J., CHUNG, S. H., AND SARATHY, S. M. PAH growth initiated by propargyl addition: Mechanism development and computational kinetics. *J. Phys. Chem. A* 118, 16 (Apr. 2014), 2865–2885. 4, 28, 33
- [131] RAJ, A., CELNIK, M., SHIRLEY, R., SANDER, M., PATTERSON, R., WEST, R., AND KRAFT, M. A statistical approach to develop a detailed soot growth model using PAH characteristics. *Combust. Flame* 156, 4 (Apr. 2009), 896–913. 4, 9, 10, 21, 29, 31
- [132] RAJ, A., MAN, P. L., TOTTON, T. S., SANDER, M., SHIRLEY, R. A., AND KRAFT, M. New polycyclic aromatic hydrocarbon (PAH) surface processes to improve the model prediction of the composition of combustion-generated PAHs and soot. *Carbon* 48, 2 (Feb. 2010), 319–332. 9, 10
- [133] RAJ, A., PRADA, I. D. C., AMER, A. A., AND CHUNG, S. H. A reaction mechanism for gasoline surrogate fuels for large polycyclic aromatic hydrocarbons. *Combust. Flame* 159, 2 (2012), 500 – 515. 7
- [134] RAMAN, S., AND CARSTENSEN, H.-H. Tree structure for intermolecular hydrogen abstraction from hydrocarbons (C/H) and generic rate constant rules for abstraction by vinyl radical. *Int. J. Chem. Kinet.* 44, 5 (May 2012), 327–349. 23, 24, 26
- [135] REACTION DESIGN. *CHEMKIN-PRO 15112*. San Diego, 2011. 6, 17, 55, 68, 90, 91
- [136] REACTION DESIGN. *Model Fuel Library*. San Diego, 2014. 24
- [137] RENARD, C., DIAS, V., TIGGELEN, P. J. V., AND VANDOOREN, J. Flame structure studies of rich ethylene–oxygen–argon mixtures doped with CO₂, or with NH₃, or with H₂O. *Proc. Combust. Inst.* 32, 1 (2009), 631 – 637. 88
- [138] RENGARAJAN, T., RAJENDRAN, P., NANDAKUMAR, N., LOKESHKUMAR, B., RAJENDRAN, P., AND NISHIGAKI, I. Exposure to polycyclic aromatic hydrocarbons with special focus on cancer. *Asian Pacific Journal of Tropical Biomedicine* 5, 3 (Mar. 2015), 182–189. 1

- [139] RICHTER, H., GRANATA, S., GREEN, W. H., AND HOWARD, J. B. Detailed modeling of PAH and soot formation in a laminar premixed benzene/oxygen/argon low-pressure flame. *Proc. Combust. Inst.* 30, 1 (Jan. 2005), 1397–1405. 7, 28, 35, 89
- [140] SAFFARIPOUR, M., KHOLGHY, M., DWORKIN, S., AND THOMSON, M. A numerical and experimental study of soot formation in a laminar coflow diffusion flame of a Jet A-1 surrogate. *Proc. Combust. Inst.* 34, 1 (2013), 1057–1065. 63, 64
- [141] SAGGESE, C., CUOCI, A., FRASSOLDATI, A., FERRARIO, S., CAMACHO, J., WANG, H., AND FARAVELLI, T. Probe effects in soot sampling from a burner-stabilized stagnation flame. *Combust. Flame* 167 (2016), 184–197. 66
- [142] SALAMANCA, M., SIRIGNANO, M., COMMODO, M., MINUTOLO, P., AND D’ANNA, A. The effect of ethanol on the particle size distributions in ethylene premixed flames. *Exp. Therm. Fluid Sci.* 43 (2012), 71–75. 3, 41, 87, 88, 92
- [143] SALAMANCA, M., SIRIGNANO, M., AND D’ANNA, A. Particulate Formation in Premixed and Counter-flow Diffusion Ethylene/Ethanol Flames. *Energy & Fuels* 26, 10 (2012), 6144–6152. 88
- [144] SALDINGER, J. C., WANG, Q., ELVATI, P., AND VIOLI, A. Characterizing the diversity of aromatics in a coflow diffusion Jet A-1 surrogate flame. *Fuel* 268 (2020), 117198. 58, 62
- [145] SARATHY, S. M., KUKKADAPU, G., MEHL, M., JAVED, T., AHMED, A., NASER, N., TEKAWADE, A., KOSIBA, G., ALABBAD, M., SINGH, E., PARK, S., RASHIDI, M. A., CHUNG, S. H., ROBERTS, W. L., OEHLSCHLAEGER, M. A., SUNG, C.-J., AND FAROOQ, A. Compositional effects on the ignition of FACE gasolines. *Combust. Flame* 169 (July 2016), 171–193. 89
- [146] SARATHY, S. M., VRANCKX, S., YASUNAGA, K., MEHL, M., OSSWALD, P., METCALFE, W. K., WESTBROOK, C. K., PITZ, W. J., KOHSE-HÖINGHAUS, K., FERNANDES, R. X., AND CURRAN, H. J. A comprehensive chemical kinetic combustion model for the four butanol isomers. *Combust. Flame* 159, 6 (June 2012), 2028–2055. 27
- [147] SCHULZ, F., COMMODO, M., KAISER, K., DE FALCO, G., MINUTOLO, P., MEYER, G., D’ANNA, A., AND GROSS, L. Insights into incipient soot formation by atomic force microscopy. *Proc. Combust. Inst.* 37, 1 (2019), 885–892. 5, 11, 32, 51, 55, 68
- [148] SCOTT, M., AND WALKER, R. W. Addition of toluene and ethylbenzene to mixtures of H₂ and O₂ at 773 K: Part I: Kinetic measurements for H and HO₂ reactions with the additives and a data base for H abstraction by HO₂ from alkanes, aromatics and related compounds. *Combust. Flame* 129, 4 (June 2002), 365–377. 24

- [149] SENDT, K., BACSKAY, G. B., AND MACKIE, J. C. Pyrolysis of Furan: Ab Initio Quantum Chemical and Kinetic Modeling Studies. *J. Phys. Chem. A* *104*, 9 (Mar. 2000), 1861–1875. 41
- [150] SHANDROSS, R. A., LONGWELL, J. P., AND HOWARD, J. B. Destruction of benene in high-temperature flames: Chemistry of benene and phenol. *Proc. Combust. Inst.* *26*, 1 (Jan. 1996), 711–719. 27, 48
- [151] SHAO, C., WANG, H., ATEF, N., WANG, Z., CHEN, B., ALMALKI, M., ZHANG, Y., CAO, C., YANG, J., AND SARATHY, S. M. Polycyclic aromatic hydrocarbons in pyrolysis of gasoline surrogates (n-heptane/iso-octane/toluene). *Proc. Combust. Inst.* *37*, 1 (2019), 993 – 1001. 7
- [152] SHI, X., WANG, Q., AND VIOLI, A. Chemical pathways for the formation of benzofuran and dibenzofuran in combustion. *Combust. Flame* *212* (Feb. 2020), 216–233. 11, 25, 28, 35, 36, 37, 38, 39, 40, 41, 42, 45, 51, 70, 87
- [153] SHI, X., WANG, Q., AND VIOLI, A. Reaction pathways for the formation of five-membered rings onto polyaromatic hydrocarbon framework. *Fuel* *283* (Jan. 2021), 119023. 41, 54
- [154] SIEGMANN, K., HEPP, H., AND SATTLER, K. Reactive Dimerization: A New PAH Growth Mechanism in Flames. *Combust. Sci. Technol.* *109*, 1-6 (1995), 165–181. 69, 94
- [155] SIEGMANN, K., AND SATTLER, K. Formation mechanism for polycyclic aromatic hydrocarbons in methane flames. *The Journal of Chemical Physics* *112*, 2 (Jan. 2000), 698–709. 4, 33, 67
- [156] SIRIGNANO, M., CIAJOLO, A., D’ANNA, A., AND RUSSO, C. Chemical Features of Particles Generated in an Ethylene/Ethanol Premixed Flame. *Energy & Fuels* *31*, 3 (2017), 2370–2377. 87, 88
- [157] SKEEN, S. A., MICHELSEN, H. A., WILSON, K. R., POPOLAN, D. M., VIOLI, A., AND HANSEN, N. Near-threshold photoionization mass spectra of combustion-generated high-molecular-weight soot precursors. *J. Aerosol Sci.* *58* (Apr. 2013), 86–102. 34, 88
- [158] SOMERS, K. P., AND SIMMIE, J. M. Benchmarking Compound Methods (CBS-QB3, CBS-APNO, G3, G4, W1BD) against the Active Thermochemical Tables: Formation Enthalpies of Radicals. *J. Phys. Chem. A* *119*, 33 (Aug. 2015), 8922–8933. 7
- [159] STEIN, S. E., AND FAHR, A. High-temperature stabilities of hydrocarbons. *J. Phys. Chem.* *89*, 17 (Aug. 1985), 3714–3725. 11, 72
- [160] SU, D., JENTOFT, R., MÜLLER, J.-O., ROTHE, D., JACOB, E., SIMPSON, C., TOMOVIĆ, Ž., MÜLLEN, K., MESSERER, A., PÖSCHL, U., NIESSNER, R., AND

- SCHLÖGL, R. Microstructure and oxidation behaviour of Euro IV diesel engine soot: A comparative study with synthetic model soot substances. *Catal. Today* 90, 1 (2004), 127–132. Air Pollution Abatement Symposium. 5, 6
- [161] TAATJES, C. A., OSBORN, D. L., SELBY, T. M., MELONI, G., TREVITT, A. J., EPIFANOVSKY, E., KRYLOV, A. I., SIRJEAN, B., DAMES, E., AND WANG, H. Products of the Benzene + O(3p) Reaction. *J. Phys. Chem. A* 114, 9 (Mar. 2010), 3355–3370. 43, 47
- [162] THERRIEN, R. J., ERGUT, A., LEVENDIS, Y. A., RICHTER, H., HOWARD, J. B., AND CARLSON, J. B. Investigation of critical equivalence ratio and chemical speciation in flames of ethylbenzene–ethanol blends. *Combust. Flame* 157, 2 (Feb. 2010), 296–312. 41, 87, 88, 96
- [163] THOMAS, S., PODDAR, N. B., AND WORNAT, M. J. Identification of Methylene-Bridged Polycyclic Aromatic Hydrocarbon Products of Catechol Pyrolysis. *Polycycl. Aromat. Compd.* 32, 4 (Aug. 2012), 531–555. Publisher: Taylor & Francis. 51
- [164] TIBAQUIRÁ, J. E., HUERTAS, J. I., OSPINA, S., QUIRAMA, L. F., AND NIÑO, J. E. The Effect of Using Ethanol-Gasoline Blends on the Mechanical, Energy and Environmental Performance of In-Use Vehicles. *Energies* 11, 1 (Jan. 2018), 221. 87
- [165] TOTTON, T. S., MISQUITTA, A. J., AND KRAFT, M. A quantitative study of the clustering of polycyclic aromatic hydrocarbons at high temperatures. *Phys. Chem. Chem. Phys.* 14 (2012), 4081–4094. 51
- [166] TRANTER, R. S., LYNCH, P. T., RANDAZZO, J. B., LOCKHART, J. P. A., CHEN, X., AND GOLDSMITH, C. F. High temperature pyrolysis of 2-methyl furan. *Phys. Chem. Chem. Phys.* 20, 16 (2018), 10826–10837. 41
- [167] TREE, D. R., AND SVENSSON, K. I. Soot processes in compression ignition engines. *Prog. Energy Combust. Sci.* 33, 3 (2007), 272–309. 2
- [168] TREGROSSI, A., CIAJOLO, A., AND BARBELLA, R. The combustion of benzene in rich premixed flames at atmospheric pressure. *Combust. Flame* 117, 3 (May 1999), 553–561. 11, 45
- [169] TSANG, W. Chemical Kinetic Data Base for Combustion Chemistry. Part 3: Propane. *J. Phys. Chem. Ref. Data* 17, 2 (Apr. 1988), 887–951. 24
- [170] TSANG, W. Chemical Kinetic Data Base for Combustion Chemistry Part V. Propene. *J. Phys. Chem. Ref. Data* 20, 2 (Mar. 1991), 221–273. 24
- [171] TSANG, W., AND HAMPSON, R. F. Chemical Kinetic Data Base for Combustion Chemistry. Part I. Methane and Related Compounds. *J. Phys. Chem. Ref. Data* 15, 3 (July 1986), 1087–1279. 35

- [172] TSUJI, H. Counterflow diffusion flames. *Prog. Energy Combust. Sci.* 8, 2 (1982), 93–119. 81
- [173] URNESS, K. N., GUAN, Q., GOLAN, A., DAILY, J. W., NIMLOS, M. R., STANTON, J. F., AHMED, M., AND ELLISON, G. B. Pyrolysis of furan in a microreactor. *J. Chem. Phys.* 139, 12 (Sept. 2013), 124305. 41
- [174] VASU, S. S., HONG, Z., DAVIDSON, D. F., HANSON, R. K., AND GOLDEN, D. M. Shock Tube/Laser Absorption Measurements of the Reaction Rates of OH with Ethylene and Propene. *J. Phys. Chem. A* 114, 43 (Nov. 2010), 11529–11537. 24
- [175] VIOLI, A. Modeling of soot particle inception in aromatic and aliphatic premixed flames. *Combust. Flame* 139, 4 (Dec. 2004), 279–287. 8, 9
- [176] VIOLI, A. Cyclodehydrogenation Reactions to Cyclopentafused Polycyclic Aromatic Hydrocarbons. *J. Phys. Chem. A* 109, 34 (Sept. 2005), 7781–7787. 4, 29, 51
- [177] VIOLI, A., TRUONG, T. N., AND SAROFIM, A. F. Kinetics of Hydrogen Abstraction Reactions from Polycyclic Aromatic Hydrocarbons by H Atoms. *J. Phys. Chem. A* 108, 22 (June 2004), 4846–4852. 23, 26
- [178] VIOLI, A., AND VENKATNATHAN, A. Combustion-generated nanoparticles produced in a benzene flame: A multiscale approach. *J. Chem. Phys.* 125, 5 (Aug. 2006), 054302. 8, 9
- [179] WAGNON, S. W., THION, S., NILSSON, E. J., MEHL, M., SERINYEL, Z., ZHANG, K., DAGAUT, P., KONNOV, A. A., DAYMA, G., AND PITZ, W. J. Experimental and modeling studies of a biofuel surrogate compound: Laminar burning velocities and jet-stirred reactor measurements of anisole. *Combust. Flame* 189 (Mar. 2018), 325–336. 37, 42
- [180] WANG, H., AND FRENKLACH, M. A detailed kinetic modeling study of aromatics formation in laminar premixed acetylene and ethylene flames. *Combust. Flame* 110, 1 (1997), 173–221. 89
- [181] WANG, H., YOU, X., JOSHI, A. V., DAVIS, S. G., LASKIN, A., EGOLFOPOULOS, F., AND LAW, C. K. USC mech version II. high-temperature combustion reaction model of H₂/CO/C₁-C₄ compounds, 2007. 7, 89
- [182] WANG, Q., ELVATI, P., KIM, D., JOHANSSON, K. O., SCHRADER, P. E., MICHELSEN, H. A., AND VIOLI, A. Spatial dependence of the growth of polycyclic aromatic compounds in an ethylene counterflow flame. *Carbon* 149 (2019), 328 – 335. 34, 38, 41, 42, 47, 58, 59, 67, 80, 81, 88, 96
- [183] WANG, Q., SALDINGER, J. C., ELVATI, P., AND VIOLI, A. Insights on the effect of ethanol on the formation of aromatics. *Fuel* 264 (2020), 116773. 7, 80, 88

- [184] WANG, Q., SALDINGER, J. C., ELVATI, P., AND VIOLI, A. Molecular structures in flames: A comparison between SNapS2 and recent AFM results. *Proc. Combust. Inst.* (Sept. 2020). 55, 58, 68, 69
- [185] WANG, Y., RAJ, A., AND CHUNG, S. H. A PAH growth mechanism and synergistic effect on PAH formation in counterflow diffusion flames. *Combust. Flame* 160, 9 (Sept. 2013), 1667–1676. 7, 28, 68, 89
- [186] WANG, Z., HERBINET, O., HANSEN, N., AND BATTIN-LECLERC, F. Exploring hydroperoxides in combustion: History, recent advances and perspectives. *Prog. Energy Combust. Sci.* 73 (2019), 132–181. 66
- [187] WEBER, I., FRIESE, P., AND OLZMANN, M. H-Atom-Forming Reaction Pathways in the Pyrolysis of Furan, 2-Methylfuran, and 2,5-Dimethylfuran: A Shock-Tube and Modeling Study. *J. Phys. Chem. A* 122, 32 (Aug. 2018), 6500–6508. 41
- [188] WEI, L., TANG, C., MAN, X., AND HUANG, Z. Shock-Tube Experiments and Kinetic Modeling of 2-Methylfuran Ignition at Elevated Pressure. *Energy & Fuels* 27, 12 (Dec. 2013), 7809–7816. 41
- [189] WEININGER, D. SMILES, a chemical language and information system. 1. Introduction to methodology and encoding rules. *J. Chem. Inf. Comput. Sci.* 28, 1 (Feb. 1988), 31–36. 18
- [190] WELZ, O., SAVEE, J. D., OSBORN, D. L., VASU, S. S., PERCIVAL, C. J., SHALLCROSS, D. E., AND TAATJES, C. A. Direct Kinetic Measurements of Criegee Intermediate CH₂OO Formed by Reaction of CH₂I with O₂. *Science* 335, 6065 (2012), 204–207. 64
- [191] WESTBROOK, C. K., MEHL, M., PITZ, W. J., AND SJÖBERG, M. Chemical kinetics of octane sensitivity in a spark-ignition engine. *Combust. Flame* 175 (Jan. 2017), 2–15. 23, 24, 27, 35, 36, 37
- [192] WHITESIDES, R., DOMIN, D., SALOMÓN-FERRER, R., LESTER, W. A., AND FRENKLACH, M. Embedded-ring migration on graphene zigzag edge. *Proc. Combust. Inst.* 32, 1 (2009), 577–583. 51
- [193] WHITESIDES, R., AND FRENKLACH, M. Detailed Kinetic Monte Carlo Simulations of Graphene-Edge Growth. *J. Phys. Chem. A* 114, 2 (Jan. 2010), 689–703. 9, 10, 32, 51
- [194] WU, C.-W., LEE, Y.-P., XU, S., AND LIN, M. C. Experimental and Theoretical Studies of Rate Coefficients for the Reaction O(3p) + C₂H₅OH at High Temperatures. *J. Phys. Chem. A* 111, 29 (July 2007), 6693–6703. 27
- [195] WU, J., SONG, K. H., LITZINGER, T., LEE, S.-Y., SANTORO, R., LINEVSKY, M., COLKET, M., AND LISCINSKY, D. Reduction of PAH and soot in premixed ethylene–air flames by addition of ethanol. *Combust. Flame* 144, 4 (2006), 675–687. 3, 41, 87, 88, 89, 92

- [196] WU, S., YANG, H., HU, J., SHEN, D., ZHANG, H., AND XIAO, R. Pyrolysis of furan and its derivatives at 1100 °C: PAH products and DFT study. *J. Anal. Appl. Pyrol.* 120 (July 2016), 252–257. 41
- [197] XU, N., TANG, C., MENG, X., FAN, X., TIAN, Z., AND HUANG, Z. Experimental and Kinetic Study on the Ignition Delay Times of 2,5-Dimethylfuran and the Comparison to 2-Methylfuran and Furan. *Energy & Fuels* 29, 8 (Aug. 2015), 5372–5381. 41
- [198] XU, Z. F., AND LIN, M. C. Ab Initio Kinetics for the Unimolecular Reaction $C_6H_5OH \rightarrow CO + C_5H_6$. *J. Phys. Chem. A* 110, 4 (Feb. 2006), 1672–1677. 27
- [199] XU, Z. F., PARK, J., AND LIN, M. C. Thermal decomposition of ethanol. III. A computational study of the kinetics and mechanism for the $CH_3 + C_2H_5OH$ reaction. *J. Chem. Phys* 120, 14 (Apr. 2004), 6593–6599. 27
- [200] YAPP, E. K., WELLS, C. G., AKROYD, J., MOSBACH, S., XU, R., AND KRAFT, M. Modelling PAH curvature in laminar premixed flames using a detailed population balance model. *Combust. Flame* 176 (2017), 172–180. 10, 32, 51
- [201] YUAN, W., LI, W., LI, Y., LI, T., ZENG, M., ZHANG, Y., ZOU, J., CAO, C., YANG, J., AND QI, F. Experimental and kinetic modeling investigation on anisole pyrolysis: Implications on phenoxy and cyclopentadienyl chemistry. *Combust. Flame* 201 (Mar. 2019), 187–199. 37, 41
- [202] ZADOR, J., HUANG, H., WELZ, O., ZETTERBERG, J., OSBORN, D. L., AND TAATJES, C. A. Directly measuring reaction kinetics of 1QOOH – a crucial but elusive intermediate in hydrocarbon autoignition. *Phys. Chem. Chem. Phys.* 15, 26 (2013), 10753–10760. 64
- [203] ZHANG, H.-B., HOU, D., LAW, C. K., AND YOU, X. Role of Carbon-Addition and Hydrogen-Migration Reactions in Soot Surface Growth. *J. Phys. Chem. A* 120, 5 (2016), 683–689. 4
- [204] ZHANG, H.-B., YOU, X., AND LAW, C. K. Role of Spin-Triplet Polycyclic Aromatic Hydrocarbons in Soot Surface Growth. *J. Phys. Chem. Lett.* 6, 3 (2015), 477–481. 4
- [205] ZHANG, Y., AND TAO, S. Global atmospheric emission inventory of polycyclic aromatic hydrocarbons (PAHs) for 2004. *Atmos. Environ.* 43, 4 (Feb. 2009), 812–819. 1
- [206] ZHAO, L., PRENDERGAST, M., KAISER, R. I., XU, B., ABLIKIM, U., LU, W., AHMED, M., OLEINIKOV, A. D., AZYAZOV, V. N., HOWLADER, A. H., WNUK, S. F., AND MEBEL, A. M. How to add a five-membered ring to polycyclic aromatic hydrocarbons (pahs) – molecular mass growth of the 2-naphthyl radical (c10h7) to benzindenes (c13h10) as a case study. *Phys. Chem. Chem. Phys.* 21 (2019), 16737–16750. 52

- [207] ZHONG, X., AND BOZZELLI, J. W. Thermochemical and Kinetic Analysis of the H, OH, HO₂, O, and O₂ Association Reactions with Cyclopentadienyl Radical. *J. Phys. Chem. A* 102, 20 (May 1998), 3537–3555. 35, 37, 70
- [208] ZHOU, C.-W., SIMMIE, J. M., AND CURRAN, H. J. Rate constants for hydrogen-abstraction by from n-butanol. *Combust. Flame* 158, 4 (Apr. 2011), 726–731. 27
- [209] ZHOU, C.-W., SIMMIE, J. M., AND CURRAN, H. J. Rate constants for hydrogen abstraction by HO₂ from n-butanol. *Int. J. Chem. Kinet.* 44, 3 (Mar. 2012), 155–164. 27
- [210] ZÁDOR, J., W. JASPER, A., AND A. MILLER, J. The reaction between propene and hydroxyl. *Phys. Chem. Chem. Phys.* 11, 46 (2009), 11040–11053. 24